

AN EXAMINATION OF ESTUARINE LUTOCLINE DYNAMICS

By

JIANHUA JIANG

A DISSERTATION PRESENTED TO THE GRADUATE SCHOOL
OF THE UNIVERSITY OF FLORIDA IN
PARTIAL FULFILLMENT OF THE REQUIREMENTS
FOR THE DEGREE OF DOCTOR OF PHILOSOPHY

UNIVERSITY OF FLORIDA

1999

ACKNOWLEDGMENT

I would like to express my most profound gratitude to my advisor and the chairman of my supervisory committee, Dr. Ashish J. Mehta, professor of Coastal and Oceanographic Engineering, for his guidance and support throughout my study at the University of Florida. It has been a challenging and a rewarding experience for me.

I wish to express my deep appreciation to the members of my supervisory committee, Graduate Research Professor Robert G. Dean, Associate Professor Kirk Hatfield, Professor D. Max Sheppard and Assistant Professor Robert J. Thieke for their helpful advice, comments and patience in reviewing this dissertation. Thanks are also due to all other teaching faculty members in the Coastal & Oceanographic Engineering Department, as well as those whose courses I attended in Aerospace Engineering, Mechanics & Engineering Science and Environmental Engineering Sciences. They supplied me with knowledge essential for the pursuit of this study through their creative teaching efforts. Special thanks are due to Jim Joiner and Sydney Schofield of the Coastal Engineering Laboratory, and John Davis and Twedell Helen of the Coastal Engineering Archives.

My thanks also extend to Dr. Eric Wolanski of the Australian Institute of Marine Science, for his valuable suggestions and discussions. Our joint effort on the investigation of vertical mixing due to breaking of internal waves at the lutocline in the Jiaojiang estuary, China, gave me the initial direction of this study.

Many fellow student colleagues, including Al Browder, Matt Henderson, Hugo Rodriguez, Bill McAnally, Chenxia Qiu, Detong Sun, and others gave me support in various ways.

This study has been made possible in part due to data gathered in the Jiaojiang. These campaigns were successfully carried out due to the sincere efforts of Professors Xie Qinchun, Li Yan, Li Bogen, Xia Xiaomin, Feng Yinjun, and others, all of the Second Institute of Oceanography, Hangzhou.

Most important of all, I am deeply indebted to my wife, Tian Fang, and my daughter, Jiang Ruiwei. Although we were separated from each other during my education at UF, they always provided me their strong support, persuasion and love from the other side of the Pacific Ocean. My family has been the source of my perseverance with this work.

TABLE OF CONTENTS

	<u>page</u>
ACKNOWLEDGMENTS	ii
LIST OF FIGURES	viii
LIST OF TABLES	xviii
LIST OF SYMBOLS	xix
ABSTRACT	xl
CHAPTERS	
1 INTRODUCTION	1
1.1 Problem Statement	1
1.2 Objectives	3
1.3 Tasks	4
1.4 Thesis Outline	5
2 LUTOCLINES IN ESTUARIES	7
2.1 Vertical Structure of Fine Sediment Suspension and the Lutocline	7
2.2 Causes of Fluid Mud and Lutocline Generation	9
2.2.1 Settling Velocity	11
2.2.2 Formation of Fluid Mud	12
2.2.3 Formation of Lutocline	12
2.3 Influence of Lutocline on Turbidity Transport	14
2.4 Dynamics of Turbid Estuaries	16
2.4.1 Amazon Shelf	17
2.4.2 Ariake Bay	18
2.4.3 Gironde River	19
2.4.4 Hangzhou Bay	20
2.4.5 James River	21
2.4.6 Orinoco River	22

2.4.7	Rhine-Meuse River	23
2.4.8	Severn River	24
2.4.9	South Alligator River	24
2.4.10	Thames River	25
2.4.11	Yellow River	26
3	FLOW AND SEDIMENT TRANSPORT	28
3.1	Introduction	28
3.2	Hydrodynamics	29
3.2.1	Governing Equations	29
3.2.2	Boundary Conditions	31
3.3	Sediment Transport	35
3.3.1	Sediment Conservation Equation in the Water Column	35
3.3.2	Boundary Conditions	35
3.3.3	Fine Sediment Transport Processes	37
3.4	Flow-Sediment Coupling	43
3.4.1	Baroclinic Effects	43
3.4.2	Vertical Momentum and Mass Diffusion Coefficients	43
3.5	Solution Techniques	47
3.5.1	Discretization of Hydrodynamic Equations	48
3.5.2	Discretization of Sediment Transport Equation	50
3.5.3	Discretization of Consolidation Equation	51
3.5.4	Properties of the Finite-Differential Equations	52
3.6	Basic Simulations	54
3.6.1	Hydrodynamics	54
3.6.2	Sediment Transport	60
3.6.3	Consolidation	68
3.6.4	Interfacial Entrainment	73
4	FIELD INVESTIGATION AND DATA ANALYSIS	75
4.1	Study Area Description	75
4.2	Experimental Plan, Methods and Instruments	77
4.2.1	Fluid Mud Observations	77
4.2.2	Lutocline Observations	79
4.2.3	Observations of SSC, Currents, Salinity and Temperature	80
4.2.4	Tidal Elevations	80
4.3	Experimental Data	80
4.3.1	Sediment Size	80
4.3.2	Tides	81
4.3.3	Profiles of SSC	83
4.3.4	ASSM Data	83

	4.3.5 Floc Settling Velocity	102
	4.3.6 Erosion Rate Constant	105
4.4	Properties of Internal Waves	107
	4.4.1 Effect of Ri_0 on H_s	107
	4.4.2 Effect of Ri_0 on ω_a	108
	4.4.3 Celerity and Wave Length	111
5	TURBULENCE DAMPING IN FLUID MUD	114
	5.1 Introduction	114
	5.2 Turbulence Damping and its Effect on Lutocline Formation	115
	5.3 Mixing Length in the Jiaojiang	125
	5.4 Modified Vertical Momentum and Mass Diffusion Coefficients	127
6	LUTOCLINE DYNAMICS IN THE JIAOJIANG	128
	6.1 Introduction	128
	6.2 Parameters for Flow and Sedimentary Processes	128
	6.3 Model Application	132
	6.3.1 Modeled Domain, Initial and boundary Conditions	132
	6.3.2 Sediment Deposition, Erosion, Consolidation and Entrainment	134
	6.4 Flow and Sediment Dynamics	136
	6.4.1 Flow Field	136
	6.4.2 Tidal Variation of Velocity	137
	6.4.3 Tidal Variation of SSC	142
	6.4.4 Vertical Profiles of Velocity	146
	6.4.5 Vertical Profiles of SSC	155
	6.4.6 Lutocline Layer	163
	6.4.7 Flow-SSC Hysteresis	168
	6.4.8 Effect of Turbulence Damping on SSC and Lutocline Formation	174
7	SUMMARY AND CONCLUSIONS	176
	7.1 Summary	176
	7.2 Conclusions	177
	7.3 Recommendations for Future Studies	179

APPENDICES

A	DERIVATIONS OF THE GOVERNING EQUATIONS	181
A.1	Vertical Velocities, w and ω , and Continuity Equation (3.1)	181
A.2	Momentum Equations (3.2) and (3.3)	183
A.3	Sediment Conservation Equation (3.15)	185
B	NUMERICAL TECHNIQUES	187
B.1	Back-Tracing Approach	187
B.2	Pre-conditioned Conjugate Gradient Method	188
C	EFFECT OF TEMPERATURE ON SETTLING VELOCITY	191
D	AN APPLICATION OF COHYD-UF:CONTRACTION SCOUR IN A RIVER	197
D.1	Scour Problem	197
D.2	Scour Simulation	200
D.3	Results	203
E	SIMULATION OF SEDIMENT DEPOSITION IN A FLUME	206
E.1	Introduction	206
E.2	Flume Test	206
E.3	Settling Velocity in Moving Water	207
E.4	Deposition Simulation	210
	BIBLIOGRAPHY	214
	BIOGRAPHICAL SKETCH	226

LIST OF FIGURES

<u>Figure</u>	<u>page</u>	
2.1	Vertical dry SSC profile classification and associated velocity profile. Also shown are unit transport processes which govern concentration profile dynamics (after Mehta, 1989; 1991)	8
2.2	A representative description of settling velocity and flux variation with SSC (after Mehta and Li, 1997)	10
2.3	Mixing of a two-layered stratified fluid, with fluid mud beneath clear water . . .	16
3.1	Schematic diagram showing σ -transform	29
3.2	Dimensionless median settling velocity as a function of temperature, where ω_{50} is the median settling velocity at 15 °C	44
3.3	Schematic diagram of computational mesh and notation	48
3.4	Schematization of the simulated consolidation process, where (a) is the original consolidating layer, (b) is the case of net deposition and (c) is the case of net erosion	52
3.5	Modeling 1D linear hydrodynamic equation for tidal flow in an open channel. Lines are simulations and open circles represent analytical solutions	57
3.6	Modeling 1D linear hydrodynamic equation for tidal flow in an open channel. Lines are simulations and open circles represent analytical solutions	57
3.7	Modeling 1D non-linear hydrodynamic equation for tidal flow in an open channel. Lines are simulations and open circles represent analytical solutions	59
3.8	Modeling 1D non-linear hydrodynamic equation for tidal flow in an open channel. Lines are simulations and open circles represent analytical solutions	59

3.9	Modeling 1D convection-diffusion equation. Line is analytical solution and dots represent model simulations	62
3.10	Modeling 2D Laplace equation. Lines are analytical solution and open circles represent model simulations	62
3.11	Modeling 1D transient heat conduction. Lines are analytical solutions and dots represent model simulations	64
3.12	Modeling heat conduction with radiation. Lines are analytical solutions and dots represent model simulations	64
3.13	Modeling 1D transient convection-diffusion equation. Lines are analytical solutions and dots represent model simulations	66
3.14	Modeling 3D Laplace equation. Lines are analytical solutions, dots represent model simulations, and plus signs are associated with contour number	67
3.15	Modeling SSC (unit: kg m^{-3}). Solid lines are simulations and dashed lines represent field data observed from 1800, 9/24/68 to 0400, 9/25/68 in Savannah River estuary (after Ariathurai, et al., 1977). Contours from the surface to the bottom are 0.1, 0.25, 0.5, 1, 1.5 and 2, respectively	70
3.16	Consolidation rate, ω_{sc} , as a function of dry density for Doel Dock mud with $c_f=80 \text{ kg m}^{-3}$ (after Toorman and Berlamont, 1993)	70
3.17	Modeling laboratory data of Toorman and Berlamont (1993) on consolidation without deposition at the bed-fluid interface. Lines are model simulations and points represent data	71
3.18	Modeled consolidation curve (solid line) compared with the laboratory data (open circles) of Toorman and Berlamont (1993)	71
3.19	Consolidation rate, ω_{sc} , as a function of dry density for the laboratory tests of Burt and Parker (1984) with $c_f=26.3 \text{ kg m}^{-3}$	72
3.20	Modeling laboratory data of Burt and Parker (1984) on consolidation with deposition at the bed-fluid interface. Lines are model simulations and points represent data	73
3.21	Modeling laboratory data on entrainment by Mehta and Srinivas (1993). Lines are model simulations and points represent data	74

4.1	Location map of Jiaojiang estuary, China. Depths are in meters below lowest astronomical tide. M1 and M2 are mooring sites (Table 4.1); C1, C2, C3 and C4 are velocity measurement and SSC profile sampling stations (Table 4.1); C6 is the site of ASSM (Table 4.1) and T1-T6 are tide stations. The region between double dotted lines is the modeled domain	76
4.2	A representative frequency distribution of suspended sediment (dispersed) size in the Jiaojiang estuary	81
4.3	Time series of tidal elevation at sites T1 and T5 during a spring tide from 0000 hr on 11/05/94 to 0100 hr on 11/06/94	82
4.4	Time series of velocity at site C4 during a spring tide. Observations began at 1700 hr on November 5, 1994. Positive numbers signify flood and negative are for ebb	84
4.5	Time series of velocity at site C4 during a neap tide. Observations began at 0900 hr on November 10, 1994. Positive numbers signify flood and negative are for ebb	84
4.6	Time series of velocity at site C6 during a neap tide. Observations began at 0630 hr on November 15, 1995. Positive numbers signify flood and negative are for ebb	85
4.7	Time series of SSC at site C4 during a spring tide. Observations began at 1700 hr on November 5, 1994. Shaded area includes SSC greater than 20 kg m ⁻³	85
4.8	Time series of SSC at site C4 during a neap tide. Observations began at 0900 hr on November 10, 1994. Shaded area includes SSC greater than 20 kg m ⁻³	86
4.9	Time series of SSC at site C6 during a neap tide. Observations began at 0600 hr on November 15, 1995. Shaded area includes SSC greater than kg m ⁻³	86
4.10	Typical raw ASSM records during the neap tide on November 15, 1995, with a horizontal time scale of 1 min and a vertical distance scale of 1.25 m. (A) was observed during a flood with a value of Richardson number Ri_0 of about 2, and (b) during an ebb with Ri_0 of about 150	87
4.11	Relationship between lutocline elevations above bottom detected by the turbidimeter and by the ASSM. Data were collected during 0600-1600 hr on November 15, 1995	88

4.12	Time series of lutocline elevation at site C6 during a neap tide using ASSM on November 15, 1995. (a) and (b) were sampled during flood with a value of Ri_0 of about 1, and (c) during ebb with Ri_0 of about 150. Solid lines are instantaneous elevations and dashed lines are mean trends	89
4.13	Time series of lutocline elevation after trend removal at site C6 during a neap tide, where (a), (b) and (c) correspond to Figure 4.12	91
4.14	Typical profiles of internal waves exhibiting sharp crests and flat troughs. Data were taken from example (a) in Figure 4.13. Wave heights range from 0.07 m to 0.23 m	92
4.15	Auto-correlation function against time interval, where (a), (b) and (c) correspond to Figure 4.13	94
4.16	Internal wave spectrum corresponding to example (a) in Figure 4.13	94
4.17	Internal wave spectrum corresponding to example (b) in Figure 4.13	95
4.18	Internal wave spectrum corresponding to example (c) in Figure 4.13	95
4.19	rsm of high-frequency internal wave height as a function of global Richardson number	97
4.20	Modal frequency of high-frequency internal waves as a function of global Richardson number	97
4.21	rms of high-frequency internal wave height during ebb and flood	98
4.22	Modal frequency of high-frequency internal waves during ebb and flood	98
4.23	rsm of low-frequency internal wave height as a function of global Richardson number	99
4.24	Modal frequency of low-frequency internal waves as a function of global Richardson number	99
4.25	rms of low-frequency internal wave height during ebb and flood	100
4.26	Modal frequency of low-frequency internal waves during ebb and flood	100

4.27	Settling velocity as a function of SSC during a neap tide from 0900 hr on 11/10/94 to 1000 hr on 11/11/94. Solid line is the best-fit of the calculated data points using Eq. (4.12)	104
4.28	Settling velocity as a function of SSC during a spring tide from 1700 hr on 11/05/94 to 1800 hr on 11/06/94. Solid line is the best-fit of the calculated data points using Eq. (4.12)	104
4.29	Erosion rate as a function of excess bottom shear stress	107
4.30	Definition sketch of two-layered flow system	110
5.1	Definition of linear sediment concentration, c_λ , and its relationship with sediment concentration, c . d_f is the floc diameter	117
5.2	Relative momentum mixing length calculated from Eq. (5.11) (solid lines), field data (data points) and settling flux (dashed line) as functions of SSC . . .	123
5.3	Lutocline strength index as a function of turbulence energy production based on measured profiles of SSC and velocity. The equation represents the best-fit line	125
6.1	Bathymetry in the modeled domain of the Jiaojiang (a), where the datum is mean water level and the regions enclosed within dotted lines are mudflats, and the numerical mesh in the horizontal plane (b)	133
6.2	Simulated peak flood flow during a spring tide at 2000 hr, 11/05/94	138
6.3	Simulated high water slack during a spring tide at 2245 hr, 11/05/94	138
6.4	Simulated peak ebb flow during a spring tide at 0100 hr, 11/06/94	139
6.5	Simulated low water slack during a spring tide at 0615 hr, 11/06/94	139
6.6	Tidal velocity at $0.4H$ (a), and SSC at $0.25H$ (b) and at $0.75H$ (c) at C2 during a spring tide. Solid lines are simulations and dashed lines represent field data collected during 1800 hr, 11/05/94 to 1700 hr, 11/06/94	140
6.7	Tidal velocity at $0.4H$ (a), and SSC at $0.25H$ (b) and at $0.75H$ (c) at C2 during a neap tide. Solid lines are simulations and dashed lines represent field data collected during 1000 hr, 11/10/94 to 0900 hr, 11/11/94	140

6.8	Tidal velocity at $0.4H$ (a), and SSC at $0.25H$ (b) and at $0.75H$ (c) at C4 during a spring tide. Solid lines are simulations and dashed lines represent field data collected during 1800 hr, 11/05/94 to 1700 hr, 11/06/94	141
6.9	Tidal velocity at $0.4H$ (a), and SSC at $0.25H$ (b) and at $0.75H$ (c) at C4 during a neap tide. Solid lines are simulations and dashed lines represent field data collected during 1000 hr, 11/10/94 to 0900 hr, 11/11/94	141
6.10	Time series of vertically-averaged SSC during a spring tide (a) and a neap tide (b). During spring tide, the data at sites C1 and C3 began at 1700 hr, 11/04/94 and at sites C2 and C4 at 1800 hr, 11/05/94. During neap tide, the data at sites C1 and C3 began at 1000 hr, 11/12/94 and at sites C2 and C4 at 2300 hr, 11/10/94	145
6.11	Velocity profiles at site C2 during a spring tide. Solid lines are simulations and open circles represent field data obtained during 1900 hr, 11/05/94 to 0600 hr, 11/06/94. Positive values signify flood and negative denote ebb	147
6.12	Velocity profiles at site C2 during a neap tide. Solid lines are simulations and open circles represent data obtained during 1100 hr to 2100 hr, 11/10/94. Positive values signify flood and negative denote ebb	147
6.13	Velocity profiles at site C4 during a spring tide. Solid lines are simulations and open circles represent data obtained during 1900 hr, 11/05/94 to 0500 hr, 11/06/94. Positive values signify flood and negative denote ebb	148
6.14	Velocity profiles at site C4 during a neap tide. Solid lines are simulations and open circles represent data obtained during 1100 hr to 2100 hr, 11/10/94. Positive values signify flood and negative denote ebb	148
6.15	Distribution of transverse (a) and longitudinal (b) currents across the channel due to the Coriolis effect, viewed in the direction of tidal wave propagation. Solid lines are currents in Taizhou Bay and dashed lines in the Jiaojiang	151
6.16	Profiles of gravitational circulation without wind stress (after Hansen and Rattray, 1965)	154
6.17	Tidal currents, vorticities and residual circulation in the neighborhood of a headland. Currents are signified by solid arrows for flood and dashed arrows for ebb. Currents are largest near the headland and decrease towards the shoreline. Vorticity therefore has a maximum near the headland. Vorticities generated by side-wall friction are shown by solid circles for flood and dashed circles for ebb. Vorticities have highest strength near the headland and diminish away from it (after Zimmerman, 1981)	155

6.18	SSC profiles at site C2 during a spring tide. Solid lines are simulations and open circles represent field data obtained during 1900 hr, 11/05/94 to 0600 hr, 11/06/94	156
6.19	SSC profiles at site C2 during a neap tide. Solid lines are simulations and open circles represent field data obtained during 1100 hr to 2100 hr, 11/10/94	156
6.20	SSC profiles at site C4 during a spring tide. Solid lines are simulations and open circles represent field data obtained during 1900 hr, 11/05/94 to 0400 hr, 11/06/94	157
6.21	SSC profiles at site C4 during a neap tide. Solid lines are simulations and open circles represent field data obtained during 1100 hr to 2100 hr, 11/10/94	157
6.22	Time series of vertically-averaged SSC. Dark circles are from site C2, open circles represent site C4. Solid lines signify simulations at C2, dashed lines are simulations at the center of the flow section containing C2 and C4 and dotted lines denote simulations at C4	160
6.23	Comparison of simulated vertically-averaged SSC using uniform and non-uniform boundary conditions for SSC during a spring tide. Solid lines signify simulations at site C2, dashed lines are that at site C4, and dark and open circles represent that using uniform conditions of SSC	161
6.24	Vertical gradient of SSC as a function of elevation during a neap tide. Solid lines are simulations and open circles represent field data obtained during 1100 hr to 2100 hr, 11/10/94	164
6.25	Simulated (solid lines) and measured (dashed lines) tidal variation of the lutocline layer at site C2 during a spring tide from 1800 hr, 11/05/94 to 1700 hr, 11/06/94	165
6.26	Simulated (solid lines) and measured (dashed lines) tidal variation of the lutocline layer at site C2 during a neap tide from 1000 hr, 11/10/94 to 0900 hr, 11/11/94	165
6.27	Simulated (solid lines) and measured (dashed lines) tidal variation of the lutocline layer at site C4 during a spring tide from 1800 hr, 11/05/94 to 1700 hr, 11/06/94	166

6.28	Simulated (solid lines) and measured (dashed lines) tidal variation of the lutocline layer at site C4 during a neap tide from 1000 hr, 11/10/94 to 0900 hr, 11/11/94	166
6.29	Lutocline layer thickness: simulation (δ_{ls}) and measurement (δ_{lm})	167
6.30	Lutocline layer upper elevation: simulation (Z_{us}) and measurement (Z_{um}) ...	167
6.31	Simulated (solid line) and measured (dashed line) hysteresis loops at 1 m above the bottom at C2 during a spring tide from 1800 hr, 11/05/94 to 0500 hr, 11/06/94	169
6.32	Simulated (solid line) and measured (dashed line) hysteresis loops at 1 m below the surface at C2 during a spring tide from 1800 hr, 11/05/94 to 0500 hr, 11/06/94	169
6.33	Simulated (solid line) and measured (dashed line) hysteresis loops at 1 m above the bottom at C2 during a neap tide from 1000 hr to 2100 hr, 11/10/94	170
6.34	Simulated (solid line) and measured (dashed line) hysteresis loops at 1 m below the surface at C2 during a neap tide from 1000 hr to 2100 hr, 11/10/94	170
6.35	Simulated (solid line) and measured (dashed line) hysteresis loops at 1 m above the bottom at C4 during a spring tide from 1800 hr, 11/05/94 to 0500 hr, 11/06/94	171
6.36	Simulated (solid line) and measured (dashed line) hysteresis loops at 1 m below the surface at C4 during a spring tide from 1800 hr, 11/05/94 to 0500 hr, 11/06/94	171
6.37	Simulated (solid line) and measured (dashed line) hysteresis loops at 1 m above the bottom at C4 during a neap tide from 1000 hr to 2100 hr, 11/10/94	172
6.38	Simulated (solid line) and measured (dashed line) hysteresis loops at 1 m below the surface at C4 during a neap tide from 1000 hr to 2100 hr, 11/10/94	172

6.39	Modeling SSC profiles at site C4 during a neap tide. Open circles represent field data from 1100 hr to 2100 hr, 11/10/94, solid lines are simulations with $d_2=0.75$, dashed lines signify simulations with $d_2=0.75$ and $Ri_B=Ri_\mu=0$, and dotted lines represent simulations with $d_2=0$	175
B.1	Schematic diagram of back-tracing approach, where dotted line is the pathline of water particle, o is the position of water particle at current time step $n+1$ and p is the position of water particle at previous time step n	188
C.1	Frequency distribution, ϕ_f , of the settling velocity of kaolinite	194
C.2	Time-concentration relationship during deposition at 26 °C. Open circles are the experimental data of Lau (1994)	194
C.3	Time-concentration relationship during deposition at 20 °C. Open circles are the experimental data of Lau (1994)	195
C.4	Time-concentration relationship during deposition at 10 °C. Open circles are the experimental data of Lau (1994)	195
C.5	Time-concentration relationship during deposition at 5 °C. Open circles are the experimental data of Lau (1994)	196
C.6	Cumulative distribution of settling velocity of kaolinite at different temperatures, θ	196
D.1	Schematic diagram showing the Haldia oil pier and depth contours (m) in the vicinity. Water depth are below mean low water	198
D.2	Location map of Haldia oil pier, India	199
D.3	Measured scour depths in front of the Haldia oil pier. The pier is shown as an idealized rectangular protrusion, Unit: m	201
D.4	Bottom topography of the modeled segment of the river in the vicinity of the Haldia pier. Water depths (unit: m) are below mean low water	201
D.5	Simulated flow field around pier at $0.05H$ below the surface	204
D.6	Simulated flow field around pier at $0.05H$ above the bottom	204

D.7	Comparison of scour depths simulated (solid lines) and measured (dashed lines) in front of the Haldia oil pier. Unit: m	205
D.8	Comparison between simulated and measured areas at 2-3 m (●), 3-4 m (*), 4-5 m (○) and >5 m (+) scour depths	205
E.1	Settling velocity as a function of SSC in moving water. Data are from Mehta (1973)	210
E.2	Simulated flow field around the barrier in the flume, (a) near the surface and (b) near the bottom	212
E.3	Distribution of simulated (solid lines) and observed (numbers in circles) deposition (thickness) at the down side of the barrier. Data are from Ariathurai (1974)	213

LIST OF TABLES

<u>Table</u>	<u>page</u>
3.1	Parameters for momentum and mass diffusion coefficients in a stratified flow . 47
4.1	Summary of Jiaojiang field campaigns 78
4.2	rms height and angular frequency of internal waves as functions of global Richardson number and tidal range 101
4.3	Celerity and length of internal waves 113
6.1	Flow and sedimentary process formulations and parameters 129
6.2	Vertically-averaged maximum velocities at sites C2 and C4 (Unit: $m s^{-1}$) .. 142
6.3	Vertically-averaged SSC during minor and significant non-uniformity of SSC across the flow cross-section (Unit: $kg m^{-3}$) 159
6.4	Average thickness and upper elevation of lutocline layer at different times (Unit: m) 168
E.1	Basic parameters in deposition experiments using the bay mud 208

LIST OF SYMBOLS

- a Sediment-dependent empirical coefficient in Eq. (3.30)
- a_1 Empirical constant in Eq. (3.33)
- a_2 Empirical constant in Eq. (3.34)
- $a_{i+1/2,j}$ Coefficients depending on the time step in Eq. (B.4)
- A_0 Amplitude of the forcing tide at the open boundary (m)
- A_a Coefficient in Eq. (4.19)
- A_E Sediment-dependent constant in Eq. (3.26)
- A_m Measured scour area (m^2)
- A_n Horizontal turbulent momentum diffusion coefficient in the direction normal to the shore boundary ($m^2 s^{-1}$)
- A_s Simulated scour area (m^2)
- A_v Vertical turbulent momentum diffusion coefficient ($m^2 s^{-1}$)
- A_{v0} Vertical momentum diffusion coefficient in homogenous flow ($m^2 s^{-1}$)
- A_{vb} Background value of the turbulent diffusion coefficient of momentum ($m^2 s^{-1}$)

- A_x Horizontal turbulent momentum diffusion coefficient in the x -direction ($\text{m}^2 \text{s}^{-1}$)
- A_y Horizontal turbulent momentum diffusion coefficient in the y -direction ($\text{m}^2 \text{s}^{-1}$)
- b Sediment-dependent empirical coefficient in Eq. (3.30)
- b_1 Empirical constant in Eq. (3.33)
- b_2 Empirical constant in Eq. (3.34)
- b_{ij} Coefficients depending on the time step in Eq. (B.4)
- $b_{ij \neq 1/2}$ Coefficients depending on the time step in Eq. (B.4)
- B Sum of the discretized Coriolis, baroclinic, horizontal diffusion and Bingham yield strength terms
- B_a Coefficient in Eq. (4.19)
- B_b Coefficient in Eq. (4.20)
- \bar{B} Mean width of the estuary (m)
- c Suspended sediment concentration or SSC (kg m^{-3})
- c_0 Prescribed boundary condition
- c_1 Maximum SSC for free settling (kg m^{-3})
- c_2 Maximum SSC for flocculation settling (kg m^{-3})
- c_3 Maximum SSC for hindered settling (kg m^{-3})

- c_b Near-bed SSC (kg m^{-3})
- c_e Prescribed SSC at open boundary (kg m^{-3})
- c_f Initial concentration of deposited sediment (kg m^{-3})
- c_i SSC from outside the modeled domain (kg m^{-3})
- c_{max} Maximum sediment concentration corresponding to grain-grain contact
- c_p SSC of water particle at position p (kg m^{-3})
- c_{s1} Concentration corresponding to the maximum settling flux (kg m^{-3})
- c_{s2} Saturation concentration or the maximum compaction concentration (kg m^{-3})
- c_t Transition concentration (kg m^{-3})
- c_{vmax} Maximum volumetric floc content corresponding to floc-floc contact
- c_λ Linear sediment concentration
- c' Turbulent fluctuation of SSC (kg m^{-3})
- C Vertical mean SSC (kg m^{-3})
- C_0 Initial vertical mean SSC (kg m^{-3})
- C_1 Depth-mean sediment concentration in the upper, mixed, layer of height h_{mix}
(kg m^{-3})

- C_2 Depth-mean sediment concentration in the lower, fluid mud, layer of height h_m
(kg m^{-3})
- C_a Wave speed (m s^{-1})
- C_D Bottom drag coefficient
- C_f Vertically averaged steady state SSC (kg m^{-3})
- C_m Coefficient dependent on the granular density in Eqs. (3.26) and (3.32)
- C_n Vertical mean SSC of n^{th} sediment class (kg m^{-3})
- C_t Lateral friction coefficient
- C_w Water surface drag coefficient
- \bar{C} Bed average dry density or concentration (kg m^{-3})
- C^* Fraction of depositable concentration
- d Grain or floc size of sediment (m)
- d_1 Sediment-dependent coefficient in Eq. (5.24)
- d_2 Sediment-dependent coefficient in Eq. (5.25)
- d_n Grain size of n^{th} sediment class (m)
- dx Total back-tracing distance in the x -direction (m)
- dx^m Back-tracing distance in x direction at time step m (m)

dy	Total back-tracing distance in the y -direction (m)
dy^m	Back-tracing distance in the y -direction at time step m (m)
dz	Height between the <i>in situ</i> measured layers of SSC (m)
$d\sigma$	Total back-tracing distance in the σ -direction
$d\sigma^m$	Back-tracing distance in the σ -direction at time step m
D	Sum of the discretized vertical settling and horizontal diffusion terms
D_E	Sediment-dependent constant in Eq. (3.26)
D/Dt	Total derivative with respect to time
erfc	Complementary error function
f	Coriolis parameter (s^{-1})
F	Temperature function of flocculation
F_a	ASSM signal reading
F_c	Flocculation factor
F_m	Settling flux ($kg\ m^{-2}\ s^{-1}$)
F_{mm}	Maximum settling flux ($kg\ m^{-2}\ s^{-1}$)
F_s	Turbulence energy production ($m^2\ s^{-3}$)
F_t	Transition function
g	Gravitational acceleration ($m\ s^{-2}$)

g_n	Phase lag of the n^{th} tidal harmonic component
g'	Reduced Gravity (m s^{-2})
G	Any physical property
G_p	Any physical property of water particle at position p
h	Undisturbed water depth (m)
h_0	Maximum water depth at the channel center (m)
h_a	Sediment-dependent coefficient in Eq. (4.1) (m)
h_b	Bed thickness (m)
h_m	Fluid mud layer thickness (m)
h_{mix}	Mixed layer thickness (m)
h'	Depth below the acoustic probe (m)
\bar{h}	Mean water depth of the flow cross-section (m)
H	Total water depth (m)
H_0	Initial thickness of the consolidating layer (m)
H_1	Water depth of the upper layer in the two-layer flow system (m)
H_2	Water depth of the lower layer in the two-layer flow system (m)
H_a	Internal wave profile (m)
H_{an}	n^{th} wave height (m)

H_{eff}	Effective water depth defined as the thickness affected by internal waves (m)
H_n	Amplitude of the n^{th} harmonic component (m)
H_s	rms wave height (m)
H'	Thickness of the consolidating layer (m)
I	Number index of the mesh cell centers in the x -direction
j	Number index of the mesh cell centers in the y -direction
k	Number index of the mesh cell centers in the σ or σ' direction (subscript), and wave number
k_0	Deposition rate constant in Eq. (E.1)
k_a	Sediment-dependent coefficient in Eq. (4.1)
k_s	Proportional coefficient between fluid density and salinity
K_0	Constant mass diffusion coefficient ($m^2 s^{-1}$)
K_v	Vertical turbulent mass diffusion coefficient ($m^2 s^{-1}$)
K_{v0}	Vertical mass diffusion coefficient in homogenous flow ($m^2 s^{-1}$)
K_{vb}	Background value of the turbulent mass diffusion coefficient ($m^2 s^{-1}$)
K_x	Horizontal turbulent mass diffusion coefficient in the x -direction ($m^2 s^{-1}$)
K_y	Horizontal turbulent mass diffusion coefficient in the y -direction ($m^2 s^{-1}$)

l	Length of a basin (m)
l_c	Mass mixing length (m)
l_{c0}	Mass mixing length in a homogeneous, non-cohesive flow (m)
l_m	Momentum mixing length (m)
l_{m0}	Momentum mixing length in a homogeneous, non-cohesive flow (m)
l_x	Length of a rectangular domain (m)
l_y	Width of a rectangular domain (m)
l_v	Height of a cubic domain (m)
L_f	Sublayers of the water column in the hydrodynamic and sediment transport model
L_m	Sublayers of the consolidating bottom layer in the consolidation model
L_s	Lutocline strength index
L_λ	Monin-Obukhov length scale (m)
m	Modeling step in the consolidation model and back-tracing calculation (superscript) and summation variable
m_d	Rate of SSC deposition ($\text{kg m}^{-2} \text{s}^{-1}$)
m_e	Rate of bottom sediment erosion ($\text{kg m}^{-2} \text{s}^{-1}$)
m_{en}	Rate of interfacial entrainment (m s^{-1})

- m_i Sediment-dependent constant in Eq. (3.23)
- M Number of mesh grids in the y -direction
- M_b Vertical flux of buoyancy ($\text{kg m}^{-2} \text{s}^{-1}$)
- M_k Classes of sediment
- M_{\max} Maximum erosion rate constant at $\tau_b = 2\tau_s$ ($\text{kg N}^{-1} \text{s}^{-1}$)
- $\vec{M}p^{(k)}$ Working vector at the k^{th} step of water surface elevation iteration according to Eq. (B.5)
- M_z Vertical mass flux ($\text{kg m}^{-2} \text{s}^{-1}$)
- n Modeling step in the hydrodynamic and sediment transport model (superscript), and summation variable
- n_f Manning's bed resistance coefficient
- n_s Direction normal to the lateral solid boundary
- n_i Sediment-dependent constant in Eq. (3.23)
- N Number of mesh grids in the x -direction
- N_a Total number of waves over a period T_a
- N_c Consolidation step
- N_p Subdivided back-tracing step
- N_{Pe} Peclet number

N_i	Total number of tidal harmonic components considered
o	Position of water particle at the current time step $n+1$ (subscript)
p	Position of water particle at the previous time step n (subscript), and water pressure (Pa)
p_d	Probability of sediment deposition
$\vec{p}^{(k)}$	Working vector at the k^{th} step of water surface elevation iteration according to Eq. (B.5)
p_w	Pore water pressure (Pa)
q	Deposition flux minus erosion flux at the bed-fluid interface ($\text{kg m}^{-2} \text{s}^{-1}$)
q_s	Constant source-sink term
$\vec{r}^{(k)}$	Working vector at the k^{th} step of water surface elevation iteration according to Eq. (B.5)
R	Auto-correlation function for internal waves
R_0	Rossby number
R_f	River inflow rate ($\text{m}^3 \text{s}^{-1}$)
Ra	Estuarine Rayleigh number
Ri	Richardson number
Ri_0	Global Richardson number
Ri_B	Ratio of the Bingham yield strength to the Reynolds stress

Ri_s	Stream Richardson number
Ri_μ	Ratio of the viscous force due to interactions between flocs in the fluid mud layer to the Reynolds stress
Ri_ω	Ratio of potential energy of sediment settling flux to the production of turbulent energy
s	Salinity (‰)
S	Spectral density of internal waves ($m^2 s$)
S_0	Salinity at the estuarine mouth (‰)
t	Time (s)
t_{50}	Time corresponding to $c^* = 50\%$ (s)
t'	New time after σ -transformation (s)
t^*	Non-dimensional time
T	Period of tide (hr)
T_a	Duration of each segment of ASSM data (s)
T_d	Period over which σ_d is calculated (s)
T_{El}	Elapsed time
T'	Integration time-limit (s)
u	Horizontal instantaneous velocity in the x -direction ($m s^{-1}$)

- u_g Gravitational circulation (m s^{-1})
- u_{max} Maximum velocity in the x -direction within the modeled domain (m s^{-1})
- u_p Velocity u of water particle at position p (m s^{-1})
- u' Turbulent fluctuation of horizontal velocity in the x -direction (m s^{-1})
- u_* Bottom frictional velocity (m s^{-1})
- u_{*0} Bottom frictional velocity in homogenous, non-cohesive flow (m s^{-1})
- U Vertical mean velocity in the x -direction (m s^{-1})
- U_1 Depth-mean flow velocity in the upper, mixed, layer of height h_{mix} (m s^{-1})
- U_2 Depth-mean flow velocity in the lower, fluid mud, layer of height h_m (m s^{-1})
- U_f Vertical mean inflow velocity (m s^{-1})
- U_w Slip velocity near the bottom (m s^{-1})
- v Horizontal instantaneous velocity in the y -direction (m s^{-1})
- v_{max} Maximum velocity in the y -direction within the modeled domain (m s^{-1})
- v_p Velocity v of water particle at position p (m s^{-1})
- \vec{V}_1 Velocity vector of the modeled layer closest to the bottom (m s^{-1})
- \vec{V}_{n_s} Vector of the normal velocity at the lateral solid boundary (m s^{-1})

V_t	Tangential velocity at the modeled grid closest to the shore boundary (m s^{-1})
w	Vertical instantaneous velocity in the z -coordinate (m s^{-1})
w'	Turbulent fluctuation of vertical velocity in the z -coordinate (m s^{-1})
\vec{W}	Wind velocity vector at a reference elevation (10 m above the water surface in the prototype case) (m s^{-1})
x	Longitudinal Cartesian coordinate located at the mean sea level (m)
x_n	Coordinate normal to the shore boundary (m)
x'	New longitudinal Cartesian coordinate after σ transformation (m)
y^*	Frictional Reynolds number
y	Transverse Cartesian coordinate located at the mean sea level (m)
y'	New transverse Cartesian coordinate after σ -transformation (m)
z	Vertical Cartesian coordinate originating from the mean sea level and positive upward (m)
z_0	Effective roughness of the bed (m)
z_1	Elevation above the bottom of the modeled layer closest to the bottom (m)
z_b	Elevation above bottom (m)
z_l	Lower elevation of the lutocline layer (m)
z_u	Upper elevation of the lutocline layer (m)

z_{um}	Measured upper elevation of the lutocline layer (m)
z_{us}	Simulated upper elevation of the lutocline layer (m)
z'	Vertical coordinate of the consolidating layer originating from the bottom and positive upward (m)
α	Sediment-dependent empirical coefficient in Eq. (3.30)
α_1	Sediment-dependent coefficient in Eq. (3.25)
α_2	Bed-dependent coefficient in Eq. (3.24)
α_a	Sediment-dependent coefficient in Eq. (4.1)
α_B	Sediment-dependent coefficient in Eq. (5.13)
α_g	Constant in the relationship of salinity distribution (6.5)
$\alpha^{(k)}$	Coefficient for the k^{th} step of water surface elevation iteration according to Eq. (B.5)
α_m	The dimensionless variable dependent on SSC in Eq. (5.11)
α_s	Empirical coefficient in Eq. (3.38)
α_t	Linear heat transfer coefficient
α_λ	Empirical constant in Eq. (3.10)
A	Sediment and elevation dependent constant in Eq. (5.20)
β	Sediment-dependent empirical coefficient in Eq. (3.30)
β_1	Sediment-dependent coefficient in Eq. (3.25)

β_2	Bed-dependent coefficient in Eq. (3.24)
β_a	Sediment-dependent coefficient in Eq. (4.1)
β_B	Sediment-dependent coefficient in Eq. (5.13)
β_d	Sediment-dependent constant in Eq. (E.3)
$\beta^{(k)}$	Coefficient at the k^{th} step of water surface elevation iteration according to Eq. (B.5)
β_m	Turbulent Schmidt number
β_n	Positive roots of $\beta \cot \beta + \alpha J = 0$
β_s	Empirical coefficient in Eq. (3.38)
γ_1	Empirical constant in Eq. (3.33)
γ_2	Empirical constant in Eq. (3.34)
δ_l	Lutocline layer thickness (m)
δ_{lm}	Measured lutocline layer thickness (m)
δ_{ls}	Simulated lutocline layer thickness (m)
δ_v	Thickness of current shear layer (m)
ΔH	Thickness of sedimentation (m)
ΔH_{max}	Maximum scour depth (m)
$\Delta H'$	Thickness of deposited sediment over time step Δt (m)

Δt	Time step (s)
$\Delta t'$	Consolidation time step (s)
$\Delta t''$	Back-tracing time interval (s)
ΔT	Time period for the scour hole to be stable (s)
Δx	Horizontal step length in the x -direction (m)
Δy	Horizontal step length in the y -direction (m)
Δz	Incremental depth downward from the bed surface (m)
$\Delta \sigma$	Vertical step length in the σ -coordinate
$\Delta \sigma'$	Vertical step length in the σ' -coordinate
Δ	Sediment-dependent coefficient in Eq. (3.29)
ϵ	Roughness parameter
ζ	Instantaneous water surface elevation (m)
ζ_0	Mean water level (m)
ζ_σ	Lutocline elevation above the bottom (m)
$\vec{\zeta}^{(k)}$	Vector of water surface elevation at the k^{th} step of iteration according to Eq. (B.5)
ζ_r	Lutocline elevation above the bottom detected by the turbidimeter (m)
Z	Vertical distribution function of salinity
θ	Temperature ($^{\circ}\text{C}$)
Θ	Absolute temperature ($^{\circ}\text{K}$)
κ	von Kármán constant
λ	Sediment-dependent coefficient in Eq. (3.29)

λ_a	Wave length (m)
Λ	Sediment-dependent coefficient in Eq. (3.29)
μ	Dynamic viscosity of the fluid mud ($\text{m}^2 \text{s}^{-1}$)
ν	Fluid kinematic viscosity ($\text{m}^2 \text{s}^{-1}$)
ξ	Integration variable in Eq. (3.74) (s)
ρ	Fluid density (kg m^{-3})
ρ_0	Water density (kg m^{-3})
ρ_1	Fluid density of the upper layer in the two-layer flow system (kg m^{-3})
ρ_2	Fluid density of the lower layer in the two-layer flow system (kg m^{-3})
ρ_{air}	Air density (kg m^{-3})
ρ_D	Dry density of the bottom sediment (kg m^{-3})
ρ_f	Bulk density of flocs (kg m^{-3})
ρ_s	Sediment granular density (kg m^{-3})
ρ_ζ	Fluid density at the water surface (kg m^{-3})
ρ'	Turbulent fluctuation of density (kg m^{-3})
$\bar{\rho}$	Vertical mean fluid density (kg m^{-3})
σ	Normalized vertical coordinate in the water column

σ_d	Standard deviation of SSC
σ'	Normalized vertical coordinate of the consolidating layer
τ	Shifting time and integration variable in Eq. (4.2) (s)
τ_b	Bottom shear stress (Pa)
$\vec{\tau}_b$	Vector of bottom shear stress (Pa)
τ_b^x	Bottom shear stress in the x -direction (Pa)
τ_b^y	Bottom shear stress in the y -direction (Pa)
τ_b'	Bottom shear stress at the point where the maximum scour appeared (Pa)
τ_B	Bingham yield strength (Pa)
τ_d	Critical shear stress for deposition (Pa)
τ_{d1}	Minimum critical shear stress for deposition of the M_k sediment classes (Pa)
τ_{dM}	Maximum critical shear stress for deposition of the M_k sediment classes (Pa)
τ_R	Reynolds stress (Pa)
τ_s	Bed shear strength for erosion (Pa)
τ_{s0}	Shear strength of newly deposited bottom sediment (Pa)
τ_s'	Critical shear stress at the point of maximum scour (Pa)
τ_i	Total (normal) stress (Pa)

$\bar{\tau}_w$	Vector of wind-induced water surface stress (Pa)
τ_w^x	Wind-induced water surface stress in the x -direction (Pa)
τ_w^y	Wind-induced water surface stress in the y -direction (Pa)
τ_{zx}	Shear stress near the bottom (Pa)
τ_μ	Shear stress due to the interactions between flocs (Pa)
$\tau_{\mu\beta}$	Shear stress due to cohesion and interactions between flocs (Pa)
τ'	Effective (normal) stress (Pa)
T	Dimensionless wind stress
ϕ	Solid weight fraction
ϕ_c	Critical solid weight fraction
ϕ_d	Dynamic angle of repose ($^\circ$)
ϕ_f	Frequency distribution of sediment
ϕ_l	Latitude ($^\circ$)
χ	Sediment-dependent coefficient in Eq. (3.29)
X	Dimensionless horizontal coordinate
ψ	Stratification function
ω	Vertical instantaneous velocity in the σ -coordinate (s^{-1})
ω_0	Angular frequency of the forcing tide at the open boundary ($rad\ s^{-1}$)

- ω_{0n} Settling velocity of the n^{th} sediment class (m s^{-1})
- ω_a Angular frequency of the internal waves (rad s^{-1})
- ω_n Angular frequency of the n^{th} tidal harmonic component (rad s^{-1})
- ω_s Sediment settling velocity (m s^{-1})
- ω_{s0} Flocculation settling velocity at 15 °C
- ω_{s1} Minimum flocculation settling velocity of the M_k sediment classes (m s^{-1})
- ω_{sb} Near-bed settling velocity (m s^{-1})
- ω_{sc} Rate of consolidation (m s^{-1})
- ω_{sf} Free settling velocity (m s^{-1})
- ω_{sc1} Rate of consolidation for the first mode (m s^{-1})
- ω_{sc2} Rate of consolidation for the second mode (m s^{-1})
- ω_{smax} Maximum flocculation settling velocity (m s^{-1})
- ω_{sM} Maximum flocculation settling velocity of the M_k sediment classes (m s^{-1})
- ω_{sn} Flocculation settling velocity of the n^{th} sediment class (m s^{-1})
- ω_v Brunt-Väisälä frequency (rad s^{-1})
- ω' Angular frequency (rad s^{-1})

- Ω Angular frequency of earth's rotation (rad s^{-1})
- ε Allowed error in the iteration of water surface elevation

Abstract of Dissertation Present to the Graduate School
of the University of Florida in Partial Fulfillment of the
Requirements for the Degree of Doctor of Philosophy

AN EXAMINATION OF ESTUARINE LUTOCLINE DYNAMICS

By

JIANHUA JIANG

August, 1999

Chairman: Dr. Ashish J. Mehta

Major Department: Coastal and Oceanographic Engineering

Three dynamical features associated with estuarine lutoclines are examined with special reference to data from the Jiaojiang estuary in China. These features include turbulence damping induced by high suspended sediment concentration, internal wave behavior at the lutocline, and the response of the lutocline to tidal forcing. It is shown that turbulence damping is governed by the settling flux, cohesion, interaction between flocs and sediment-induced stratification. Maximum turbulence damping in the water column occurs at the lutocline, a finding which supports previous, qualitative observations of a similar nature. Expressions for the vertical momentum and mass diffusion coefficients incorporating these effects have been developed.

Observations from the Jiaojiang are examined for the height, angular frequency, celerity and length of internal waves at the lutocline. Both deep water high and shallow water

low frequency waves are identified. The low frequency, at 0.09 rad s^{-1} , is shown to be close to the local Brunt-Väisälä frequency. The high frequency wave at 1.33 rad s^{-1} is possibly induced by interfacial shear, and is characterized by sharp crests and flat troughs. The height and the angular frequency of both wave types are shown to decrease with increasing Richardson number.

Lutocline variation with tide in the Jiaojiang is examined by applications of three-dimensional, finite-difference codes developed for flow and sediment transport. It is shown that lutocline responses reflect the cumulative effects of sediment settling and entrainment, turbulence damping and tidal asymmetry.

CHAPTER 1 INTRODUCTION

1.1 Problem Statement

A lutocline is a step structure in the vertical profile of fine-grained suspended sediment concentration (SSC), and is a critically important pycnocline in addition to salinity and temperature gradients governing estuarine dynamics (Parker and Kirby, 1979). From experiments in the field and the laboratory in recent years, the lutocline's significance in governing the vertical mixing of suspended sediment and sedimentation patterns has been assessed (e.g., Kirby, 1986; Wolanski, et al., 1989; Mehta and Srinivas, 1993; Winterwerp and Kranenburg, 1997). As a result, it is now recognized that lutocline formation and strength are controlled by numerous factors including tidal currents, interfacial waves formed at the lutocline, turbulence damping in the fluid mud layer beneath the lutocline, floc settling, suspended sediment deposition, bottom erosion, and consolidation of deposits. Unfortunately, the inter-linkage among these unit processes has yet to be quantified on theoretical grounds for an accurate prediction of lutocline dynamics. There is a critical need for such a quantification, due to the importance of predicting fine-grained sediment transport in estuarine engineering applications.

Turbid water is a characteristic feature of estuarine zones with high-load fine sediments, especially around turbidity-maxima, sedimentary fronts, and dredging disposal

sites. In such cases, the spatial distribution of SSC and the horizontal transport of sediment are significantly associated with the high concentration distribution near the bottom, i.e., the lutocline and fluid mud. Lutoclines frequently can cause significant problems due to associated sedimentation in engineering projects, especially where the natural environment is dramatically altered by dredging operations or erection of structures.

Prediction of lutocline dynamics is presently hindered by a lack of adequate understanding of lutocline-associated processes, namely the influence of SSC on turbulence damping, hence diffusion, and the response of the lutocline interface to shear flow that leads to interfacial waves and vertical mixing.

A high degree of turbulence damping is known to occur in the fluid mud layer (Wolanski, et al., 1992; Kranenburg and Winterwerp, 1997). Hence, vertical diffusion and mixing at the lutocline are influenced not only by the sediment-induced buoyancy force, but also by turbulence damping. It has also been shown that the characteristic, upward-asymmetric, sediment entrainment caused by the instability and breaking of internal waves at the lutocline occurs concurrently with high turbulence damping (Jiang and Wolanski, 1998). However, there remains a lack of detailed theoretical analyses and direct evidence of turbulence damping because of the difficulty in observing turbulent damping both in the field and in the laboratory.

Substantial efforts have been devoted to understanding lutocline response to tidal forcing (e.g., Wolanski, et al., 1988; Smith and Kirby, 1989; Costa and Mehta, 1990; Dong, et al., 1997). It is found that the elevation and strength (i.e., the steepness and size of the SSC

step structure) of the lutocline vary with the tidal cycle under the combined effects of the strongly current-dependent vertical and horizontal sediment transport processes. However, a comprehensive quantification of lutocline response to tide is still difficult because of limited field data and process-based formulations for the interactions between SSC and flow as noted. This difficulty in quantification and the consequent need to examine SSC-flow interaction was the main motivation behind the present study.

1.2 Objectives

In accordance with the above discussion, the objectives of the investigation were set as follows:

1. To examine the effects of high SSC on the turbulent mixing length over the estuarine water column, and develop an expression for the vertical diffusion coefficient accounting for these effects.

2. To investigate the behavior of the interfacial waves at the lutocline, as a basis for an improved understanding of the vertical mixing processes at the interface.

3. To develop a numerical code for estuarine flow and fine sediment transport, incorporating the latest unit process models for sediment transport including erosion/entrainment, diffusion, settling, deposition and consolidation.

4. To test the model against laboratory data and analytical solutions, and apply the model to extensive field data obtained at Jiaojiang estuary in China, as a means to comment on the utility of the model.

1.3 Tasks

With respect to the above objectives, the specific tasks established to conduct the study consist of the following:

1. Review of Previous Studies: Previous studies on sedimentary process in fine sediment dominated estuarine environments are reviewed, thereby providing the groundwork for the subsequent tasks.

2. Theoretical Analyses: A analytical model for vertical diffusion in the water column is developed and incorporated in the numerical model for the flow and sediment transport developed to examine tide-induced lutocline dynamics (see below).

3. Flow and Sediment Transport Model: A three-dimensional, finite-difference scheme numerical model code is developed. This code consists of two major parts, namely, a flow model (called Coastal and Estuarine Hydrodynamic model - University of Florida or COHYD-UF) and a fine-grained sediment transport model (called Coastal and Estuarine Cohesive Sediment model - University of Florida or COSED-UF). The model system focuses on fine sediment transport processes and flow-sediment coupling due to sediment-induced stratification and turbulence damping in the fluid mud layer.

4. Model Parameters: All parameters defining the flow and sediment transport processes required for COHYD-UF and COSED-UF are determined from works of previous researchers, model calibrations as well as prototype data analysis.

5. Modeling Tests: For validation, COHYD-UF and COSED-UF are tested against some special forms of the governing equations having exact or approximate solutions, as well as laboratory and field data. The sub-models for consolidation of deposits and interfacial

entrainment are tested against experimental data of previous researchers. Further tested are the ability of the developed model in predicting local scour using data at a pier in a river (Appendix D), and sedimentation behind a piled structure using flume test data (Appendix E).

6. Field Data Analysis: Through analysis of field data from the Jiaojiang estuary, the following tasks are carried out: (1) Examination of the behavior of internal waves at the lutocline in conjunction with previous analyses; and (2) Examination of lutocline and fluid mud response to tidal forcing.

1.4 Thesis Outline

This study is presented in the following order. Chapter 2 introduces the vertical structure of fine sediment suspension, definitions of lutocline and fluid mud layers, causes of fluid mud and lutocline generation, influence of lutocline on turbidity transport, and a review of turbidity dynamics in several estuaries.

Chapter 3 describes model formulations including the governing equations and the boundary conditions for flow and sediment transport, reviews of previous studies on flow-sediment transport processes, and the respective mathematical formulas. Lastly, the results of model tests are reported for hydrodynamics and sediment transport.

Analysis of field data and the results for the behavior of internal waves, tides, SSC, settling velocity and erosion rate in the Jiaojiang are covered in Chapter 4. Also introduced in this chapter are previous models for the behavior of internal wave height, angular frequency, celerity and wave length at haloclines and thermoclines. These models are used to explain the behavior of internal waves detected in the Jiaojiang.

Chapter 5 presents an analytical model for the turbulent mixing length and the associated diffusion coefficient. Data from the Jiaojiang are used to examine the validity of the model.

Chapter 6 summarizes the hydrodynamic and sedimentary formulations and parameters for numerical model application to the Jiaojiang. Simulations of lutocline and fluid mud dynamics in the Jiaojiang and their comparisons with data are then presented.

Based on above results, major conclusions derived from this study are summarized in Chapter 7.

Appendix A provides derivations of the governing equations for hydrodynamics and sediment transport with respect to σ -transformation.

Appendix B describes the numerical technique, including the back-tracing approach used in the discretization of the inertial terms in hydrodynamic and sediment transport equations, and the pre-conditioned conjugate gradient method used in solving the finite differential equation for the water surface elevation.

Appendix C presents the analyzed results for the effects of temperature on cohesive sediment settling using the experimental data of previous researchers.

Appendix D presents the simulated results of contraction scour at the Haldia Pier, in the Hooghly River in India using COHYD-UF, and a comparison with observations in the field.

Appendix E presents the simulated results of sediment deposition pattern behind a piled barrier carried out in a flume test and comparison with experimental observations.

CHAPTER 2 LUTOCLINES IN ESTUARIES

2.1 Vertical Structure of Fine Sediment Suspension and the Lutocline

A typical instantaneous sediment concentration profile and associated velocity profile is schematically shown in Figure 2.1, as might be observed in a macro- or meso-tidal estuarine environment with high fine-grained sediment loads (Mehta, 1989; 1991a). A noteworthy characteristic of the vertical profile of the suspended sediment concentration (SSC) is the multiple step structures identified as secondary lutoclines and the primary lutocline. A secondary lutocline (Mehta and Li, 1997) has a relatively low SSC, generally $\sim 1.0 \text{ kg m}^{-3}$, and is induced by the coupling between concentration dependent settling velocity (i.e., settling velocity increasing with SSC as the flocs become stronger, larger and denser in the flocculation settling mode; see Figure 2.2), and the SSC gradient dependent diffusion (i.e., the upward mass diffusion retarded by this gradient due to negative buoyancy). The primary lutocline is a significant pycnocline which occurs near the bottom. It is characterized by a high value of SSC, generally $> \sim 5\text{-}10 \text{ kg m}^{-3}$, and a significant vertical gradient of SSC. It is formed due to a high sediment settling flux above it and high turbulence damping as well as hindered settling; see Figure 2.2 below (Ross and Mehta, 1989; Mehta and Li, 1997).

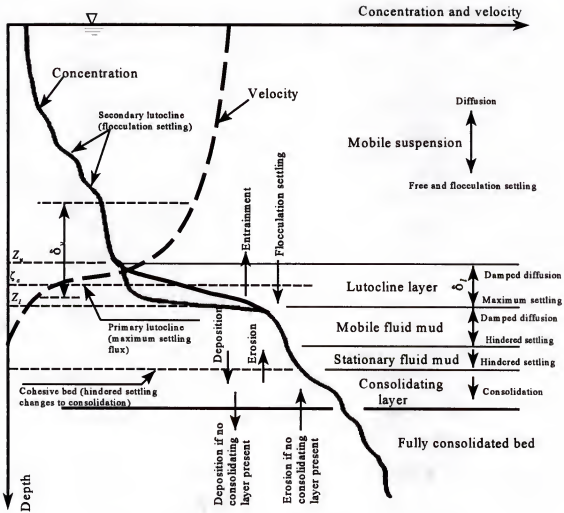


Figure 2.1. Vertical SSC profile classification and associated velocity profile. Also shown are unit transport processes which govern concentration profile dynamics (after Mehta, 1989; 1991a).

As shown in Figure 2.1, the primary lutocline tends to separate the water column into two reasonably well-defined zones. The near-bottom, non-Newtonian flow zone is characterized by high SSC, generally $> \sim 5\text{-}10 \text{ kg m}^{-3}$, hindered settling, turbulence damping, turbidity underflow, a sediment-modified velocity profile, etc. On the other hand, the overlying zone, generally having $\text{SSC} < 1.0 \text{ kg m}^{-3}$ and exceeding $2\text{-}3 \text{ kg m}^{-3}$ during extreme energy events, is marked by free or flocculation settling (Figure 2.2), a higher level of turbulence and near-Newtonian flow properties.

The typical SSC profile can be sub-divided into a layer of mobile suspension, the lutocline layer, mobile fluid mud, stationary fluid mud, a consolidating mud layer and the fully consolidated bed. The lutocline layer is characterized by a thickness δ_l , between the upper elevation, Z_u , and lower elevation, Z_l , of the vertical gradient of SSC (Figure 2.1). The characteristic elevation of the lutocline above the bottom, ζ_a , is within the lutocline layer. Approximately at elevation Z_l , the lutocline layer transitions to layers consisting of horizontally mobile and horizontally stationary fluid muds (Figure 2.1). Within the stationary fluid mud layer, the sediment is maintained in suspension by turbulent diffusion. Below this is the consolidating mud layer.

2.2 Causes of Fluid Mud and Lutocline Generation

As noted, the primary lutocline is characterized by a steep vertical gradient of SSC and occurs within a thin transition zone (or the lutocline layer) from the upper mobile suspension to the lower fluid mud (Ross, 1988). Thus, the lutocline occurs concurrently with

the fluid mud. The formation of fluid mud and lutocline are dependent on complex erosion, deposition and mixing-settling processes, high turbulence damping due to settling flux (Einstein and Chien, 1955), cohesion, interactions between flocs (Bagnold, 1954 and 1956), and the buoyancy effect due to sediment-induced stratification (Ross and Mehta, 1989). A general description of the settling behavior as well as causes of fluid mud and lutocline generation are given in the following sections.

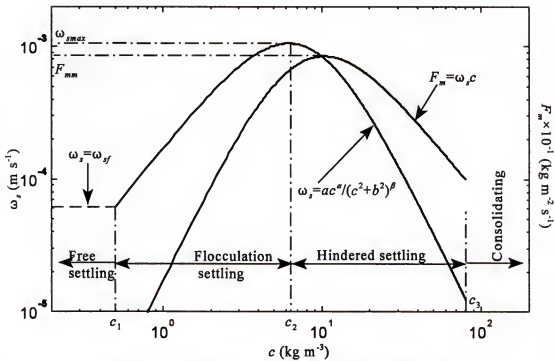


Figure 2.2. A representative description of settling velocity and flux variation with SSC (after Mehta and Li, 1997).

2.2.1 Settling Velocity

In water with salinity $>0.1-0.5\%$, the settling velocity, ω_s , of cohesive sediment is strongly dependent on SSC ($=c$), and can be divided into three sub-ranges in terms of concentration. These ranges are free settling ($c < c_1$), flocculation settling ($c_1 < c < c_2$) and hindered-settling ($c > c_2$) with the maximum SSC for free settling $c_1 = 0.1 - 0.3 \text{ kg m}^{-3}$, the maximum SSC for flocculation settling $c_2 = 5 - 10 \text{ kg m}^{-3}$ (Mehta and Li, 1997) and the maximum SSC for hindered settling $c_3 = \sim 80 \text{ kg m}^{-3}$ (Odd and Rodger, 1986). Free settling occurs at low SSC when the settling velocity is independent of concentration. In the flocculation range, the settling velocity increases with concentration due to the formation of stronger, denser and larger flocs with increasing concentration. In the hindered range, the occurrence of an aggregated particulate network inhibits the upward escape of the interstitial water present within the deposit. As a result, the settling velocity decreases with increasing SSC. Figure 2.2 gives a representative description of the settling velocity and the settling flux $F_m (= \omega_s c)$, variation with SSC, where a , b , α and β are sediment-dependent empirical coefficients in the combined relationship between the settling velocity and SSC for the flocculation and the hindered settling regions, ω_{sf} is the free settling velocity, ω_{smax} is the maximum flocculation settling velocity, and F_{mm} is the maximum settling flux.

2.2.2 Formation of Fluid Mud

Fluid mud can form during rapid erosion or deposition. During erosion, if the erosion rate greatly exceeds the net upward flux due to sediment diffusion and settling, i.e., the rate at which sediment is mixed by turbulence into the upper column mobile suspension layer, the SSC near the bottom continues to increase and tends to lead to the formation of fluid mud (Maa and Mehta, 1987). During deposition, if the sediment deposition flux exceeds the rate of upward transport of the pore fluid (i.e., the dewatering rate of the suspension), a dense near-bed suspension is formed, grows upward and consolidates slowly (Ross, 1988). Once a fluid mud layer forms, it is stabilized by buoyancy and may be enhanced by high turbulence damping and hindered settling as well as further erosion or deposition (Maa and Mehta, 1987; Ross and Mehta, 1989).

2.2.3 Formation of Lutocline

Based solely on the concept of density stratification, the lutocline behaves, at least qualitatively, like a halocline or a thermocline. Both the lutocline and other pycnoclines are characterized by the coincidence of a vertical maximum in the concentration gradient and minimum vertical mixing (Ross and Mehta, 1989). The local minimum in mixing due to the buoyancy effect is associated with the concentration gradient. However, there are two significant differences between a lutocline and other pycnoclines as follows:

(1) Sediment settling occurs with respect to the fluid. This has the effect of further enhancing the stability of the lutocline for a given set of flow conditions (Ross and Mehta, 1989). Based on the non-linear variation of the settling velocity with concentration (Figure 2.2), at the maximum settling flux the gradient of $\partial F_m / \partial c$ must be equal to zero, i.e.,

$$\frac{\partial F_m}{\partial c} = \frac{\partial F_m / \partial z}{\partial c / \partial z} = 0 \quad (2.1)$$

where z is the vertical coordinate. Note that the vertical gradient of settling flux is not equal to zero, i.e., $\partial F_m / \partial z \neq 0$, due to the high gradient of SSC at the lutocline. Thus, only as $\partial c / \partial z \rightarrow \infty$, Eq. (2.1) is satisfied. This analysis supports the observation that discontinuities in the concentration profile are generated at elevations where the maximum settling flux F_{mm} occurs.

(2) High turbulence damping occurs in the fluid mud layer due to the settling flux, cohesion and interactions between flocs as well as the sediment-stratified buoyancy effect. Turbulence damping decreases vertical mixing and consequently enhances the lutocline (discussed in details in Chapter 5).

From the above it can be expected that the lutocline would be much more persistent in the macro-tidal environments than the halocline and the thermocline (Ross and Mehta, 1989). This inference has been confirmed from field data taken in the Severn estuary, U.K. (Kirby, 1986), with a spring tide range of ~ 15 m, and in the Jiaojiang (Dong, et al., 1993, Guan, et al., 1998 and Jiang and Wolanski, 1998), with a spring tide range of 6.3 m. At these sites, lutoclines have been observed to persist through most of the tidal cycle, even during spring tides.

2.3 Influence of Lutocline on Turbidity Transport

In a stratified flow, vertical mixing is damped due to the buoyancy force because work must be done to raise heavy fluid parcels and lower lighter parcels. As noted, in the case of the lutocline the mixing process is further complicated by sediment settling, cohesion (Hopfinger and Linden, 1982; Ross and Mehta, 1989) and interactions between flocs (Bagnold, 1954; 1956). Thus, additional work is required to keep the sediment in suspension and overcome cohesion and interactions between flocs.

Without explicitly considering settling, cohesion and interactions between flocs, the mixing process over the lutocline can be simply demonstrated with reference to a sediment-induced two-layer flow with initial densities ρ_1 and ρ_2 , and identical depths $H_1 = H_2 = H/2$; this system representing a fluid mud layer beneath clear water moving parallel to the x -direction with velocities U_1 and U_2 , respectively (Figure 2.3). After some time complete mixing is assumed to take place, and the system now consists of single layer of mean density, $\bar{\rho} = (\rho_1 + \rho_2)/2$, flowing with mean velocity, U . Because initially the heavier fluid (of density ρ_2) lies below the lighter fluid (of density ρ_1), the center of gravity of the system is below mid-depth level, whereas in the final state it is exactly at mid-depth. Thus, the center of gravity is raised in the mixing process, for which a potential energy PE must be provided to the system according to

$$PE = \int_0^H \bar{\rho} g z dz - \left\{ \int_0^{H_1} \rho_2 g z dz + \int_{H_1}^{H_2} \rho_1 g z dz \right\} = \frac{1}{8} (\rho_2 - \rho_1) g H^2 \quad (2.2)$$

where g is the gravitational acceleration. The source of potential energy increase, PE , must be from the externally imposed kinetic energy so long as the initial velocity distribution is uneven. Conservation of linear momentum in the absence of the effects of settling, cohesion and interactions between flocs implies that the final, uniform velocity is the mean of the initial velocities of each layer, i.e., $U = (U_1 + U_2)/2$, thus leading to a kinetic energy loss, KE , given by

$$KE = \left\{ \int_0^{H_1} \frac{1}{2} \rho_2 U_2^2 dz + \int_{H_1}^{H_2} \frac{1}{2} \rho_1 U_1^2 dz \right\} - \int_0^H \frac{1}{2} \bar{\rho} U^2 dz = \frac{1}{8} \bar{\rho} (U_1 - U_2)^2 H \quad (2.3)$$

Here, the Boussinesq approximation, $\rho_1 \approx \rho_2 \approx \bar{\rho}$, has been invoked (Lesieur, 1997).

Complete vertical mixing is possible as long as the kinetic energy loss exceeds the potential energy gain, i.e.,

$$\frac{(\rho_2 - \rho_1)gH}{\bar{\rho}(U_1 - U_2)^2} < 1 \quad (2.4)$$

Therefore, the initial density difference must be sufficiently weak in order not to present an insurmountable gravitational barrier, or alternatively, the initial velocity-shear induced at the interface must be sufficiently large to supply the necessary amount of energy. When criterion (2.4) is not met, mixing occurs only in the vicinity of the initial interface and cannot extend over the entire system. This situation can result in interfacial instabilities (Delisi and Corcos, 1973). This phenomenon will be further discussed in Section 4.4.2.

Vertical mixing is also highly dependent on the nature and intensity of turbulence in both layers. As stated in Section 1.1, an upward-asymmetric mixing caused by the instability and breaking of internal waves at the lutocline occurs concurrently with high turbulence damping in the fluid mud layer.

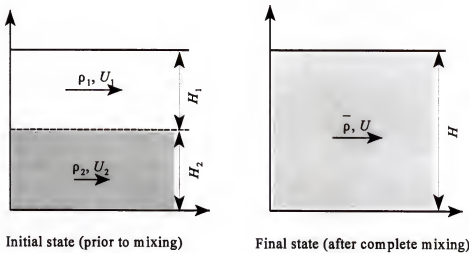


Figure 2.3. Mixing of a two-layer stratified fluid, with fluid mud beneath clear water.

2.4 Dynamics of Turbid Estuaries

Over the past decades there has been an increasing number of studies on the dynamics of lutocline and fluid mud through combined physical and mathematical approaches and *in situ* measurements of sediment movement. This has been made possible by improved instrumentation such as the optical backscatter sensors, e.g., turbidimeters and nephelometers (Wolanski, et al., 1988), and acoustic backscatter sensors, e.g., the recently developed Acoustic Suspended Sediment Monitors or ASSM (Shi, 1997). Improvements have also occurred in designing advanced methods of recording large quantities of data and computer

analysis techniques. The following sections briefly describe the works of previous researchers in some of the turbid estuaries of the world.

2.4.1 Amazon Shelf

The Amazon continental shelf in Brazil is the offshore region extending from the mouth of the Amazon River. This river is one of the world's largest with the highest fresh water outflow; the annual mean rate of about $210,000 \text{ m}^3 \text{ s}^{-1}$ is 18% of the global riverine discharge. The Amazon also has one of the largest fluvial sediment discharge of about $1.2 \times 10^9 \text{ tons yr}^{-1}$, or 10% of the global sediment output to the sea (Kineke, 1993). The shelf region can be considered as an estuary because the fresh water discharge is so large that low salinities (e.g., 20‰) occur 100 km from the river mouth and 100 km offshore.

Measurements of SSC and sediment transport were made over the middle and inner Amazon shelf region during four oceanographic cruises between August 1989 and November 1990 using OBS sensors (range $0\text{-}36 \text{ kg m}^{-3}$), CTD probes, current meters and a data logger mounted on a tripod frame (AmasSeds Research Group, 1990). Silt- and clay-size sediments were found to dominate the bottom. A major characteristic of the suspended sediment was the vast extent of high-concentration near-bed suspension (or fluid mud), which accounted for most of the suspended sediment inventory on the shelf. Fluid muds generally were observed in the region of the turbidity maximum. Fluid mud of up to 7 m in thickness on the inner and middle shelf was found to cover an extensive region, ranging from 5,700 to 10,000 km^2 , in water depths as great as 40 m. Observed SSC near the surface of the shelf ranged from 0.01 to $>0.54 \text{ kg m}^{-3}$. SSC in fluid mud layer ranged from 10 to 100 kg m^{-3} with a

sharply decrease of SSC above, thus marking a distinct lutocline. Much of the inner shelf mud deposit was found to accumulate sediment at a rate exceeding 2 cm yr^{-1} .

2.4.2 Ariake Bay

Ariake Bay in southern Japan is dominated by semi-diurnal tides with a spring range of 3.86 m and a neap range of 1.54 m. The maximum tidal velocity is in the range of 0.3-0.5 m s^{-1} . A great amount of fine sediment is transported from the mountain area to the bay through two main rivers, which lead to a wide tidal flat near Kumamoto City. The bed material offshore consists of fine clay and silt, and fine sand and silt occur nearshore. Extensive field measurements have been carried out at Kumamoto Port in order to obtain information on the sedimentation mechanism in the port area (Tsuruya, et al., 1990a).

In field surveys, an echo-sounding measuring pole (measuring sedimentation volume), electro-magnetic current meters and turbidity meters were employed. A noteworthy engineering project was the selection of a submerged dike for reducing deposition within the navigation channel. A multi-layered numerical model was used to take into account the effects of the dike and to reproduce the vertical distribution of suspended mud particles in the port area (Tsuruya et al., 1990b). It was found that there was a strong correlation between the wave-induced oscillatory current and turbidity concentration. High concentrations occurred at low tide when wave heights were large. Maximum concentrations were about 1.0 kg m^{-3} . SSC greater than 10.0 kg m^{-3} was observed near the bottom with a steep vertical gradient of SSC (or lutocline). It was also found that net bottom erosion took place when the wave height was large and tidal level low. It was concluded that the bottom sediments around

Kumamoto Port were eroded mainly by shear stress induced by wind waves (Tsuruya et al., 1990a).

2.4.3 Gironde River

The Gironde River estuary in France is one of the largest estuaries of the European Atlantic coast. It has an annual mean inflow rate on the order of $1,000 \text{ m}^3 \text{ s}^{-1}$, and the tidal range varies from 2 to 6 m at the mouth. The range increases towards the upper estuary due to the convergence effect of the estuarine shape, and tides propagate up to 170 km upstream during low river inflow periods. Turbidity maximum is an important feature of this estuary. Numerous studies on the dynamics of this turbidity maximum have been made through field investigations (e.g., Allen, et al., 1976; Castaing and Allen, 1981), as well as depth-averaged and three-dimensional numerical modeling (Sottolichio, et al., 1999).

In order to examine the resuspension and dispersion of fluid mud in zone of the turbidity maximum, a tracer study was carried out using sediments labeled with radioactive Scandium 46. Five kilos of labeled, naturally occurring, fluid mud were injected into a fluid mud pool in a channel during a neap tide in May, 1974. It was shown that the high turbidity zone was characterized by SSC ranging between 1 to 10 kg m^{-3} (Allen et al., 1976). During slack water periods, and especially at neap tides, suspended sediment settling was enhanced, and thick patches of fluid mud appeared on the channel bottom with concentrations up to 300 kg m^{-3} . The estimated total sediment mass contained in the turbidity maximum-fluid mud system was found to reach up to 5×10^6 tons (Castaing and Allen, 1981). It was also determined that in this estuary, tidal pumping is the major mechanism of the formation of the

turbidity maximum (Sottolichio, et al., 1999). Large-scale lateral transport of suspended sediment occurs within the turbidity maximum, resulting in a general northward drift of the sediment. This lateral transport occurs by advection, while the rates of lateral sediment diffusion appear to be low (Allen, et al., 1976).

2.4.4 Hangzhou Bay

Hangzhou Bay on the coast of East China Sea is the outer region of the Qiantang River estuary with an average inflow of $4.2 \times 10^{10} \text{ m}^3 \text{ yr}^{-1}$, and an average suspended sediment load of $7.9 \times 10^6 \text{ ton yr}^{-1}$. This bay is a typical funnel-shaped estuary with a length of about 100 km and an average depth of 10 m. Its width decreases from 90 km at the mouth to 20 km at its western end. The tidal range is about 3 m at the mouth and increases rapidly landward. A tidal bore develops about 10 km further upstream of the bay (Su, et al., 1992). Sediment in the bay is predominantly fine and medium silt with the median size of the suspended load ranging from 10 to 13 μm and that of the bed about 16 μm (Costa and Mehta, 1990).

Available *in situ* data are from the following three surveys: (1) observations in the bay carried out from 13th to 21th of December, 1987 and from 22th of July to 2th of August, 1988 using Partech 7000-3RP turbidimeter and ENDECO 174 current meter, aimed at understanding of the plume front and its role in suspended sediment transport (Su, et al., 1992); (2) Measurements of lutocline and flow-fine sediment hysteresis near the south shore were conducted between 14th and 16th of May, 1988, deploying a pressure gage, two turbidimeters (Partech SDM16) and two electromagnetic current meters mounted on a tower

(Costa and Mehta 1990); and (3) Fluid mud and interfacial waves in a proposed navigational channel observed at a neap tide (October 23, 1993) using a ship-borne ASSM, soon after a dredging operation (Shi,1998). Horizontal, two-dimensional, numerical modeling of the depositional patterns in Hangzhou Bay was carried out by Su and Xu (1984). It was found that the tidal bore there traps the fine fluvial sediments. A persistent, year-around NE-SW suspended sediment concentration front was found to exist inside the bay. This front acts to concentrate suspended sediment and transport it southwestward into the bay (Su, et al., 1992). ASSM data showed that high concentration suspensions ($SSC > 10 \text{ kg m}^{-3}$) appeared close to the mud bed, occupying 30% of the water column. The ASSM also detected a relatively well defined wave train with a wave period of about 144 s superimposed by higher frequency oscillations with periods of a few seconds (Shi, 1998). Due to the presence of the lutocline, reversals of flow-fine sediment hysteresis was observed during the transition from accelerating to decelerating flows (Costa and Mehta, 1990).

2.4.5 James River

The James River estuary in Virginia discharges into the south end of the Chesapeake Bay. Extensive surveys of the vertical profiles of SSC, tidal currents and sediment-water interface were conducted using an optical turbidimeter, an electromagnetic current meter and a nuclear transmission density probe, all mounted on a tripod frame (Nichols, 1984-1985). It was shown that the flood peak at 6 cm above the bed reached 0.24 m s^{-1} , whereas the ebb reached 0.30 m s^{-1} . Fluid mud accumulated mainly as shallow pools and blanket deposits greater than 0.2 m in thickness in the channel depressions in the middle reach of the estuary.

This occurred mainly in the turbidity maximum zone, a site of high near-bed concentration ($0.5\text{-}2.0 \text{ kg m}^{-3}$), intensive resuspension and rapid sedimentation ($10\text{-}80 \text{ kg m}^{-2} \text{ yr}^{-1}$). Measurements of mud density and thickness from 85 continuous densitometer profiles revealed two basic types of profiles: (1) those with an abrupt increase in density with depth to more than $1,200 \text{ kg m}^{-3}$ in the upper 1-2 cm, i.e., mainly settled mud, and (2) those with a moderate increase in density with depth in the density range $\sim 1,003\text{-}1,200 \text{ kg m}^{-3}$ in the upper 2-30 cm. It was found that accumulation of fluid mud was promoted by stratification of the interfacial fluid and pore water, by the pseudoplastic behavior of the mud with relatively high viscosity at low shear rates, by the high suspended sediment concentrations, and by the resultant rapid-settling flux in the hindered state relative to the consolidation rate.

2.4.6 Orinoco River

The Orinoco River delta is located in a coastal plain extending from the Guyana shield in the south to the Venezuelan cordillera in the north. The river discharges through the delta with an annual mean outflow of about $17,000 \text{ m}^3 \text{ s}^{-1}$ and total suspended load on the order of $10^8 \text{ tons yr}^{-1}$ (Eisma, et al., 1978). Bottom deposits sampled in the delta (Eisma, et al., 1978) were essentially mixtures of silt and clay-size materials, with generally low sand content (less than 10%).

Turbidity was measured using the radiometric method (Goldberg and Bruland, 1974). A layer of hyper-concentrated suspended material (i.e., fluid mud layer) with concentrations reaching 500 kg m^{-3} was located at the bottom of the navigation channel over a distance

of up to 50 km and a thickness on the order of 6 m. This layer was confined to the navigation channel, while turbidity exceeding 0.7 kg m^{-3} was not detected elsewhere on the deltaic platform. The upper layer of lower turbidity was separated from the fluid mud by a sharp discontinuity (lutocline), which caused strong reflections on the echograms, thus resulting in a so-called “double-bottom” pattern. Within the fluid mud layer there was a significant vertical gradient of turbidity, which in the deepest parts of the channel tended to reverse close to the bottom in the lowest 0.5 m of the water column.

2.4.7 Rhine-Meuse River

The Rhine-Meuse River estuary (or Rotterdam Waterway) in the Netherlands is a partially mixed estuary, through which the Rhine and the Meuse flow into the North Sea with an annual mean discharge of $1,500 \text{ m}^3 \text{ s}^{-1}$. It has a deepened navigation channel with a depth of 25 m. In field investigations of the movement of fluid mud, echo-sounders and a Partech turbidity meter with a range of $0\text{-}12 \text{ kg m}^{-3}$ were employed (Kirby and Parker, 1977). As described by van Leussen and van Velzen (1989), fluid mud layers with thicknesses of $0.5\text{-}4.0 \text{ m}$ and $\text{SSC} < 15 \text{ kg m}^{-3}$ usually appear in this area. A distinct lutocline was observed around high water slack. Fluid mud layers play a dominant role in sedimentation in this estuary. They are responsible for high deposition rates in short times under rough weather conditions. At times sediment deposition of about $2 \times 10^6 \text{ m}^3$ has been measured in one week (Wiersma, 1984).

2.4.8 Severn River

The Severn River estuary in the UK is dominated by semi-diurnal macro-tides with a spring range of 13 m and a neap range of 5 m. Extensive field studies in this estuary were carried out in the early 1970's (Kirby and Parker, 1982 and Kirby, 1986). In these studies, optical turbidity meters were used to obtain continuous horizontal and vertical traverses of SSC in comparatively low concentration ($0.1\text{-}20.0 \text{ kg m}^{-3}$) areas, and gamma-ray densimeters for high-resolution vertical profiles of dense stationary suspensions. The movement of fluid mud was simulated by Odd and Cooper (1989) using a horizontal, two-dimensional, numerical model. It was found that during spring tides the strong tidal currents, with a flood peak on the order of 2.3 m s^{-1} and associated turbulence, were sufficiently high that entrained sediment reached the water surface at peak ebb and peak flood, leading to "well-mixed", homogeneous vertical SSC profiles. As the velocity decreased towards slack water, sediment began to settle whilst the velocity was still high ($>1.5 \text{ m s}^{-1}$). A discontinuity in concentration (i.e., a lutocline) caused by settling formed in the water column, which then subsided towards the bed. By the time of slack water the layer settled to a level only 2 or 3 meters above the bed to leave a residual low concentration upper zone and a high concentration ($\sim >20.0 \text{ kg m}^{-3}$) lower layer. At slack water the layer stagnated for a short period before being re-entrained by the subsequent reversal of the tidal current.

2.4.9 South Alligator River

The South Alligator River estuary in the Northern Territory of Australia is a macro-tidal and shallow estuary with the mean water depth in the thalweg on the order of only a few

meters, a spring tidal range up to 6 m and maximum spring tidal currents of up to 2 m s^{-1} . The tidal currents exhibit a strong asymmetry with the flood currents being much stronger than ebb. The bed sediment is a mixture of sand and mud. The bulk of the suspended sediment is composed of particulates 1-4 μm in diameter. Vertical profiles of SSC were obtained using an Analite optical fiber nephelometer, which recorded data at 3 Hz when lowered at a speed of about $0.2\text{-}0.3 \text{ m s}^{-1}$ through the water column. A 210-KHz narrow-beam Deso-10 acoustic sounder was used to obtain a visual record of density stratification induced by suspended sediment (Wolanski, et al., 1988). The estuary is very turbid, with typical SSC values on order $1\text{-}6 \text{ kg m}^{-3}$. A maximum SSC of 10 kg m^{-3} was measured. For most of the ebb duration a lutocline separated a clear upper layer from an extremely turbid bottom layer; both layers being of comparable thickness, whereas the vertical gradients in SSC were small at flood tides (Wolanski, et al., 1988). A vertical, one-dimensional, numerical model of SSC was used by Wolanski, et al. (1988). Simulations of the tidal evolution of SSC were shown to be consistent with observations.

2.4.10 Thames River

The Thames River estuary in southern England is characterized by relatively uniform depths, about 7.6 m at mean tide level, and an exponential variation of the cross sectional area and channel width along its length. From its seaward limit to the tidal limit it is about 100 km long; the widths at these limits being 7000 m and 85 m, respectively. The mean tide range at the mouth is 4.3 m and increases up to 5.6 m at 63 km. With one major exception, the estuary has a hard bed made up of gravel, clay and chalk. In the area known as the Mud

Reaches, 45-53 km upstream of the mouth, there are extensive deposits of silt, and a turbidity maximum with SSC ranging between 0.1-5.5 kg m⁻³ (Owen and Odd, 1970). Field investigations (Inglis and Allen, 1957) and two-layer numerical modeling of Odd and Owen (1972) found that the null point is usually located in this area, and the turbidity maximum and sedimentation there are due mainly to silt transported in the lower layers from both the upstream and downstream directions. A local pocket of silt also occurs at about 24 km upstream of the mouth.

2.4.11 Yellow River

The Yellow River estuary in northern China discharges into the Bohai Sea with an annual mean inflow rate of about 1,550 m³ s⁻¹ and a sediment load of about 1.2×10⁹ tons yr⁻¹. It carries the largest sediment load of any river in the world and is dominated by loess silt and fine sand. On the order of 64% of the sediment is deposited on the river delta and mudflats, while the remaining is transported deeper into the Bohai Sea. As a result, a fan-shaped delta has been formed since 1855, which covers a distance of 160 km along shore and 20-28 km seaward (Wang, 1988). An extensive survey over the active delta front was carried out in September-October 1987 and July-August 1988, aimed at documenting the areal extent, vertical thickness, bulk densities, downslope velocities and velocity gradients of the sediment underflows and their relationship to tidal and storm forcing. It was reported that cross-isobath sediment dispersal into the shallow Bohai Sea is dominated by the formation of a hyperpycnal plume (SSC>2 kg m⁻³) and gravity-driven underflows (Wright, 1988). The strong tidal currents often had speeds of over 1.5 m s⁻¹

near the surface and 0.8 m s^{-1} at 1 m above the bed. The observed cross-isobath components of underflows had downslope speeds of $0.05\text{-}0.30 \text{ m s}^{-1}$. These underflows descended the rapidly prograding delta front as hyperpycnal plumes of 1-4 m thickness. SSC in the lower 2 m of the water column in the shallow parts ($<5 \text{ m}$) normally exceeded 1 kg m^{-3} and attained maxima of over 10 kg m^{-3} . SSC near the surface varied from $<0.1 \text{ kg m}^{-3}$ to $>1.0 \text{ kg m}^{-3}$. The highest turbidity values occurred landward of the front. In the deeper part ($\sim 10 \text{ m}$), SSC near the surface was consistently less than 0.1 kg m^{-3} and about 1 kg m^{-3} near the bottom. Observations during a storm and immediately after the storm revealed near-bottom layers of fluid mud with a thickness of 1-2 m and average SSC at $\sim 0.8 \text{ m}$ above the bed of about 252 kg m^{-3} . Another process observed at the top of the underflows was the activity of low frequency ($2.5\text{-}5.0 \times 10^{-3} \text{ Hz}$) internal waves of relatively high amplitude (1.0-2.5 m), which were believed having contribution to plume deceleration (Wright, et al., 1988).

CHAPTER 3 FLOW AND SEDIMENT TRANSPORT

3.1 Introduction

In order to examine lutocline dynamics in estuaries through numerical modeling, it is essential to carry out simulation for the following: (1) ambient flow field, (2) flow-sediment coupling due to the stratification effect and turbulence damping in the fluid mud layer, (3) erosion, entrainment, settling and deposition, (4) formation of fluid mud, (5) interfacial mixing, (6) suspended sediment advection and diffusion, (7) consolidation of bottom sediment, etc. Accordingly, a three-dimensional numerical model code is developed. This code consists of two parts, namely, a hydrodynamic model (called Coastal and Estuarine Hydrodynamic model - University of Florida or COHYD-UF) and a fine-grained sediment transport model (called Coastal and Estuarine Cohesive Sediment model - University of Florida or COSED-UF).

This chapter begins with descriptions of the governing equations of hydrodynamics and sediment transport, relevant boundary conditions, fine sediment transport processes, flow-sediment coupling and finite-difference schemes for solving these equations. Results of tests related to model validation are then presented.

3.2 Hydrodynamics

3.2.1 Governing Equations

In the derivations of the governing hydrodynamic equations, the following treatments are considered: (1) σ -transform is introduced (Figure 3.1) by transforming the temporal and Cartesian coordinate system (t, x, y, z) to a new system (t', x', y', σ) according to $\sigma = (z - \zeta)/H$ (Stansby and Lloyd, 1995), (2) the flow continuity equation takes the vertically integrated form, (3) the vertical distribution of pressure is assumed to be hydrostatic, and (4) higher order terms related to diffusion involving σ -coordinate are neglected. Thus, the continuity and momentum equations in the new time and coordinate system, where the superscript (prime) has been eliminated for convenience, respectively are (see Appendix A for derivations):

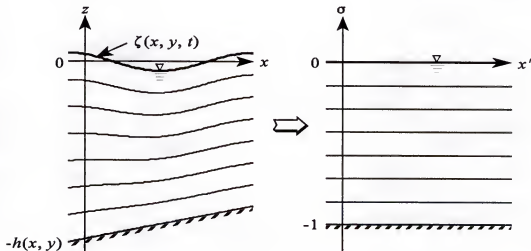


Figure 3.1. Schematic diagram showing σ -transform.

Continuity equation:

$$\frac{\partial \zeta}{\partial t} + \int_{-1}^0 \left(\frac{\partial Hu}{\partial x} + \frac{\partial Hv}{\partial y} \right) d\sigma = 0 \quad (3.1)$$

Momentum equation in the x-direction:

$$\begin{aligned} \frac{Du}{Dt} - fv = \frac{\partial u}{\partial t} + u \frac{\partial u}{\partial x} + v \frac{\partial u}{\partial y} + \omega \frac{\partial u}{\partial \sigma} - fv = -g \frac{\partial \zeta}{\partial x} - \frac{gH}{\rho} \int_{\sigma}^0 \frac{\partial \rho}{\partial x} d\sigma \\ - \frac{g}{\rho} \frac{\partial H}{\partial x} \left(\sigma \rho + \int_{\sigma}^0 \rho d\sigma \right) + \left(A_x \frac{\partial^2 u}{\partial x^2} + A_y \frac{\partial^2 u}{\partial y^2} \right) + \frac{1}{H} \frac{\partial}{\partial \sigma} \left(\frac{A_v}{H} \frac{\partial u}{\partial \sigma} \right) + \frac{1}{\rho H} \frac{\partial \tau_B}{\partial \sigma} \frac{u}{\sqrt{u^2 + v^2}} \end{aligned} \quad (3.2)$$

Momentum equation in the y-direction:

$$\begin{aligned} \frac{Dv}{Dt} + fu = \frac{\partial v}{\partial t} + u \frac{\partial v}{\partial x} + v \frac{\partial v}{\partial y} + \omega \frac{\partial v}{\partial \sigma} + fu = -g \frac{\partial \zeta}{\partial y} - \frac{gH}{\rho} \int_{\sigma}^0 \frac{\partial \rho}{\partial y} d\sigma \\ - \frac{g}{\rho} \frac{\partial H}{\partial y} \left(\sigma \rho + \int_{\sigma}^0 \rho d\sigma \right) + \left(A_x \frac{\partial^2 v}{\partial x^2} + A_y \frac{\partial^2 v}{\partial y^2} \right) + \frac{1}{H} \frac{\partial}{\partial \sigma} \left(\frac{A_v}{H} \frac{\partial v}{\partial \sigma} \right) + \frac{1}{\rho H} \frac{\partial \tau_B}{\partial \sigma} \frac{v}{\sqrt{u^2 + v^2}} \end{aligned} \quad (3.3)$$

where D/Dt denotes the total derivative with respect to time, u , v and ω are the flow velocity components in the x , y and σ directions, respectively, t is time, g is the gravitational acceleration, ζ is the instantaneous water surface elevation, H is the total water depth, $H = \zeta + h$, h is the undisturbed water depth, f is the Coriolis parameter, A_x and A_y are the

horizontal turbulent momentum diffusion coefficients in the x and y directions, respectively, A_v is the vertical turbulent momentum diffusion coefficient, ρ is the fluid density, and τ_b is the Bingham yield strength (Odd and Cooper, 1989). The vertical velocity in the σ coordinate, ω , is determined as according to

$$\omega = -\frac{1}{H} \int_{-1}^{\sigma} \left(\frac{\partial Hu}{\partial x} + \frac{\partial Hv}{\partial y} \right) d\sigma + \frac{(1+\sigma)}{H} \int_{-1}^0 \left(\frac{\partial Hu}{\partial x} + \frac{\partial Hv}{\partial y} \right) d\sigma \quad (3.4)$$

and the vertical velocity in the z coordinate, w , is obtained from (see Appendix A)

$$w = H\omega + u \left(\sigma \frac{\partial H}{\partial x} + \frac{\partial \zeta}{\partial x} \right) + v \left(\sigma \frac{\partial H}{\partial y} + \frac{\partial \zeta}{\partial y} \right) + \left(\sigma \frac{\partial H}{\partial t} + \frac{\partial \zeta}{\partial t} \right) \quad (3.5)$$

3.2.2 Boundary Conditions

The boundary conditions for solving the above equations are prescribed as follows:

1. Water surface: At the water surface ($\sigma=0$), the x and y components of the wind-induced stresses, τ_w^x and τ_w^y , are respectively specified as

$$\tau_w^x = \frac{\rho A_v}{H} \frac{\partial u}{\partial \sigma}, \quad \tau_w^y = \frac{\rho A_v}{H} \frac{\partial v}{\partial \sigma} \quad (3.6)$$

where the resultant vector, $\vec{\tau}_w$, is obtained from

$$\vec{\tau}_w = \rho_{air} C_w |\vec{W}| \vec{W}, \quad \text{with } C_w = 0.001(1 + 0.07|\vec{W}|) \quad (3.7)$$

Here ρ_{air} is the air density, C_w is the surface drag coefficient and \vec{W} is the wind velocity vector at a reference elevation (10 m above the water surface in the prototype case).

2. Bottom: The boundary condition at the bottom ($\sigma=1$) can be specified by either no-slip or a shear stress condition. At the bottom, the water particles are attached to (stationary) the solid surface, hence the velocity is zero, i.e., $\vec{u}_b=0$. Within the fluid, velocity increases rapidly and reaches a value of U_w (called slip velocity) over a small distance (Woodruff, 1973). Thus, there is a very steep velocity gradient near the bottom. If one were to specify the no-slip condition right at the bottom, a high-resolution numerical grid near the bottom would become essential. In turn this would lead to overly extensive computation time. In addition, viscous effects are important in the sublayer near the bottom, so that high Reynolds number turbulence modeling is not applicable there. Therefore, the shear stress condition is most commonly used. The bottom shear stress is expressed in terms of the velocity components taken from the modeled layer closest to the bottom. Accordingly, the corresponding stress components, τ_b^x and τ_b^y , can be related to the velocity gradient according to

$$\tau_b^x = \frac{\rho A_v}{H} \frac{\partial u}{\partial \sigma}, \quad \tau_b^y = \frac{\rho A_v}{H} \frac{\partial v}{\partial \sigma} \quad (3.8)$$

where the resultant vector, $\vec{\tau}_b$, is obtained from

$$\vec{\tau}_b = \rho C_D |\vec{v}_1| \vec{v}_1, \quad \text{with } C_D = \left[\frac{\kappa}{\ln(z_1/z_0) + \psi(z_1/L_\lambda)} \right]^2 \quad (3.9)$$

for turbulent flow. Here z_1 and \vec{v}_1 , respectively, are the elevation above the bottom and the velocity vector of the modeled layer closest to the bottom, C_D is the bottom drag coefficient,

κ is the von Kármán constant, z_0 is related to the effective roughness of the bed and ψ is a stratification function which takes the form (Monin and Obukhov, 1953):

$$\psi\left(\frac{z}{L_\lambda}\right) = 1 + \alpha_\lambda \frac{z}{L_\lambda} \quad (3.10)$$

In Eq. (3.10) α_λ is an empirical constant in the range of 4.7-5.5, and L_λ is the Monin-Obukhov length scale defined as

$$L_\lambda = \frac{u_*^3}{\kappa g w' \overline{\rho'} / \rho_0} = \frac{u_*^3}{\kappa^2 g z [(\rho_s - \rho) / \rho] \partial c / \partial z} \quad (3.11)$$

where u_* is the bottom friction velocity defined as $u_* = \sqrt{|\bar{\tau}_b| / \rho}$, c is the suspended sediment concentration (SSC), ρ_0 is the density of water, ρ_s is the sediment granular density, w' is the turbulent fluctuation of the vertical velocity in the z coordinate and ρ' is the turbulent fluctuation of density.

Since the shear stress condition is employed at the bottom boundary, the flow within low turbulence region close to the wall can only be described by a semi-empirical wall function which bridges the viscous sublayer by relating the values at the first numerical grid point placed outside the viscous sublayer to conditions at the wall. Launder and Spalding (1972) have proposed a wall function which is described by a logarithmic velocity profile applicable to the solid wall and the first grid point adjacent to it. The standard formulation of the wall function is

$$\frac{U_w}{u_*} = \frac{1}{\kappa} \ln(y^+ \epsilon) \quad (3.12)$$

where $y^+ = u_* z_1 / \nu$ is a dimensionless distance or frictional Reynolds number, ν is the kinematic viscosity and ϵ is a roughness parameter ($\epsilon=9$ for a hydraulically smooth wall and 0.05 for a hydraulically rough wall). As suggested by Rodi (1980), the wall function should apply to a point whose y^+ value is in the range of $30 < y^+ < 100$. Eq. (3.12) is then sufficiently accurate for most of the situations.

4. Shore Boundaries: At the shore boundaries, the following impermeable condition is prescribed:

$$\vec{V}_{n_s} = 0 \quad (3.13a)$$

where the subscript n_s denotes the direction normal to the solid boundaries.

Similar to the bottom, a no-slip condition at the shore boundary would require a high-resolution grid near boundary. Thus, the lateral shear stress condition is specified at the shore boundary according to

$$\rho A_n \frac{\partial V_t}{\partial x_n} = \rho C_t |V_t| V_t \quad (3.13b)$$

where A_n is the horizontal turbulent momentum diffusion coefficient in the direction normal to the solid boundary, x_n is the coordinate normal to the solid boundary, V_t is the tangential velocity at the modeled grid closest to the solid boundary, and C_t is the lateral friction coefficient.

5. Open Boundaries: At the open boundaries, the elevation of the water surface is prescribed:

$$\zeta_e = \zeta_0 + \sum_{n=1}^{N_t} H_n \cos(\omega_n t - g_n) \quad (3.14)$$

where ζ_0 is the mean water level, N_t is the total number of tidal harmonic components considered, ω_n is the angular frequency of the n^{th} harmonic component, and H_n and g_n are the amplitude and phase lag of the n^{th} harmonic component, respectively.

3.3 Sediment Transport

3.3.1 Sediment Conservation Equation in the Water Column

The sediment conservation equation in the x , y and σ coordinate system can be stated as (see Appendix A for derivation of the equation in the σ coordinate):

$$\begin{aligned} \frac{Dc}{Dt} - \frac{1}{H} \frac{\partial \omega_s c}{\partial \sigma} &= \frac{\partial c}{\partial t} + u \frac{\partial c}{\partial x} + v \frac{\partial c}{\partial y} + \omega \frac{\partial c}{\partial \sigma} - \frac{1}{H} \frac{\partial \omega_s c}{\partial \sigma} \\ &= \left(K_x \frac{\partial^2 c}{\partial x^2} + K_y \frac{\partial^2 c}{\partial y^2} \right) + \frac{1}{H} \frac{\partial}{\partial \sigma} \left(\frac{K_v}{H} \frac{\partial c}{\partial \sigma} \right) \end{aligned} \quad (3.15)$$

where ω_s is the sediment settling velocity, K_x and K_y are the horizontal turbulent mass diffusion coefficients in the x and y directions, respectively, and K_v is the vertical turbulent mass diffusion coefficient.

3.3.2 Boundary Conditions

The boundary conditions for solving Eq. (3.15) are prescribed as follows:

1. Water Surface: No sediment crosses the water surface ($\sigma=0$), i.e.,

$$\frac{1}{H} \frac{\partial \omega_s c}{\partial \sigma} + \frac{1}{H} \frac{1}{\partial \sigma} \left(\frac{K_v}{H} \frac{\partial c}{\partial \sigma} \right) = 0 \quad (3.16)$$

2. Bottom: Sediment vertical flux at the bed-fluid interface ($\sigma=-1$) is equal to the net flux due to erosion and deposition, i.e.,

$$\frac{1}{H} \frac{\partial \omega_s c}{\partial \sigma} + \frac{1}{H} \frac{1}{\partial \sigma} \left(\frac{K_v}{H} \frac{\partial c}{\partial \sigma} \right) = m_e - m_d \quad (3.17)$$

where m_e is the flux or rate of bottom sediment erosion (mass per unit area and time) and m_d is the flux or rate of SSC deposition.

3. Shore Boundaries: No sediment crosses the solid shore boundaries, i.e.,

$$\frac{\partial c}{\partial n_s} = 0 \quad (3.18)$$

4. Open Boundaries: The condition at the open boundaries are dependent on the flow, i.e., inflow or outflow. If fluid flows into the modeled region, the SSC of the water from the outside region is prescribed, i.e.,

$$c_e = c_i(x, y, \sigma, t) \quad (3.19)$$

where c_e is the prescribed SSC at the open boundary and c_i is the SSC from outside the modeled domain. In the case of outflow, the diffusion terms in Eq. (3.15) are neglected for numerical purposes, so that the mass conservative condition becomes:

$$\frac{\partial c}{\partial t} + u \frac{\partial c}{\partial x} + v \frac{\partial c}{\partial y} + \omega \frac{\partial c}{\partial \sigma} - \frac{1}{H} \frac{\partial \omega_s c}{\partial \sigma} = 0 \quad (3.20)$$

3.3.3 Fine Sediment Transport Processes

To use Eq. (3.15), the fine sediment transport processes must be expressed in terms of mathematical formulas. The major relevant processes are as follows.

1. Consolidation: In cohesive sediment transport models there is a need to take into account consolidation of newly deposited sediment, since the shear strength and, thus, the erosion resistance of the deposit increases with consolidation time (Verreert and Berlamont, 1989). The erodibility of a mud bed is determined by the strength of its particle-to-particle structure. This in turn is influenced by the state or degree of consolidation of the bed, which is time-dependent. Thus, in a consolidating bed the resistance to erosion is a time-dependent function of consolidation duration. Consequently, in a model of fine sediment transport behavior, predicting bed consolidation occupies a crucial role.

Consolidation of the deposit is caused by the self-weight of sediment particles, and is a process of expulsion of pore water from the bed (Parker and Lee, 1979). The settling cohesive sediment begins to behave as a soil and consolidate when the resulting stationary suspension develops particle-to-particle contacts and an effective stress appears (Hayter, 1983). At this stage, the total stress within the soil matrix is expressed as

$$\tau_t = \tau' + p_w \quad (3.21)$$

where τ_t is the total (normal) stress, τ' is the effective (normal) stress and p_w is the pore water pressure.

The aim of a consolidation model is to predict the vertical distribution of the time-dependent dry density or concentration, c , which in turn is related to the soil shear strength. There are two typical theoretical models describing the consolidation process, those based on force balance (Gibson, et al., 1967) and those based on solid mass conservation (Kynch, 1952). Here the theoretical framework first developed by Kynch (1952) is applied. It describes consolidation by a vertical transport equation. The consolidation rate, instead of permeability, is used as the model parameter, which is a function of dry density (Toorman and Berlamont, 1993). In the present work, the difference from the pure deposition model of Kynch (1952) is that the deposition flux minus erosion flux at the bed-fluid interface, i.e., $q = m_d - m_e$, is incorporated in the model, and a normalized coordinate σ' ($=z'/H'$) is used. Thus, the relevant transport equation is:

$$\frac{\partial H'c}{\partial t} = \frac{\partial \omega_{sc}c}{\partial \sigma'} + q \quad (3.22)$$

where z' is the vertical coordinate of the consolidating layer originating from the bottom and positive upward, H' is the thickness of the consolidating layer and ω_{sc} is the rate of consolidation. As for this rate, experimental evidence of Toorman and Berlamont (1993) suggests that two distinct modes of consolidation can be recognized from the plot of consolidation rate against concentration, i.e., loose soil consolidation and compacted soil consolidation. For these two modes, they developed a combined relationship expressed as

$$\omega_{sc} = \omega_{sc1} \exp\left(-\frac{c}{c_{s1}}\right) F_t + \omega_{sc2} \left(1 - \frac{c}{c_{s2}}\right)^{m_t} (1 - F_t), \quad F_t = \exp\left[-\left(\frac{c}{c_t}\right)^{n_t}\right] \quad (3.23)$$

where F_i is a characteristic mode transition (from loose soil to compacted soil) function with $n_i > 10$, m_i is a sediment-dependent constant, c_i is the transition concentration, ω_{sc1} and ω_{sc2} are the rates of consolidation for the first and the second modes, respectively, c_{s1} is the concentration corresponding to the maximum settling flux and c_{s2} is the saturation concentration, i.e., the maximum compaction concentration.

2. Fully Consolidated Bed: The deposited sediment is said to be fully consolidated when $c > c_{s2}$. The vertical profile of the dry density or concentration of a fully consolidated bed can be expressed as (Mehta, et al., 1982):

$$c = \bar{C} \alpha_2 \left(\frac{h_b - \Delta z}{h_b} \right)^{\beta_2} \quad (3.24)$$

where h_b is the bed thickness, \bar{C} is the bed average concentration, Δz is the incremental depth downward from the bed surface, and α_2 and β_2 are bed-dependent coefficients.

3. Shear Strength: The bed shear strength with respect to erosion is the primary measure of bed scour. As stated above, the shear strength increases with the consolidation time, or the dry density. Hence, usually, the shear strength is related to the bottom sediment concentration. In accordance with the description of Mehta (1991b), the bed shear strength, τ_s , can be considered to have the form

$$\tau_s = \tau_{s0} + \alpha_1 (\phi - \phi_c)^{\beta_1} \quad (3.25)$$

where τ_{s0} is the shear strength of newly deposited bottom sediment, α_1 and β_1 are sediment-dependent coefficients, ϕ is the solids weight fraction, $\phi = c/\rho_s$, and ϕ_c is the critical solids weight fraction below which mud has a fluid-like consistency. James, et al. (1988) show that ϕ_c is typically on the order of 0.03 to 0.05.

4. Interfacial Entrainment: Since diffusion-induced mixing over the lutocline is damped due to strong stratification and turbulence damping within fluid mud, internal wave breaking becomes a major mechanism contributing to vertical entrainment over the lutocline (Scarlatos and Mehta, 1993). There are two primary modes of instability of the interface depending on the relative thicknesses and positions of the current shear layer of thickness δ_v (Figure 2.1) and the density interfacial layer of thickness δ_i (Mehta and Srinivas, 1993). In case the mid-axes of density and velocity gradients coincide and δ_i is approximately equal to δ_v , the primary mode of instability is of the Kelvin-Helmholtz type, and is characterized by a roll-up and pairing of the interfacial vortices (Delisi and Corcos, 1973). When δ_i is smaller than δ_v due to stratification, Holmboe type of instability results, as recognized by sharp-crested interfacial cusps which protrude alternatively into both fluids (Browand and Wang, 1972). Results from laboratory and field observations further show that turbulence damping in the fluid mud layer introduces an upward-asymmetric mixing over the lutocline, i.e., there is a net upward flux of mass over the lutocline (Wolanski, et al., 1989; 1992; Mehta and Srinivas, 1993; Kranenburg and Winterwerp, 1997; Winterwerp and Kranenburg, 1997; Jiang and Wolanski, 1998).

Mehta and Srinivas (1993) established a semi-empirical formula for the rate of interfacial entrainment, m_{en} , which accounts for the cumulative effects of settling, cohesion and viscosity difference (between fluid mud and water) on mud entrainment

$$m_{en} = A_E Ri_0^{-1} - D_E Ri_0, \quad \text{with } Ri_0 = -\frac{g C_m (C_2 - C_1) h_{mix}}{\rho_0 (U_2 - U_1)^2} \quad (3.26)$$

where m_{en} is defined as dh_m/dt , h_m is the fluid mud layer thickness, A_E and D_E are sediment-dependent constants, Ri_0 is the global Richardson number, C_1 is the depth-mean sediment concentration in the upper, mixed, layer of height h_{mix} , C_2 is the corresponding value for the lower layer (being entrained), U_1 and U_2 are the respective depth-mean flow velocities, and C_m is a coefficient dependent on the granular density as

$$C_m = \frac{\rho_s - \rho_0}{\rho_s} \quad (3.27)$$

5. Deposition: From flume experiments Krone (1962) concluded that the rate of deposition is equal to the product of the near-bed settling velocity, SSC and the probability that a settling floc becomes attached to the bed:

$$m_d = \omega_{sb} c_b \left(1 - \frac{\tau_b}{\tau_d} \right) \quad (3.28)$$

where ω_{sb} and c_b are the near-bed settling velocity and SSC, respectively, and τ_d is the critical shear stress for deposition.

6. Bottom Erosion: Erosion of cohesive sediment, which is dependent on the composition and structure of bottom material that characterizes bottom resistance, and on the nature of the eroding force, can occur in two typical ways in estuaries (Mehta, 1991b). The first mode is floc-by-floc surface erosion in which the floc at the bed-water interface, initially attached to their neighbors by inter-particle electro-chemical bonds, breaks up and is entrained as a result of hydrodynamic lift and drag. The second mode is referred to as mass erosion, wherein the bed fails at a deeply embedded plane such that all the material above that plane is rapidly brought into suspension.

Surface erosion under current-induced bottom stress has been studied extensively (Parchure and Mehta, 1985). This process was subsequently examined further by Lee and Mehta (1994) and Mehta and Parchure (1999). From these studies, the effects of shear strength and temperature on the erosion rate are incorporated as follows:

$$m_e = M_{max} \exp\{-\chi \tau_s^\lambda\} [\Theta \exp(\Delta - \Lambda/\Theta)] [\tau_b - \tau_s] \quad (3.29)$$

in which M_{max} is the maximum erosion rate constant at $\tau_b = 2\tau_s$, χ , λ , Δ and Λ are sediment-dependent coefficients and Θ is the absolute temperature.

7. Settling Velocity: As stated in Section 2.2.1, in water with the salinity $s > 0.1 - 0.5\%$, the settling velocity of cohesive sediment is strongly dependent on SSC and can be divided into three sub-ranges in terms of concentration. These sub-ranges include free settling, flocculation settling and hindered-settling (Figure 2.2). Hwang (1989) developed a combined relationship between the settling velocity and SSC for flocculation and hindered

settling regions. Here, a modified relationship of Hwang, which includes the effects of flocculation, salinity and temperature on settling velocity, is used:

$$\omega_s = \left\{ \frac{ac^\alpha}{(c^2 + b^2)^\beta} \right\} \left\{ \left(\frac{\rho_s / \rho(\theta, s, c) - 1}{1.65} \right) \frac{10^{-6}}{v(\theta, c)} \right\} F(\theta) \quad (3.30)$$

where a , b , α and β are sediment-dependent empirical coefficients, θ is the temperature, $v(\theta)$ is the temperature-dependent fluid kinematic viscosity, $\rho(\theta, s, c)$ is the temperature, salinity and SSC dependent fluid density, and $F(\theta)$ is a temperature function which reflects the effect of temperature on flocculation defined as ω_s / ω_{s0} , where ω_{s0} is the flocculation settling velocity at 15 °C. By reprocessing the experimental data of Lau (1994) at different temperatures (see Appendix C), an empirical relationship for $F(\theta)$ is obtained as (Figure 3.2):

$$F(\theta) = 1.776 - 0.0518\theta, \quad \text{for } \theta = 0 - 30^\circ\text{C} \quad (3.31)$$

3.4 Flow-Sediment Coupling

3.4.1 Baroclinic Effects

Sediment-induced stratification is considered in the hydrodynamic equations, i.e., the second and third terms on the right hand sides of Eqs. (3.2) and (3.3), where the bulk density (ρ) of water/sediment mixture are related to SSC ($=c$) by

$$\rho = \rho_0 + C_m c \quad (3.32)$$

3.4.2 Vertical Momentum and Mass Diffusion Coefficients

When the flow is stratified, the buoyancy effect tends to restore vertically moved fluid lumps back to their original positions, and thereby causes a reduction of the turbulent transfer of momentum and mass. From the theoretical relationship derived by Rossby and

Montgomery (1935), Munk and Anderson (1948) proposed following generalized semi-empirical formulas:

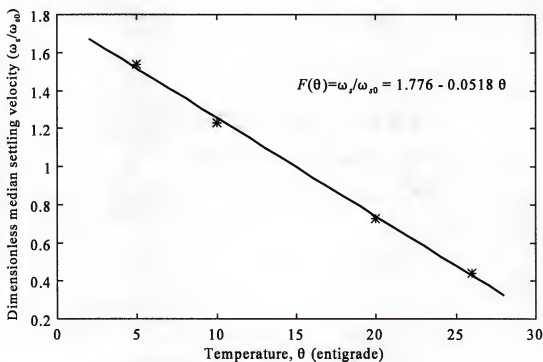


Figure 3.2. Dimensionless median settling velocity as a function of temperature, where ω_0 is the median settling velocity at 15 °C.

Momentum diffusion coefficient:

$$A_v = A_{v0} (a_1 + b_1 Ri)^{\gamma_1} \quad (3.33)$$

Mass diffusion coefficient:

$$K_v = K_{v0} (a_2 + b_2 Ri)^{\gamma_2} \quad (3.34)$$

where a_1 , b_1 , γ_1 , a_2 , b_2 and γ_2 are empirical constants, and A_{v0} and K_{v0} respectively are the vertical momentum and mass diffusion coefficients in homogenous flow. In terms of the

well-known mixing length concept of Prandtl (1925), A_{v0} and K_{v0} have simple forms for neutral turbulent diffusion:

Momentum diffusion coefficient:

$$A_{v0} = l_{m0}^2 \left| \frac{\partial u}{\partial z} \right| = \kappa u_* H(-\sigma)(1 + \sigma) \quad (3.35)$$

Mass diffusion coefficient:

$$K_{v0} = l_{c0} l_{m0} \left| \frac{\partial u}{\partial z} \right| = \kappa u_* H(-\sigma)(1 + \sigma) \quad (3.36)$$

Here $\sigma = (z - \zeta)/H$, l_{m0} and l_{c0} are, respectively, the momentum and mass mixing lengths in a homogeneous, non-cohesive flow, $l_{c0} \approx l_{m0}$, and Ri is the Richardson number defined as

$$Ri = -\frac{g}{\rho} \frac{\partial \rho / \partial z}{(\partial u / \partial z)^2 + (\partial v / \partial z)^2} \quad (3.37)$$

Jobson and Sayre (1970) noted that vertical mixing of suspended sediment in open channel flow occurs as a result of at least two semi-independent processes which are shown to be additive. These processes are: (1) Diffusion due to tangential components of turbulent velocity fluctuations, which is the predominant turbulent mixing process for fine sediment particles in general, and for all sediment particles in flows without strong vortex activity; and (2) diffusion due to centrifugal force arising from the curvature of fluid particle path lines, which is significant for coarse sediment in flows with strong vortex activity. They derived theoretically the following expressions for the total turbulent transfer coefficient of sediment:

$$K_{v0} = \alpha_s \kappa u_* H(-\sigma)(1+\sigma) + \beta_s u_* H\left(\frac{-\sigma}{0.9}\right)^3 \quad \text{for } \sigma \geq -0.9$$

$$K_{v0} = \alpha_s \kappa u_* H(-\sigma)(1+\sigma) + \beta_s u_* H\left(\frac{1+\sigma}{0.1}\right)^3 \quad \text{for } \sigma \leq -0.9$$
(3.38)

in which the first term represents turbulent transfer of sediment due to rectilinear velocity fluctuations, and the second term represents turbulent transfer of sediment due to curvature of fluid particle pathlines. Coefficients α_s and β_s are assumed to be functions of the particle characteristics. Using the method of average curve fitting technique, Jobson and Sayre (1970) reported that β_s was 0.98 and 0.49 and α_s was 0.038 and 0.1 for fine and coarse sediments, respectively.

A drawback of Eqs. (3.33) and (3.34) is that the turbulent diffusion coefficients will become zero if and where Richardson number tends to infinity, which is the case when the vertical gradient of velocity is zero. However, this is not realistic, since diffusion is practically never equal to zero. Hence, to overcome this disadvantage, an additional term interpreted a "background" value of the diffusion coefficient can be introduced in the formulas of Munk and Anderson (1948), i.e.,

Momentum diffusion coefficient:

$$A_v = A_{v0}(a_1 + b_1 Ri)^{Y_1} + A_{vb} \quad (3.39)$$

Mass diffusion coefficient:

$$K_v = K_{v0}(a_2 + b_2 Ri)^{Y_2} + K_{vb} \quad (3.40)$$

where A_{vb} and K_{vb} are the background values of the turbulent diffusion coefficients of momentum and mass, respectively. Representative values of a_1 , b_1 , γ_1 , a_2 , b_2 and γ_2 are given in Table 3.1.

Table 3.1. Parameters for momentum and mass diffusion coefficients in a stratified flow

a_1	b_1	γ_1	a_2	b_2	γ_2	Source
1	60-160	-0.5	--	--	--	Rossby and Montgomery (1935)
1	10	-0.5	1	3.33	-1.5	Munk and Anderson (1948)
1	10-15	-1	--	--	--	Kent and Pritchard (1959)

3.5 Solution Techniques

To solve hydrodynamic Eqs. (3.1), (3.2) and (3.3) and sediment transport Eq. (3.15), a semi-implicit finite difference method is applied, which discretizes the convective and diffusive terms by an Eulerian-Lagrangian scheme (Casulli and Cheng, 1992). This solution method has the advantage of a minimum degree of implicitness, good stability and consistency, and high computational efficiency at a low computational cost.

As shown in Figure 3.3, a spatial mesh consisting of rectangular cells, totally $M \times N \times L_f$ and each of length Δx and Δy and height $\Delta \sigma$, is introduced. Each cell is numbered at its center with indices i , j and k . The discrete u -velocity component is then defined at half-integer i and integers j and k . Similarly, the v -velocity component is defined at integers i and k and half-integer j . The vertical velocities, ω and w , are defined at integers i and j and half-

integer k . Water surface elevation ζ is defined at integers i and j . The undisturbed water depth $h(x,y)$ and the total water depth $H(x,y)$ are specified at the both u and v points. Finally, SSC, denoted by c , and fluid density ρ are defined at integers i, j and k .

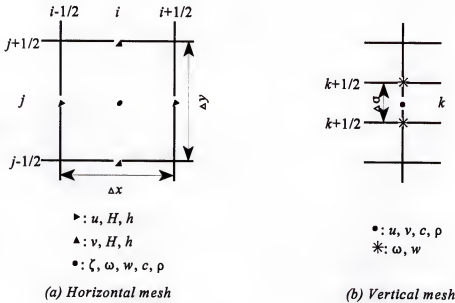


Figure 3.3. Schematic diagram of computational mesh and notation.

3.5.1 Discretization of Hydrodynamic Equations

The general, semi-implicit, discretization of the continuity Eq. (3.1) and momentum Eqs. (3.2) and (3.3) takes the following forms:

Differential continuity equation:

$$\begin{aligned} \frac{\zeta_{ij}^{n+1} - \zeta_{ij}^n}{\Delta t} = & -\frac{\Delta \sigma}{\Delta x} \left(H_{i+1/2,j}^n \sum_{k=1}^{L_j} u_{i+1/2,j,k}^{n+1} - H_{i-1/2,j}^n \sum_{k=1}^{L_j} u_{i-1/2,j,k}^{n+1} \right) \\ & -\frac{\Delta \sigma}{\Delta y} \left(H_{i,j+1/2}^n \sum_{k=1}^{L_j} u_{i,j+1/2,k}^{n+1} - H_{i,j-1/2}^n \sum_{k=1}^{L_j} u_{i,j-1/2,k}^{n+1} \right) \end{aligned} \quad (3.41)$$

Differential momentum equation in the x -direction:

$$\begin{aligned} \frac{u_{i+1/2,j,k}^{n+1} - u_p^n}{\Delta t} = & -g \frac{\zeta_{i+1,j}^{n+1} - \zeta_{ij}^{n+1}}{\Delta x} + B_{i+1/2,j,k}^n \\ & + \frac{(A v_{i+1/2,j,k+1/2}^{n+1} (u_{i+1/2,j,k+1}^{n+1} - u_{i+1/2,j,k}^{n+1}) - (A v_{i+1/2,j,k-1/2}^{n+1} (u_{i+1/2,j,k}^{n+1} - u_{i+1/2,j,k-1}^{n+1})))}{(H_{i+1/2,j}^n)^2 \Delta \sigma^2} \end{aligned} \quad (3.42)$$

Differential momentum equation in the y -direction:

$$\begin{aligned} \frac{v_{i,j+1/2,k}^{n+1} - v_p^n}{\Delta t} = & -g \frac{\zeta_{i+1,j}^{n+1} - \zeta_{ij}^{n+1}}{\Delta x} + B_{i,j+1/2,k}^n \\ & + \frac{(A v_{i,j+1/2,k+1/2}^{n+1} (v_{i,j+1/2,k+1}^{n+1} - v_{i,j+1/2,k}^{n+1}) - (A v_{i,j+1/2,k-1/2}^{n+1} (v_{i,j+1/2,k}^{n+1} - v_{i,j+1/2,k-1}^{n+1})))}{(H_{i,j+1/2}^n)^2 \Delta \sigma^2} \end{aligned} \quad (3.43)$$

Here the subscripts denote spatial positions, superscripts denote time steps, Δt , B is the sum of the Coriolis, baroclinic, horizontal diffusion and Bingham yield strength terms discretized by the hydrodynamic values at time step n , u_p^n and v_p^n are respective values of u and v at time step n , and subscript p denotes water particle position that is currently located at u or v point. To obtain position p , it is assumed that the velocity field (u , v) remains unchanged from the previous time step n to the present time step $n+1$.

Substituting Eqs. (3.42) and (3.43) into Eq. (3.41), a linear, five-diagonal system of equations for the water surface elevation, ζ , is obtained. This system is symmetric and strictly diagonally dominant with positive elements on the main diagonal and negative ones elsewhere. Thus it is positive-definite and has an unique solution. A substantial part of the computational time is utilized in solving this linear system (Casulli and Cheng, 1992). In practice, this system can be solved efficiently by the pre-conditioned conjugate gradient method (see Appendix B for details), which is fast and requires a minimum amount of computer memory (Bertolazzi, 1990). Then the velocity components, u and v are obtained from Eqs. (3.42) and (3.43).

3.5.2 Discretization of Sediment Transport Equation

Similar to the discretization of the hydrodynamic equations, the semi-implicit discretization of Eq. (3.15) is given by

$$\frac{c_{i,j,k}^{n+1} - c_p^n}{\Delta t} = \frac{(K_v)_{i,j,k+1/2}^n (c_{i,j,k+1}^{n+1} - c_{i,j,k}^{n+1}) - (K_v)_{i,j,k-1/2}^n (c_{i,j,k}^{n+1} - c_{i,j,k-1}^{n+1})}{(H_{i,j}^n)^2 \Delta \sigma^2} + D_{i,j,k}^n \quad (3.44)$$

where the notations are the same as in Eqs. (3.42) and (3.43), D is the sum of the discretized vertical settling and horizontal diffusion terms using the flow conditions and SSC at the previous time step n .

3.5.3 Discretization of Consolidation Equation

The consolidating bottom layer of thickness H' is divided into L_m sublayers, with each sublayer defined by a concentration c and thickness H'/L_m . At each time step Δt , the sediment transport model (COSED-UF) provides the net sedimentation (mass per unit area),

$q\Delta t$, at each grid point. Also, at each time step, $q\Delta t$ is introduced onto the consolidating layer in following way (Figure 3.4): (1) When net deposition takes place, i.e., $q > 0$, the initial concentration of the deposited sediment is prescribed as c_f (typically $c_f = 80 \text{ kg m}^{-3}$; Odd and Cooper, 1989), and the corresponding thickness $\Delta H' (= q\Delta t/c_f)$ is added to the top of the consolidating layer. Then the consolidating layer is redivided into L_m sublayers, and new initial concentrations at each computational element are obtained by cubic spline interpolation. (2) In the case of net erosion an erosion depth, $\Delta H'$, is subtracted from the top of the consolidating layer. Then, through redivision and cubic spline interpolation, new initial concentrations at each element are obtained as before. Following this procedure, the consolidation process is modeled using the discretized form of Eq. (3.22). To increase the modeling accuracy, a higher time resolution is applied, i.e., the consolidation time step $\Delta t' = \Delta t/N_c$, taking $N_c \geq 5$.

An explicit scheme is used for discretizing Eq. (3.22):

$$\frac{H'^{m+1}c_k^{m+1} - H'^m c_k^m}{\Delta t'} = \frac{c_k^m \omega_{sk}^m - c_{k-1}^m \omega_{sk-1}^m}{\Delta \sigma'} \quad (3.45)$$

Here the subscripts denote spatial positions, superscripts denote time steps and $\Delta \sigma'$ is the vertical step length. Then, at each time step the total thickness of the consolidating layer is calculated from mass conservation according to:

$$H'^{m+1} = \frac{\sum q\Delta t}{\int_0^1 c^{m+1} d\sigma'} \quad (3.46)$$

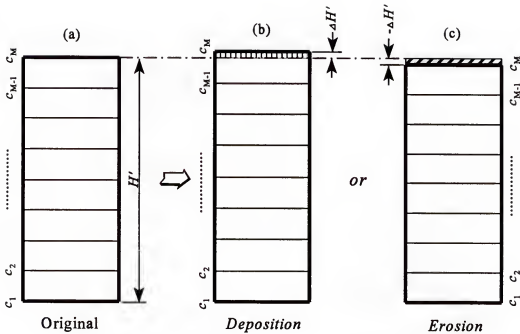


Figure 3.4. Schematization of the simulated consolidation process, where (a) is the original consolidating layer, (b) is the case of net deposition and (c) is the case of net erosion.

3.5.4 Properties of the Finite-Differential Equations

The accuracy, stability, numerical diffusion and spurious oscillations of the finite-differential equations (3.41), (3.42), (3.43) and (3.44) depend on the discretization scheme of the convective terms, when an Eulerian-Lagrangian approximation is adapted. Actually, as expressed in Eqs (3.2), (3.3) and (3.15), the convective terms can be rewritten more compactly as Lagrangian derivatives according to

$$\frac{DG}{Dt} = \frac{\partial G}{\partial t} + u \frac{\partial G}{\partial x} + v \frac{\partial G}{\partial y} + \omega \frac{\partial G}{\partial \sigma} \quad (3.47)$$

where G denotes any physical quantity, e.g., the velocity or SSC. Then the Eulerian-Lagrangian scheme discretizes the convective terms as

$$\frac{G_o^{n+1} - G_p^n}{\Delta t} \quad (3.48)$$

where subscript o denotes the current position of a water particle.

To obtain values of G_p^n , or u_p^n , v_p^n and c_p^n in Eqs. (3.42), (3.43) and (3.44), the Eulerian-Lagrangian scheme uses the back-tracing approach incorporated by a suitable interpolation method using three or more mesh points (Casulli and Cheng, 1992), in which, as stated before, it is assumed that the velocity field (u , v) remains unchanged from the previous time step n to present time step $n+1$. Here, these values are approximated by a bilinear interpolation over the eight surrounding mesh points (see Appendix B for details). The back-tracing time interval $\Delta t'' = \Delta t / N_p$, where N_p is the back-tracing step at each modeling time step, is usually selected to be ≥ 5 . In this event, the Eulerian-Lagrangian scheme becomes free of spurious oscillations. Moreover, numerical diffusion, which can be regarded as the interpolation error, is reduced when compared with numerical diffusion induced by the “up-wind” method. Further reduction in artificial diffusion can be obtained by decreasing the spatial steps Δx , Δy and $\Delta \sigma$ and increasing back-tracing step, N_p . Complete elimination of numerical diffusion can be achieved by using a higher-order interpolation formula, but the resulting method may introduce some spurious oscillations. Applications of this scheme to problems with large vertical diffusion, A_v or K_v , or small vertical spacings, $\Delta \sigma$, have

suggested the use of an implicit discretization only for the vertical diffusion terms. In fact, it can be shown that the stability condition for the above scheme is simply given by (Greenspan and Casulli, 1988)

$$\Delta t \leq \text{MIN} \left[A_x, A_y, K_x, K_y \left(\frac{1}{\Delta x^2} + \frac{1}{\Delta y^2} \right) \right]^{-1} \quad (3.49)$$

Evidently, when $A_x = A_y = K_x = K_y = 0$, this scheme becomes unconditionally stable. However, if one restricts the back-tracing process to within one cell, i.e., the back-traced water particle is not allowed to emerge out of the cell where it would start from the beginning, the stability condition becomes

$$\Delta t \leq \text{MIN} \left[\frac{2u_{\max}}{dx}, \frac{2v_{\max}}{dy}, A_x, A_y, K_x, K_y \left(\frac{1}{\Delta x^2} + \frac{1}{\Delta y^2} \right) \right]^{-1} \quad (3.50)$$

where u_{\max} and v_{\max} respectively are the maximum velocities in the x and y directions within the modeled domain.

3.6 Basic Simulations

3.6.1 Hydrodynamics

In this section, results of the COHYD-UF model will be compared with two analytical solutions. The first comparison will primarily investigate the model's capability to simulate the time propagation step. The second comparison will attempt to validate the model's ability to compute nonlinear effects.

1. Comparison with a Linear Analytical Solution: Consider tidal flow through an open channel connected to the sea at the mouth ($x=0$) and closed at the uphead end ($x=l$).

Neglecting the advective terms, bottom friction and wind surface stress, the one-dimensional hydrodynamic equations for flow through the channel are (Ippen 1966)

Momentum:

$$\frac{\partial U}{\partial t} + g \frac{\partial \zeta}{\partial x} = 0 \quad (3.51)$$

Continuity:

$$\frac{\partial \zeta}{\partial t} + h \frac{\partial U}{\partial x} = 0 \quad (3.52)$$

where U is the vertical mean velocity in the x direction and depth h is assumed to be constant. The selected boundary conditions associated with Eqs. (3.51) and (3.52) are:

At the uphead end of the basin:

$$U(l, t) = 0 \quad (3.53)$$

At the mouth of the basin:

$$\zeta(0, t) = A_0 \sin \omega_0 t \quad (3.54)$$

where A_0 and ω_0 , respectively, are the amplitude and angular frequency of the forcing tide at the open boundary. Selecting a uniform rectangular cross-section of the channel and only considering the first mode of oscillation, the solutions of Eqs. (3.51) and (3.52) are:

Water surface elevation:

$$\zeta(x, t) = \frac{A_0 \cos k(l-x)}{\cos kl} \sin \omega_0 t \quad (3.55)$$

Velocity:

$$U(x,t) = \frac{A_0 C_a \sin k(l-x)}{h \cos kl} \cos \omega_0 t \quad (3.56)$$

where C_a is the wave speed ($=\sqrt{gh}$) and k is the wave number ($=\omega_0/C_a$).

To test the hydrodynamic model results against the above solutions, a rectangular basin with a constant water depth of 20 m and basin length of 59 km is considered. Assume that a periodic tide with an amplitude of 1 m and a period of $T=12$ hr is forced at the mouth of the basin. The numerical solution is obtained by discretizing the basin into 30 grids with $\Delta x=2$ km and time step $\Delta t=20$ min.

Figure 3.5 shows the water surface elevation near the mouth ($x=10$ km), at the mid-point of the basin ($x=30$ km) and near the closed boundary ($x=58$ km). Likewise, Figure 3.6 presents the velocity near the mouth ($x=11$ km), at the middle point ($x=31$ km) and near the closed boundary ($x=51$ km). Both Figures 3.5 and 3.6 demonstrate that there is reasonably good agreement between theoretical and numerical solutions, even though a slight phase shift of velocity between the theoretical and numerical results occurs because terms higher than zero order are neglected in the analytical solution.

2. Comparison with a Non-linear Analytical Solution: When nonlinear terms are included in the one-dimensional shallow water equations, it is not possible to obtain an exact solution. However, one can use harmonic analysis to develop an analytical solution, which is still cumbersome because the high order terms are difficult to solve for. Accordingly, here only the zeroth and first order harmonic solutions are considered (Liu, 1988).

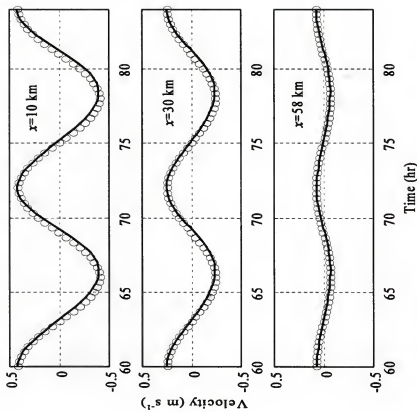


Figure 3.5. Modeling 1D linear hydrodynamic equation for tidal flow in an open channel. Lines are simulations and open circles represent analytical solutions.

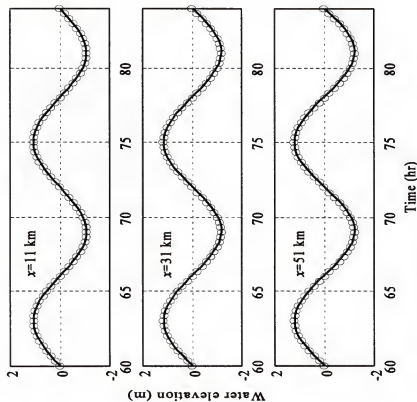


Figure 3.6. Modeling 1D linear hydrodynamic equation for tidal flow in an open channel. Lines are simulations and open circles represent analytical solutions.

Without the inclusion of Coriolis and bottom friction forces, the governing equations for one-dimensional nonlinear tidal motion can be written as

$$\frac{\partial U}{\partial t} + U \frac{\partial U}{\partial x} + g \frac{\partial \zeta}{\partial x} = 0 \quad (3.57)$$

Equation (3.52) remains unchanged. The boundary conditions and the geometry of the basin considered are the same as before. Neglecting solution terms higher than first order, the solutions are (Liu, 1988):

Water surface elevation:

$$\begin{aligned} \zeta(x,t) = & \frac{A_0 \cos k(l-x)}{\cos kl} \sin \omega t \\ & + \frac{A_0^2 k}{8h \cos^2 kl} \left[x \sin 2k(l-x) + \frac{l}{\cos 4kl} (\sin 2k(l+x) - \tan 2kl \cos 2k(l-x)) \right] \cos 2\omega t \end{aligned} \quad (3.58)$$

Velocity:

$$\begin{aligned} U(x,t) = & \frac{A_0 C_a \sin k(l-x)}{h \cos kl} \cos \omega t + \frac{A_0^2 \omega}{8h^2 \cos^2 kl} \\ & \left[x \cos 2k(l-x) + \frac{1}{2k} \sin 2k(l-x) - \frac{l}{\cos 4kl} (\cos 2k(l+x) - \tan 2kl \sin 2k(l-x)) \right] \sin 2\omega t \end{aligned} \quad (3.59)$$

The same forcing condition at the basin mouth as before is used to compare the solutions with model results. Figure 3.7 shows the comparison of water surface elevation, while Figure 3.8 presents the velocity. It can be seen that the model results are reasonably close to the analytical solutions. As before, the slight phase shift of velocity between the theoretical and numerical results occurs because terms higher than first order have been neglected in the analytical solution.

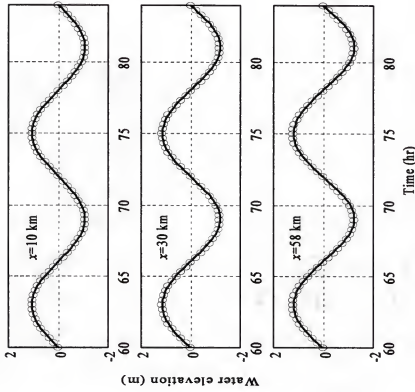


Figure 3.7. Modeling 1D non-linear hydrodynamic equation for tidal flow in an open channel. Lines are simulations and open circles represent analytical solutions.

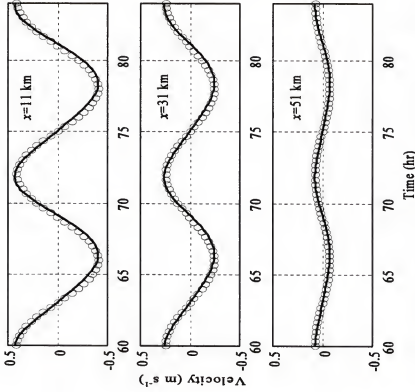


Figure 3.8. Modeling 1D non-linear hydrodynamic equation for tidal flow in an open channel. Lines are simulations and open circles represent analytical solutions.

3.6.2 Sediment Transport

To check the applicability of the COSED-UF numerical scheme, the following modeling tests against some special forms of the governing equations having exact solutions as well as field data in a river are carried out. Plots of numerical and analytical solutions are accordingly presented.

1. Steady State One-dimensional Convection-diffusion: The basic equation is

$$u \frac{dc}{dx} - K_x \frac{d^2c}{dx^2} - q_s = 0, \quad \text{at } 0 \leq x \leq l \quad (3.60)$$

where q_s is the constant source-sink term and l is the length of the system.

The boundary conditions are prescribed as

$$c(0) = c_0, \quad \left. \frac{dc}{dx} \right|_{x=l} = 0 \quad (3.61)$$

The analytical solution is

$$c(x) = c_0 + \frac{q_s K_x}{u^2} \left\{ e^{-N_{Pe} x} - e^{N_{Pe}(1-x/l)} \right\} + \frac{q_s x}{u} \quad (3.62)$$

where N_{Pe} is the Peclet number, ul/K_x , which is the ratio of convective transport to diffusive transport.

A rectangular grid with equal lengths of the spatial step was used in the numerical solution. Values of the parameters used were: $q_s=5$, $l=1$, $u=1$, $c_0=1$ and $K_0=1$. Figure 3.9 shows the comparison between the modeled results and the analytical solution.

2. Laplace Equation: The Laplace equation was solved for a rectangular domain, $0 \leq x \leq l_x$, $0 \leq y \leq l_y$, with a parabolic boundary condition for a quantity such as temperature, specified on $y=0$.

The basic equation is

$$K_x \frac{\partial^2 c}{\partial x^2} + K_y \frac{\partial^2 c}{\partial y^2} = 0 \quad (3.63)$$

The boundary conditions are given by

$$c(x,0) = \frac{K_0}{l_x^2} x(l_x - x), \quad c=0 \text{ on other faces} \quad (3.64)$$

By taking $K_x = K_y = K_0$, the exact solution takes the form

$$c(x,y,t) = \sum_{n=1}^{\infty} \frac{4K_0(1 - \cos n\pi)}{\sinh(n\pi l_y/l_x) n^3 \pi^3} \sin\left(\frac{n\pi x}{l_x}\right) \sinh\left[\frac{n\pi(l_y - y)}{l_x}\right] \quad (3.65)$$

The values $l_x=3$, $l_y=4$ and $K_0=40$ were used in the test problem. Figure 3.10 shows the comparison between the modeled results and the analytical solution.

3. One-dimensional Transient Heat Conduction: The basic equation is

$$\frac{\partial c}{\partial t} = K_x \frac{\partial^2 c}{\partial x^2}, \quad \text{at } 0 \leq x \leq l \quad (3.66)$$

The initial condition is

$$c=0, \quad 0 \leq x \leq l, \quad t=0 \quad (3.67)$$

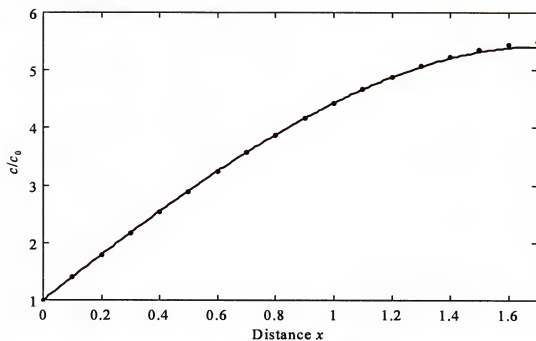


Figure 3.9. Modeling 1D convection-diffusion equation. Line is analytical solution and dots represent model simulations.

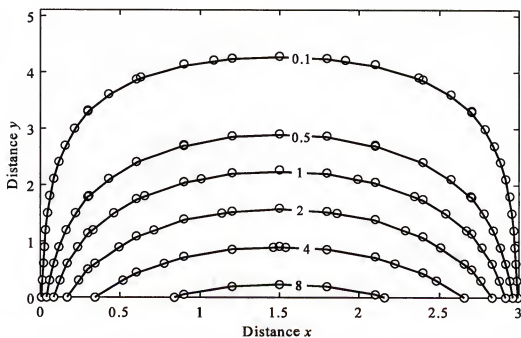


Figure 3.10. Modeling 2D Laplace equation. Lines are analytical solutions and open circles represent model simulations.

The boundary conditions are

$$c(l,t) = c_0, \quad \left. \frac{\partial c}{\partial x} \right|_{x=0} = 0 \quad (3.68)$$

The analytical solution is (Carslaw and Jaeger, 1959)

$$\frac{c}{c_0} = 1 - \frac{4}{\pi} \sum_{n=0}^{\infty} \frac{(-1)^n}{2n+1} e^{-(2n+1)^2 \pi^2 T_{El} / l^2} \cos \frac{(2n+1)\pi x}{2l} \quad (3.69)$$

where T_{El} is the elapsed time with $T_{El} = K_x t / l^2$. The values $c_0 = 1$, $l = 2$ and $K_x = 0.5$ were used in the test problem. Comparison between the modeled results and the analytical solution is shown in Figure 3.11.

4. Heat Conduction with Radiation: This problem was chosen to check the flux boundary condition formulation necessary in the model due to the resuspension term at the bed. The governing equation and initial condition are the same as Eqs. (3.66) and (3.67), respectively with the boundary conditions

$$c(l,t) = 0, \quad \left. \frac{\partial c}{\partial x} + \alpha_f c \right|_{x=0} = 0 \quad (3.70)$$

The exact solution is (Carslaw and Jaeger, 1959)

$$\frac{c}{c_0} = \left(\frac{1 + \alpha_f x}{1 + \alpha_f l} \right) - \sum_{n=1}^{\infty} \frac{2(\beta_n^2 + \alpha_f^2 l^2) \sin \left[\beta_n \left(1 - \frac{x}{l} \right) \right] e^{-\beta_n^2 T_{El}}}{\beta_n (\alpha_f l + \alpha_f^2 l^2 + \beta_n^2)} \quad (3.71)$$

where α_f is the linear heat transfer coefficient, h_f is the linear heat transfer coefficient, β_n is the positive roots of $\beta \cot \beta + \alpha_f l = 0$ and T_{El} is the elapsed time as defined before. The

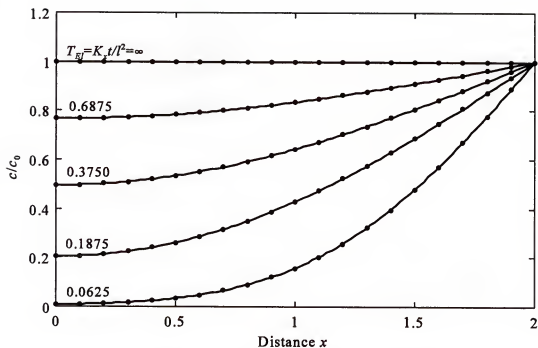


Figure 3.11. Modeling 1D transient heat conduction. Lines are analytical solutions and dots represent model simulations.

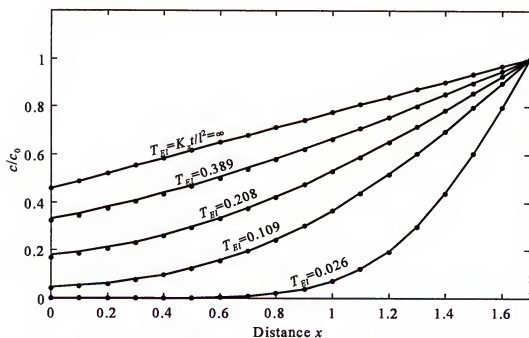


Figure 3.12. Modeling heat conduction with radiation. Lines are analytical solutions and dots represent model simulations.

values $\alpha_l=0.7$, $c_0=2$ and $l=1$ were used. Comparison between the modeled results and the analytical solution is shown in Figure 3.12.

5. Transient Convection-diffusion: The governing equation is

$$\frac{\partial c}{\partial t} + u \frac{\partial c}{\partial x} - K_x \frac{\partial^2 c}{\partial x^2} = 0, \quad \text{at } 0 \leq x < \infty \quad (3.72)$$

The boundary conditions are

$$c(0,t) = c_0, \quad c(\infty,t) = 0 \quad (3.73)$$

By taking the initial condition as $c(x,0)=0$, the analytical solution takes the form (Ogata and Banks, 1961)

$$\frac{c(x,t)}{c_0} = \exp\left(\frac{ux}{2K_x} - \frac{u^2 t}{4K_x}\right) \left\{ \int_0^t \operatorname{erfc}\left(\frac{x}{2\sqrt{K_x \xi}}\right) \frac{u^2}{4K_x} \exp\left[\frac{u^2(t-\xi)}{4K_x}\right] d\xi + \operatorname{erfc}\left(\frac{x}{2\sqrt{K_x t}}\right) \right\} \quad (3.74)$$

Here ξ is the integration variable and erfc is the complementary error function. The values $u=1$ and $K_x=0.5$ were used in the modeling test. Comparison between the modeled result and the analytical solution is shown in Figure 3.13.

6. Three-dimensional Laplace Equation: The three-dimensional equation was solved for a cubic domain, $0 \leq x \leq l_x$, $0 \leq y \leq l_y$, $0 \leq z \leq l_z$ with a power boundary condition for a quantity such as temperature, specified on $z=0$.

The governing equation is

$$K_x \frac{\partial^2 c}{\partial x^2} + K_y \frac{\partial^2 c}{\partial y^2} + K_z \frac{\partial^2 c}{\partial z^2} = 0 \quad (3.75)$$

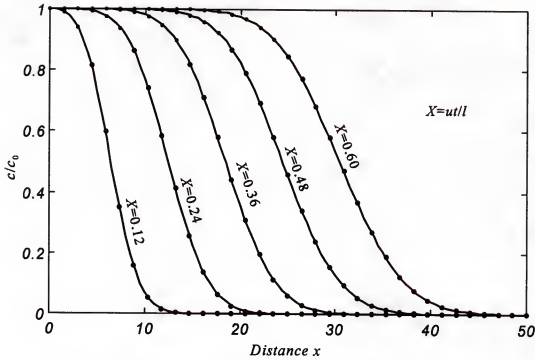


Figure 3.13. Modeling 1D transient convection-diffusion equation. Lines are analytical solutions and dots represent model simulations.

The boundary conditions are given by

$$c(x,y,0) = \frac{K_{xy}}{l_x^2 l_y^2} (l_x - x)(l_y - y), \quad c=0 \text{ on other faces} \quad (3.76)$$

By taking $K_x = K_y = K_v = K_0$, the exact solution has the form

$$c(x,y,z) = \sum_{m=1}^{\infty} \sum_{n=1}^{\infty} \frac{16K_0 (1 - (-1)^m) (1 - (-1)^n)}{m^3 n^3 \pi^6 \sinh \left[l_y \pi \sqrt{(m/l_x)^2 + (n/l_y)^2} \right]} \sin \frac{m\pi x}{l_x} \sin \frac{n\pi y}{l_y} \sinh \left[(l_y - z) \sqrt{\left(\frac{m\pi}{l_x} \right)^2 + \left(\frac{n\pi}{l_y} \right)^2} \right] \quad (3.77)$$

The values $l_x=16$, $l_y=26$, $l_z=14$ and $K_0=160$ were used in the modeling test.

Comparison between the modeled results and the analytical solution is shown in Figure 3.14.

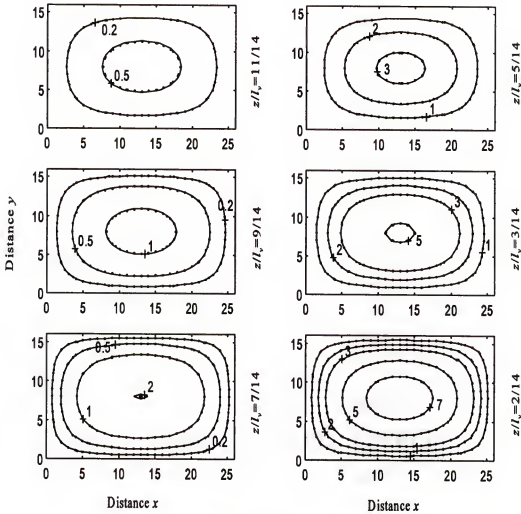


Figure 3.14. Modeling 3D Laplace equation. Lines are analytical solutions and dots represent model simulations.

7. Modeling Test Against Field Observations: To further test the sediment transport model, observed data of SSC and velocity profiles in the Savannah River estuary by

Ariathurai, et al. (1977) were used. Neglecting lateral variations of SSC and velocity due to the fact that it is a narrow estuary, the model is used in the vertical 2D code. In the modeled domain only three grid points -- located upstream, mid-point and downstream of the 6.7 km long estuarine segment considered -- were set. The velocity profiles measured at these three points were inputted for using in the sediment transport model. The SSC profiles measured at the two end sites of the segment were prescribed as boundary conditions and that at the middle site was used for verification. In the simulation, the following effects were included: longitudinal and vertical turbulent diffusion, longitudinal advection, sediment settling, suspended sediment deposition, and bottom erosion. The results are shown in Figure 3.15. It is seen that the simulated results compare approximately with observations. It is likely that the degree of comparison may improve provided: (1) modeling parameters are further fine-tuned, and (2) the full 3D code is used along with more accurate boundary conditions for SSC.

3.6.3 Consolidation

For testing the consolidation model two sets of experimental data on consolidation, without and with the net deposition flux at the bed-fluid interface (q), are considered as follows.

1. Consolidation without Deposition: Consolidation without deposition at the bed-fluid interface was examined by Toorman and Berlamont (1993) using an estuarine mud from Doel Dock in Belgium. In their experiments, which were conducted in a settling column described by Van den Bosch et al. (1988; 1989; 1990), both the consolidation rate and the density profiles of the consolidating layer were measured. The rate of consolidation

takes the form of Eq. (3.23), for which Toorman and Berlamont (1993) selected $\omega_{sc1}=5\times 10^{-4} \text{ m s}^{-1}$, $\omega_{sc2}=7\times 10^{-6} \text{ m s}^{-1}$, $c_{s1}=20 \text{ kg m}^{-3}$, $c_{s2}=205 \text{ kg m}^{-3}$, $c_t=160 \text{ kg m}^{-3}$, $m_t=3$ and $n_t=13$ (Figure 3.16), along with the initial concentration of deposited sediment $c_f=80 \text{ kg m}^{-3}$. The results are shown in Figure 3.17 for the vertical profiles of sediment concentration within the consolidating layer, and in Figure 3.18 for the time variation of surface elevation of the consolidating layer, where H_0 is the initial thickness of the layer. Both Figures 3.17 and 3.18 show that the modeled results compare favorably with the experimental data.

2. Consolidation with Deposition: Experiments on consolidation with deposition at the bed-fluid interface were carried out by Burt and Parker (1984). In their tests, fixed masses of an estuarine mud at a fixed concentration were added at 24 hour intervals to a settling column of 10 m height and 0.092 m diameter. A total of 7 beds were added; density profiles were measured 24 hours after each bed was added and immediately prior to the next addition. Density was also measured 15 days after the last bed was added. The material added for each layer comprised of 4 liters of suspension at 26.3 kg m^{-3} solids content giving a dryweight mass of 105.2 g solids.

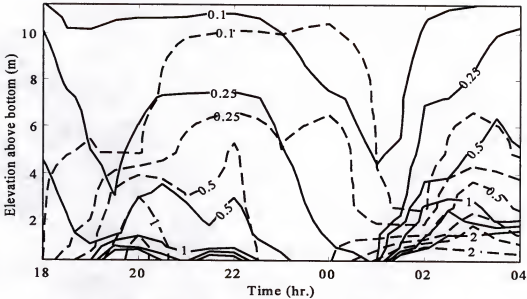


Figure 3.15. Modeling SSC (unit: kg m^{-3}). Solid lines are simulations and dashed lines represent field data observed from 1800, 9/24/68 to 0400, 9/25/68 in Savannah River estuary (after Ariathurai, et al., 1977). Contours from the surface to the bottom are 0.1, 0.25, 0.5, 1, 1.5 and 2, respectively.

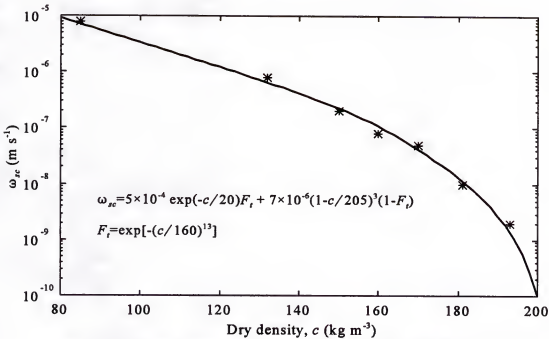


Figure 3.16. Consolidation rate, ω_{sc} , as a function of dry density for Doel Dock mud with $c_f=80 \text{ kg m}^{-3}$ (after Toorman and Berlamont, 1993).

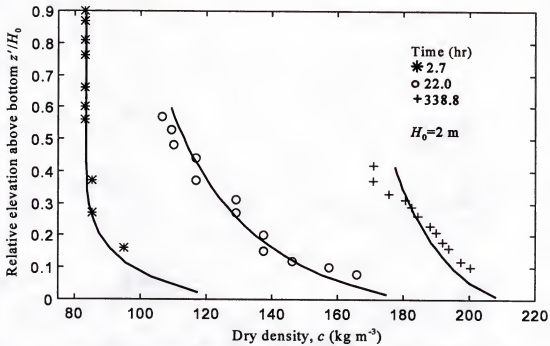


Figure 3.17. Modeling laboratory data of Toorman and Berlamont (1993) on consolidation. Lines are model simulations and points represent data.

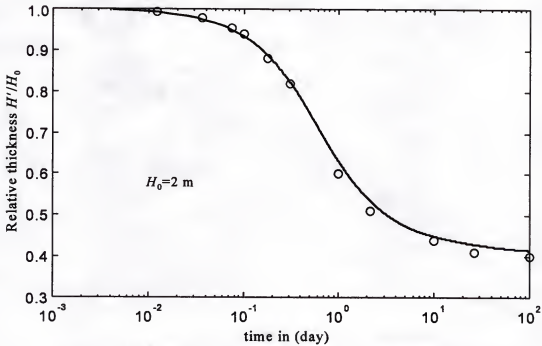


Figure 3.18. Modeled consolidation curve (solid line) compared with the laboratory data (open circles) of Toorman and Berlamont (1993).

Through calibration, the coefficients in Eq. (3.23) are taken as $\omega_{sc1} = 1 \times 10^{-5} \text{ m s}^{-1}$, $\omega_{sc2} = 4.2 \times 10^{-6} \text{ m s}^{-1}$, $c_{s1} = 15 \text{ kg m}^{-3}$, $c_{s2} = 680 \text{ kg m}^{-3}$, $c_i = 15 \text{ kg m}^{-3}$, $m_i = 6$ and $n_i = 15$ (Figure 3.19). c_f is taken as 26.3 kg m^{-3} . In the modeling test, the deposited materials were introduced into the consolidating layer in the same way as the experiments. The results of the vertical profiles of sediment concentration within the consolidating layer are shown in Figure 3.20. It is seen that the modeled results are in reasonably good agreement with the experimental data.

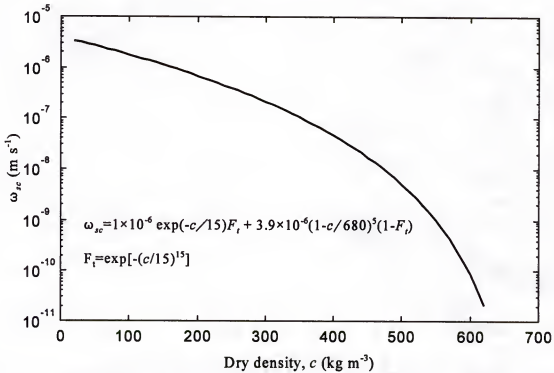


Figure 3.19. Consolidation rate, ω_{sc} , as a function of dry density for the laboratory tests of Burt and Parker (1984) with $c_f = 26.3 \text{ kg m}^{-3}$.

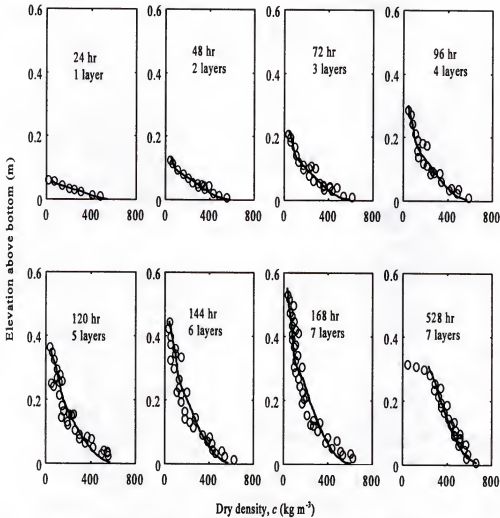


Figure 3.20. Modeling laboratory data of Burt and Parker (1984) on consolidation with deposition at the bed-fluid interface. Lines are model simulations and points represent data.

3.6.4 Interfacial Entrainment

Modeled sediment entrainment over the lutocline was tested against experimental data of Mehta and Srinivas (1993) using Eq. (3.26). In these experiments, values of $A_E=3\times 10^{-3}$ and $D_E=1.6\times 10^{-5}$ were reported. In their race-track flume experiments, the

initially introduced kaolinite mud layer, with a clear upper layer of water, was entrained as the upper layer velocity was increased gradually. In the modeling test, the measured velocity profiles were inputted. The same initial mud layer as in the experiment was also inputted. Then the mud layer was allowed to entrain with time using Eq. (3.26). The modeled and observed results of the vertical profiles of SSC at different times are shown in Figure 3.21. The modeled results are seen to be in reasonable agreement with the experimental data.

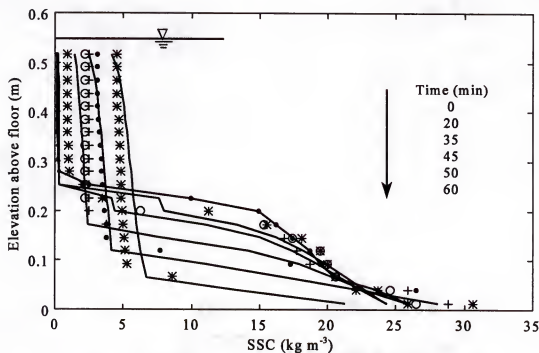


Figure 3.21. Modeling laboratory data on entrainment by Mehta and Srinivas (1993). Lines are model simulations and points represent data.

CHAPTER 4 FIELD INVESTIGATION AND DATA ANALYSIS

4.1 Study Area Description

Jiaojiang estuary is located on the east coast of China, about 200 km south of the Yangtze River (Figure 4.1). Jiaojiang is 200 km long and drains a basin of 6,500 km². The estuarine segment is only about 35 km in length. The mean water depth below mean sea level (MSL) in this segment is 4-7 m, and the mean width is about 1.2 km with a maximum of 1.8 km. Seaward of its mouth the width increases rapidly, forming Taizhou Bay in shallow coastal waters. The annual inflow rate is about $6.66 \times 10^9 \text{ m}^3$, with a mean discharge of $210 \text{ m}^3 \text{ s}^{-1}$. Semi-diurnal macro-tides prevail there. At the mouth the mean tidal range is about 4 m with a spring range of 6.3 m. The depth-mean peak tidal current can be up to 2.0 m s^{-1} . The tidal wave is strongly distorted in the estuary within a short distance from the mouth. Within the estuary itself, the duration of ebb exceeds flood by 1-2 hr. As a result the tidal currents exhibit a asymmetry; e.g., at Haimen the measured maximum flood and ebb currents are 2.1 and 1.8 m s^{-1} , respectively (Zhou, 1986; Dong, et al., 1997; Guan, et al., 1998).

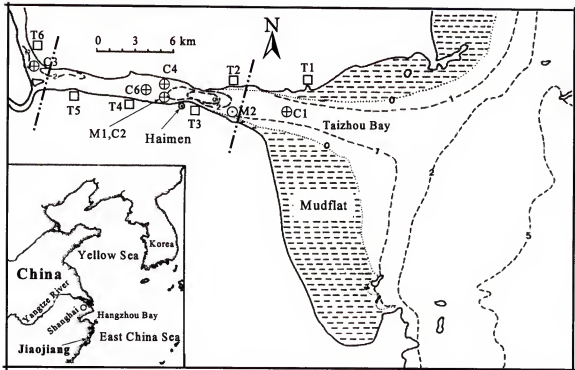


Figure 4.1. Location map of Jiaojiang estuary, China. Depths are in meters below lowest astronomical tide. M1 and M2 are mooring sites (Table 4.1); C1, C2, C3 and C4 are velocity measurement and SSC profile sampling stations (Table 4.1); C6 is the site of ASSM (Table 4.1) and T1-T6 are tide stations. The region between the double dotted lines is the modeled domain.

Jiaojiang is highly turbid with near-bottom SSC often exceeding 10 kg m^{-3} and depth-mean SSC greater than 5 kg m^{-3} (Li, et al., 1993; Dong, et al., 1997). Lutoclines along with fluid mud of 1-3 m thickness regularly appear except around flood slack. The river sediment is mostly in the clay and fine silt size range. The suspended sediment is dominated by clayey-silt with a dispersed mean particle size of $4\text{-}6 \mu\text{m}$. The fluvial sediment is estimated to be $1.23 \times 10^6 \text{ tons yr}^{-1}$, with a mean inflow SSC of 0.18 kg m^{-3} , i.e., about 4% the SSC in the estuary. Despite this high load, sediment discharge into Taizhou Bay is

only about 1% that of the Yangtze river (1.2×10^8 tons yr^{-1}) (Yu, 1987). The sedimentation rate in this estuary is up to 0.2 m yr^{-1} , requiring regular maintenance dredging for navigation from the sea to the port of Haimen (Li, et al., 1992). Haimen is located near the mouth of the estuary and is an economic center of this region. Thus, it is most important to maintain the depth of the navigation channel. For that reason, extensive engineering and scientific investigations have been carried out in this estuary. These studies have focused on tidal hydrodynamics, sediment transport and sedimentation by means of field investigations and horizontal and vertical 2D numerical modeling (e.g., Bi and Sun, 1984; Fu and Bi, 1989; Li, et al., 1993; Dong, et al., 1997; Guan, et al., 1998).

4.2 Experimental Plan, Methods and Instruments

In order to examine flow and sediment dynamics in the Jiaojiang estuary, three field campaigns were conducted. Table 4.1 provides the dates, measurements, locations, elevations at which measurements were made and apparatuses used. Sampling sites are shown in Figure 4.1. In terms of the objectives of these investigations, the observations can be classified into four types, namely: (1) fluid mud observations at sites M1 and M2, (2) lutocline observations at site C6, (3) vertical profiles of SSC, currents, temperature and salinity at sites C1, C2, C3 and C4, and (4) tidal elevations at sites T1-T6.

4.2.1 Fluid Mud Observations

Fluid mud related observations were carried out at site M1 during April 13-23, 1991, and at M2 during November 9-25, 1995. In both investigations, the monitoring system consisted of a 2.7 m high metal frame containing an Inter-Ocean (model S4) vector-averaging electromagnetic current meter and six self-logging optical fiber analite

Table 4.1. Summary of Jiaojiang field campaigns

Month Year	Date	Measure.	Site	Elevations	Apparatus	Range and sensitivity	Sampling interval
Apr. 1991	12-22	Current	M1	175 cm ASB ^a	S4 Inter-Ocean current meter	—	5 min
	13-23	Fluid mud	M1	Only elevations of 67, 55 and 35 cm ASB had data	Self-logging nephelometer	0-20 kg m ⁻³	5 min
	One day at each site	Velocity and SSC profiles	C1, C2 C3 & C4	Six elevations 0.0, 0.2, 0.4, 0.6, 0.8, 1.0H	SLC9-1 ^c ; CTD ^d , Turbidimeter and Nisk in bottle	0.03-80 kg m ⁻³	1 hr
Nov. 1994	Spring & neap at each site	Velocity & SSC profile	C1, C2 C3 & C4	Six layers 0.0, 0.2, 0.4, 0.6, 0.8, 1.0H	SLC9-1, CTD, Turbidimeter and Nisk in bottle	0.03-80 kg m ⁻³	1 hr
	Spring & neap at each site	S T D ^e & Turbidity	C2 & C3	Arbitrary elevations	CTD & Turbidimeter	0.03-80 kg m ⁻³	1 hr
	9-25	Fluid mud	M2	Six layers: 210, 178, 154, 109, 53, 17 cm ASB	Self-logging nephelometer	0-20 kg m ⁻³	10 min
Nov. 1995	9-25	Current	M2	1.5 m ASB Depth 6 m	S4 Inter-Ocean current meter	—	10 min
	15 6000-1600 hr	Lutocline	C6	Vertical resolution 5 cm	ASSM ^f Frequency 0.5MHz	—	0.6 sec
	Same	SSC for Calibration of ASSM signal	C6	Surface, middle & 1.0, 0.5, 0.2 m ASB	Multilayer Nisk in bottle	—	1 hr
	Same	S T D ^e & Turbidity	C6	Arbitrary elevations	CTD & Turbidimeter	0.03-80 kg m ⁻³	1 hr

Superscripts: a: Above sea bed; b: Fractions of instantaneous water depth, H; c: Digital current meter; d: Conductivity-Temperature-Depth sensor; e: Salinity, temperature and depth; f: Acoustic Suspended Sediment Monitor.

nephelometers. The nephelometers were fixed to the frame at six elevations near the bottom (Table 4.1). However, in the 1991 campaign, useful data were recorded at only three elevations. These transducers recorded data at intervals of 5 min in 1991 and 10 min in 1995. The data were bin-averaged over interval of 1 min with sampling at 1 s interval.

The Inter-Ocean current meter was mounted on the frame at 1.75 m in 1991 and 1.5 m in 1995, respectively, above the bottom. The meter logged velocity data sampled at 0.5 s interval and bin-averaged over 1 min. The logged interval was 5 min in 1991 and 10 min in 1995, so that the meter operated for only 1 min every 5 or 10 min. Practically calm water surface prevailed throughout the experiments with negligible waves.

4.2.2 Lutocline Observations

Lutocline observations were conducted at site C6 during 0600-1600 on November 15, 1995. A ship-borne Acoustic Suspended Sediment Monitor (ASSM) (made by the Shanghai Acoustics Laboratory, Academia Sinica) was used to detect the lutocline. The ASSM consisted of a 0.5 MHz acoustic transducer/receiver. The acoustic probe was deployed 1-2 m below the water surface. The entire system was under control of a PC for synchronization of sampling, preliminary data reduction and storage. The device had a pulse length of about 40 μ s, and measured the vertical profiles of sound scattered from suspended sediments in the range bins at 0.6 sec interval with a vertical resolution of 5 cm. The data were sampled at a rate of approximately 75 kHz for 9 min bursts. Each data burst consisted of 900 profiles of backscattered acoustic energy from suspended sediment particles between the bed and the acoustic probe.

4.2.3 Observations of SSC, Currents, Salinity and Temperature

Vertical profiles of SSC, tidal currents, temperature and salinity were obtained at sites C1, C2, C3 and C4 (Figure 4.1), respectively using Niskin bottles (each 60 cm long and 10 cm in diameter), SLC9-1 digital current meters (made by the Institute of Marine Instrument, Qingdao), CTD probes, turbidimeters and a 'mud probe' which consisted of a CTD transducer equipped with an Analite, infra-red, backscattering nephelometer (Wolanski, et al., 1988). This profiler was able to measure SSC from 0.03 to 80 kg m⁻³. The time series of such profiles were collected over 1 or 2 tidal cycles. Water samples were collected in the Niskin bottles at six elevations between the water surface to the bottom. Additionally, water samples were collected at 0.3, 0.6 and 1 m elevations above the bed using three horizontally deployed Niskin bottles mounted on a solid frame. These bottles were raised on board within about half a minute of sampling underwater, and water samples were then drawn immediately for analysis of SSC, salinity and sediment size (Li, et al., 1993; Dong et al., 1997).

4.2.4 Tidal Elevations

Tides were obtained at six sites from T1 to T6 (Figure 4.1) for a one-month period. Each time-series was processed by harmonic analysis (Dong, et al., 1997; Guan, et al., 1998).

4.3 Experimental Data

4.3.1 Sediment Size

The river sediment is mostly in the clay and fine silt size range. The suspended sediment is dominated by clayey-silt with a dispersed mean particle size of 4-6 µm (Figure 4.2). About 50% by volume of the particles constitute very fine silt (size range between 4-16

μm). The particle fraction with size less than $4\ \mu\text{m}$ accounts for about 40% of the material by volume (Li, et al., 1993; Li, et al., 1999).

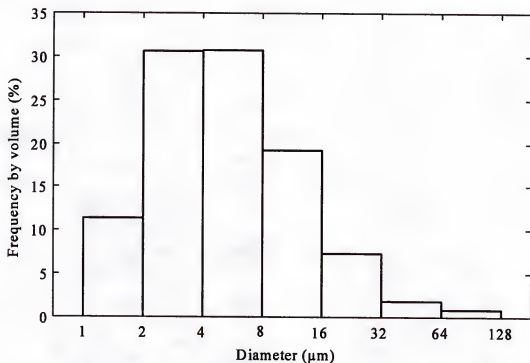


Figure 4.2. A representative frequency distribution of suspended sediment (dispersed) size in the Jiaojiang estuary.

4.3.2 Tides

1. Elevation: Harmonic analysis showed that the M_2 and S_2 constituents dominate this estuary. Figure 4.3 shows the time series of tidal elevations at sites T1 and T5 during a spring tide. It is seen that the tide was distorted as it propagated upstream from the mouth. For example, at T1 (outside the mouth), the flood lasted 5.78 hr and the ebb 6.64 hr. In

contrast, at T5 (inside the estuary) the flood was 5.29 hr and ebb was 7.13 hr. In other words, within a short distance of about 18 km from the mouth to upstream, the duration of flood decreased by about one-half hour.

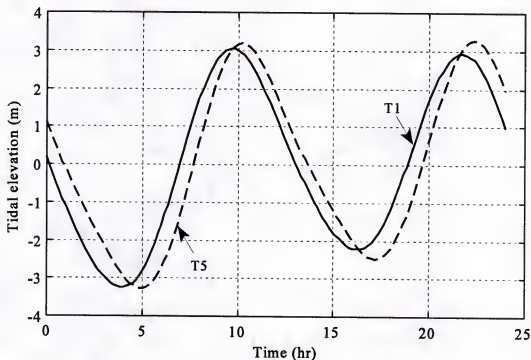


Figure 4.3. Time series of tidal elevation at sites T1 and T5 during a spring tide from 0000 hr on 11/05/94 to 0100 hr on 11/06/94.

2. Currents: As a result of tidal distortion, the tidal currents also exhibited an asymmetry as shown in Figures 4.4–4.6. It is seen that the flood current duration was shorter, and its strength was greater, than the corresponding ebb current values. Thus, for example, at C4 the ratio of depth-mean maximum flood current to ebb current was about 1.4 during the spring tide and about 1.25 during the neap tide.

4.3.3 Profiles of SSC

Figures 4.7 and 4.8 show typical time series of SSC profiles at C4 during a spring and a neap tide, respectively, and Figure 4.9 for C6 during a neap tide. It is seen that during low water slack and neap tide, the lutocline was distinct and well defined. In contrast, during spring tide and peak flows, the lutocline became indistinct even though the fluid mud layer (as defined in Section 2.1) became thicker. This observation supports the conclusion stated in later Section 5.2 regarding the relationship between the robustness of the lutocline and the flow conditions. Also at these sites, the vertical mean SSC was always greater than 5 kg m^{-3} and often exceeded 10 kg m^{-3} .

4.3.4 ASSM Data

Figures 4.10 (a) and (b) show two typical ASSM outputs, each over a 60 s time segment. Observe that most of the time the ASSM signal had a distinct step structure. As demonstrated in Figure 4.11, this step structure matches the real lutocline position detected by the turbidimeter. Hence it is reasonable to treat the step structure in the ASSM signal as the location of lutocline. Also observed are lutocline undulations, suggesting noteworthy internal wave generation and likely sediment entrainment activity. A smoother interface was observed during ebb [Figure 4.10(b)] than during flood [Figure 4.10(a)].

The SSC ($=c$) can be calculated from the ASSM reading, F_a , from (Thorne et al., 1994)

$$c = k_a F_a^2 (h' + h_a)^{\alpha_a} \exp(\beta_a h') \quad (4.1)$$

where h' is the depth below the acoustic probe and k_a , h_a , α_a and β_a are sediment-

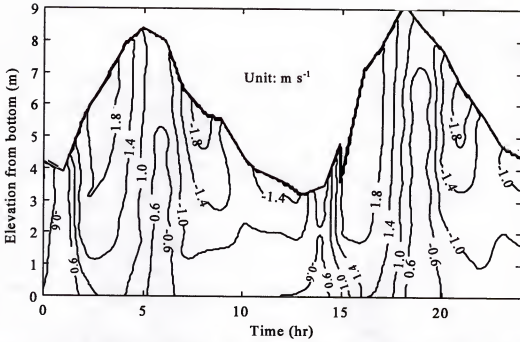


Figure 4.4. Time series of velocity at site C4 during a spring tide. Observations began at 1700 hr on November 5, 1994. Positive numbers signify flood and negative are for ebb.

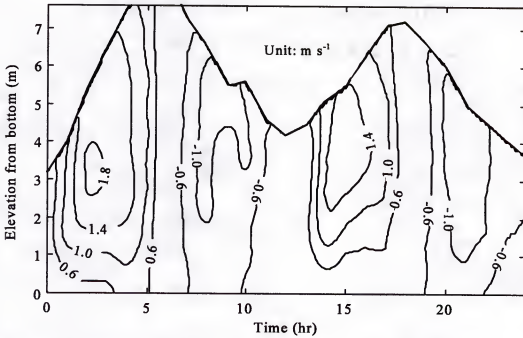


Figure 4.5. Time series of velocity at site C4 during a neap tide. Observations began at 0900 hr on November 10, 1994. Positive numbers signify flood and negative are for ebb.

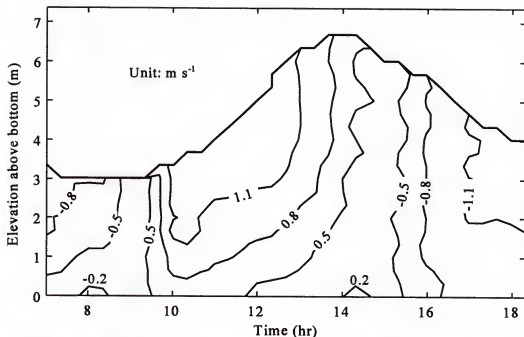


Figure 4.6. Time series of velocity at site C6 during a neap tide. Observations began at 0630 hr on November 15, 1995. Positive numbers signify flood and negative are for ebb.

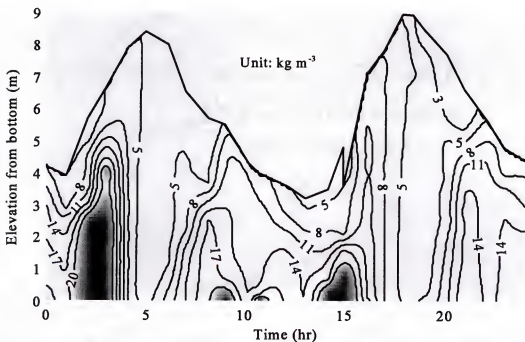


Figure 4.7. Time series of SSC at site C4 during a spring tide. Observations began at 1700 hr on November 5, 1994. Shaded area includes SSC greater than 20 kg m^{-3} .

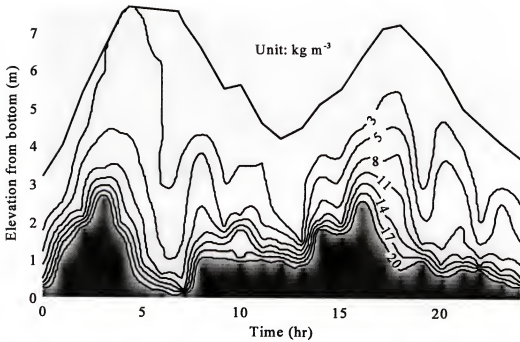


Figure 4.8. Time series of SSC at site C4 during a neap tide. Observations began at 0900 hr on November 10, 1994. Shaded area includes SSC greater than 20 kg m^{-3} .

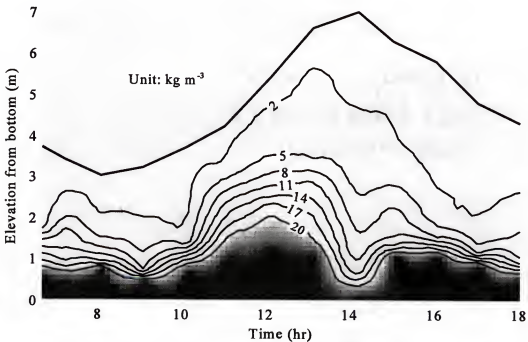
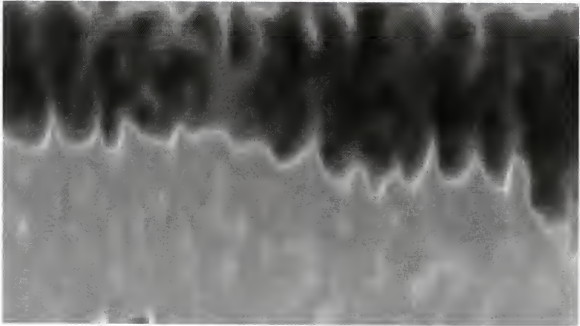
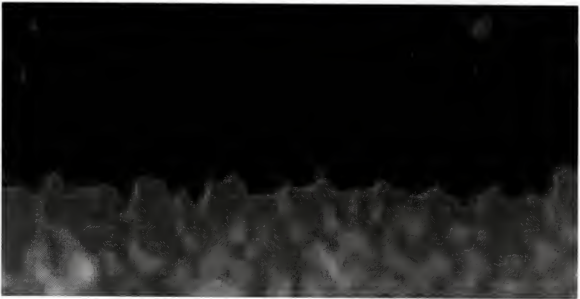


Figure 4.9. Time series of SSC at site C6 during a neap tide. Observations began at 0600 hr on November 15, 1995. Shaded area includes SSC greater than 20 kg m^{-3} .



(a)



(b)

Figure 4.10. Typical raw ASSM records during the neap tide on Nov. 15, 1995, with a horizontal time scale of 1 min and a vertical distance scale of 1.25 m. (a) was observed during a flood with a value of Richardson number Ri_0 of about 2, and (b) during an ebb with Ri_0 of about 150.

dependent constants. As mentioned above, the location of the largest vertical gradient of F_a can be taken as the lutocline elevation, $\zeta_a(t)$, above the bottom. From the time series of $\zeta_a(t)$, a spectral analysis of internal waves can be carried out, and related to local hydrodynamics.

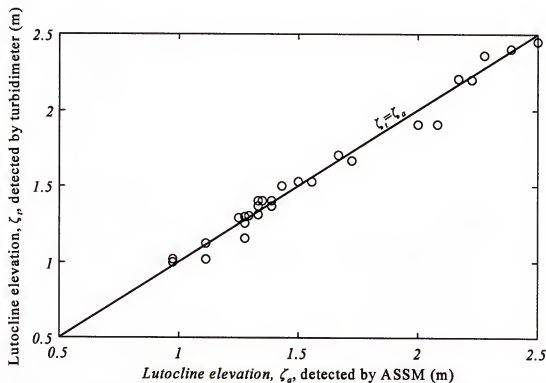


Figure 4.11. Relationship between lutocline elevations above bottom detected by the turbidimeter and by the ASSM. Data were collected during 0600-1600, Nov. 15, 1995.

Figure 4.12 shows three typical time-series, i.e., examples (a), (b) and (c), of lutocline elevation, $\zeta_a(t)$, traced from 9 min long ASSM records. It is evident that there are two types of internal waves riding on the lutocline, namely, low frequency internal waves with a period on the order of 1 min and high frequency internal waves with a period of about 5 s.

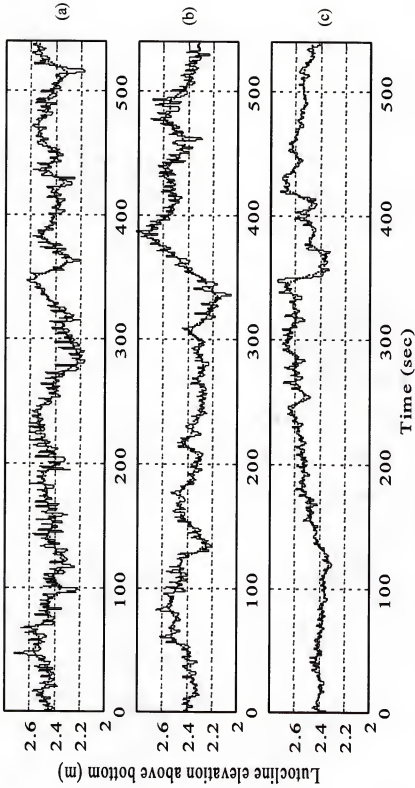


Figure 4.12. Time series of lutocline elevation at site C6 during a neap tide using ASSM on November 15, 1995. (a) and (b) were sampled during flood with a value of Ri_0 of about 1, and (c) during ebb with Ri_0 of about 150. Solid lines are instantaneous elevations and dashed lines are mean trends.

Two distinct types of internal waves on the lutocline have also been reported by other researchers. From the observation of internal waves on the lutocline in a race-track flume experiment, Mehta and Srinivas (1993) described two types of internal waves; One was characterized by high frequency and breaking. While the other included large-amplitude solitary waves which interspersed with the breaking waves and seemed to decay without breaking. Shi (1998) also observed two types of internal waves on the interface between the mobile and stationary fluid mud in Hangzhou Bay in China using an ASSM meter. These included low frequency waves with a period on the order of minutes and high frequency waves with a period of seconds. Wright, et al. (1988) observed low frequency ($\sim 6 \times 10^{-4}$ rad s⁻¹) and relatively large amplitude internal waves on the upper interface of the underflows over the active delta front of the Yellow River in China. They found that these internal waves had frequencies near the local Brunt-Väisälä frequency ($\sim 5.3 \times 10^{-4}$ rad s⁻¹).

For the purpose of spectral analysis of the high frequency internal waves, the lutocline elevation time-series processed for trend removal using an approach used by Costa (1989), i.e., filtering out the low frequency internal waves. The results after trend removal are shown in Figure 4.13. Figure 4.14 shows an enlarged portion of the time-series accentuating the internal waves. It is seen that the internal waves usually have sharp crests and flat troughs, which is most similar to the Holmboe-type interfacial instability (Broward and Wang 1972). In experiments of Srinivas (1989), in general both Kelvin-Helmoltz and Holmboe modes of interfacial instabilities appeared. However, here the Kelvin-Helmoltz instability is difficult to identify. Due to the interfacial instability, a net upward-asymmetric

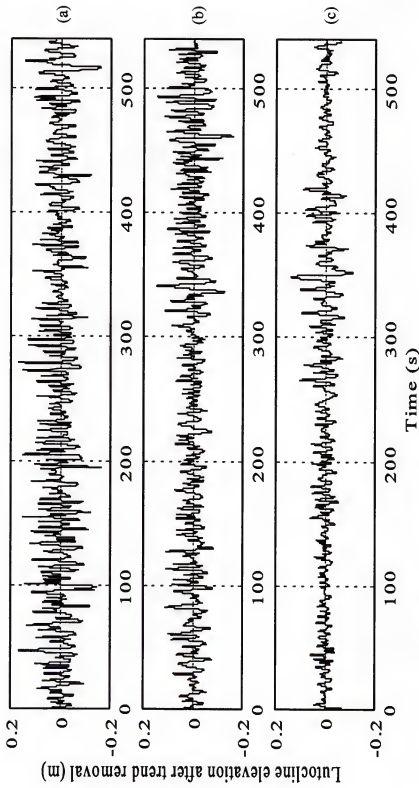


Figure 4.13. Times series of lutocline elevation after trend removal at site C6 during a neap tide, where (a), (b) and (c) correspond to Figure 4.12.

mass mixing can be expected in this case. Mixing can be further enhanced if the internal waves begin to break.

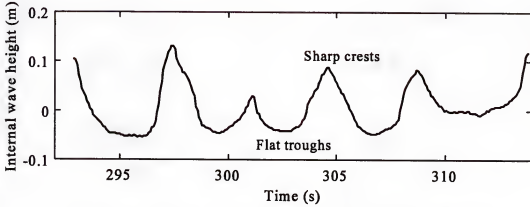


Figure 4.14. Typical profiles of internal waves exhibiting sharp crests and flat troughs. Data were taken from example (a) in Figure 4.13. Wave heights range from 0.07 m to 0.23 m.

Based on the Wiener-Khinchine theorem, the internal waves spectrum, $S(\omega')$, can be calculated using (Bendat and Piersol, 1971)

$$S(\omega_a) = \frac{2}{\pi} \int_0^{\infty} R(\tau) \cos(\omega_a \tau) d\tau \quad (4.2)$$

with the auto-correlation function, $R(\tau)$, defined as

$$R(\tau) = \lim_{T' \rightarrow \infty} \frac{1}{T'} \int_{-T'}^{T'} H_a(t) H_a(t+\tau) dt \quad (4.3)$$

where H_a is the internal wave profile, τ is the time interval or shifting time, T' is the integration time-limit and ω_a is the angular frequency (Ochi, 1990). The auto-correlation

functions for examples (a), (b) and (c) are shown in Figure 4.15. The resulting respective spectral densities are plotted in Figures 4.16-4.18. It is seen that the maximum spectral density is located around the modal frequency $\omega_a = 1.3 \text{ rad s}^{-1}$ during flood, with Ri_0 of about 1 (Figures 4.16 and 4.17), and around $\omega_a = 1.1 \text{ rad s}^{-1}$ during ebb, with Ri_0 of about 150 (Figure 4.18).

A further examination of internal waves was made by relating the root mean square (rms) of the height of the internal wave as well as its modal frequency (both for high and low frequency waves) to the global Richardson number and the tidal range. The rms of the high frequency wave height and the corresponding angular frequency were taken over 1 min segments of the ASSM output. One segment was selected from each 9 min ASSM burst (totally 21 bursts) for this purpose. The rms of the low frequency wave height and the corresponding angular frequency were taken over each 9 min segment of ASSM burst. The global Richardson number, Ri_0 , was calculated from Eq. (3.26) using the current velocity and SSC profiles. The lutocline was considered to be at the near bottom elevation having the maximum vertical gradient of SSC. The average value of Ri_0 over 1 min was taken for the high frequency waves and 9 min for the low frequency waves. The rms wave height, H_s , is calculated from

$$H_s = \sqrt{\frac{1}{N_a} \sum_{n=1}^{N_a} H_{an}^2} \quad (4.4)$$

where H_{an} is the n^{th} wave height and N_a is the total number of waves over the selected data

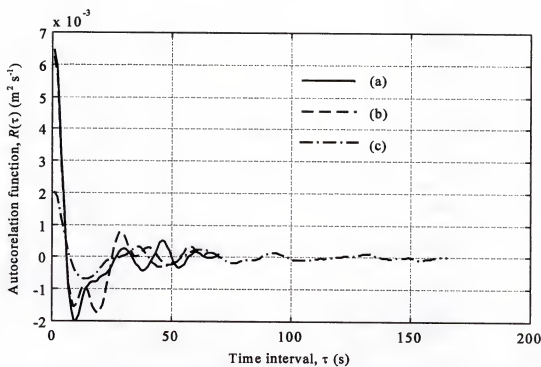


Figure 4.15. Auto-correlation function against time interval, where (a), (b) and (c) correspond to Figure 4.12.

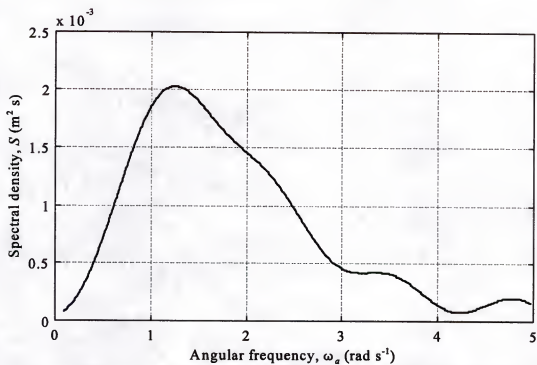


Figure 4.16. Internal wave spectrum corresponding to example (a) in Figure 4.13.

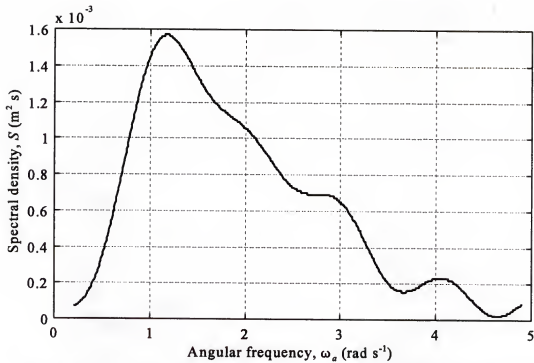


Figure 4.17. Internal wave spectrum corresponding to example (b) in Figure 4.13.

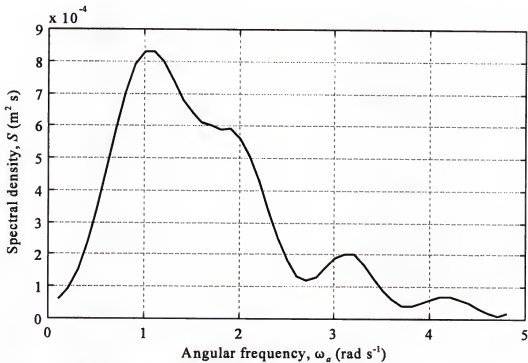


Figure 4.18. Internal wave spectrum corresponding to example (c) in Figure 4.13.

segment, i.e., 1 min or 9 min. The modal frequency is calculated as

$$\omega_a = \frac{2\pi N_a}{T_a} \quad (4.5)$$

where T_a is the duration of each segment.

The processed results are shown in Figures 4.19-4.26 and summarized in Table 4.2. It is seen that H_s and ω_a , both for high and low frequencies, have reasonably good relationships with the global Richardson number. In general, the lower the global Richardson number, the higher the H_s and ω_a values. This behavior is examined in Section 4.4.

There appears to be no identifiable relationships between H_s , ω_a and the tidal range. However, the Richardson number was typically much higher during ebb than during flood, because the ebb exhibited comparatively more uniform velocity profiles (Figure 4.6). As observed in Figures 4.21, 4.22, 4.25 and 4.26, internal waves had lower heights and angular frequencies during ebb than during flood. During ebb the majority of the data points are located below the mean trend-line. In contrast, the majority of the points are located above this line during flood.

Following Wright, et al. (1988), a possible relationship between the internal wave frequency and the Brunt-Väisälä frequency is examined here. The Brunt-Väisälä frequency, ω_v , is defined as

$$\omega_v = \sqrt{\frac{g}{\rho} \frac{\partial \rho}{\partial z}} \quad (4.6)$$

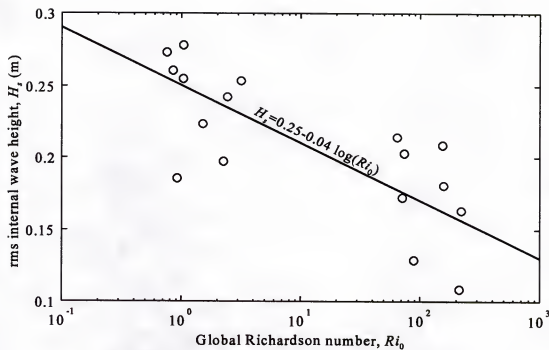


Figure 4.19. rms of high-frequency internal wave height as a function of global Richardson number.

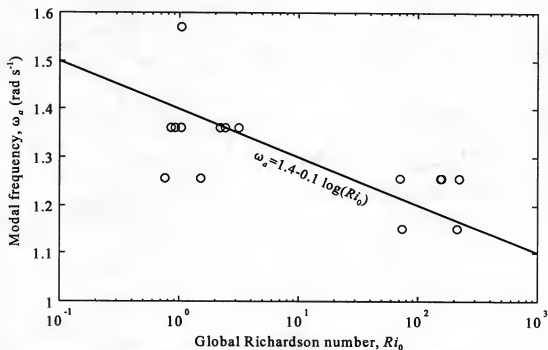


Figure 4.20. Modal frequency of high-frequency internal waves as a function of global Richardson number.

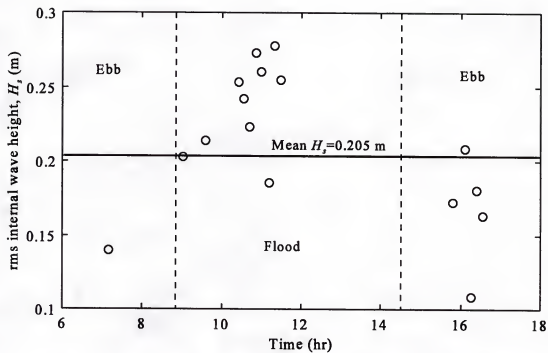


Figure 4.21. rms of high-frequency internal wave height during ebb and flood.

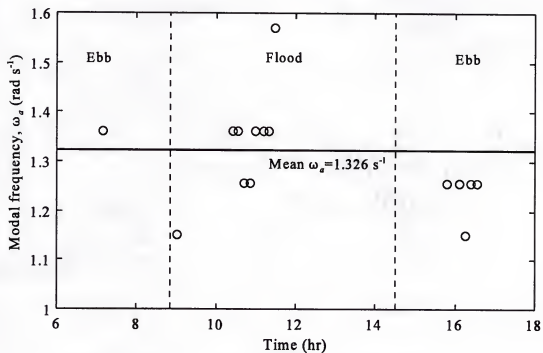


Figure 4.22. Modal frequency of high-frequency internal waves during ebb and flood.

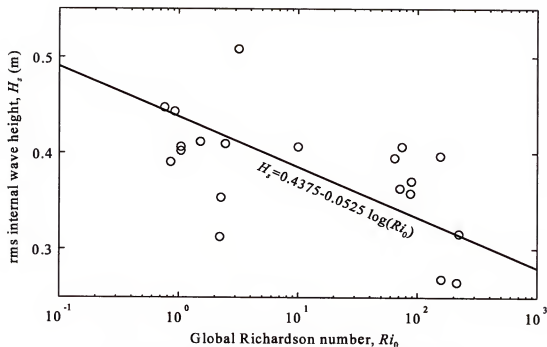


Figure 4.23. rms of low-frequency internal wave height as a function of global Richardson number.

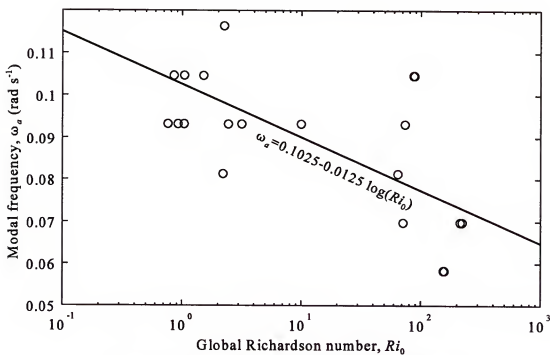


Figure 4.24. Modal frequency of low-frequency internal waves as a function of global Richardson number.

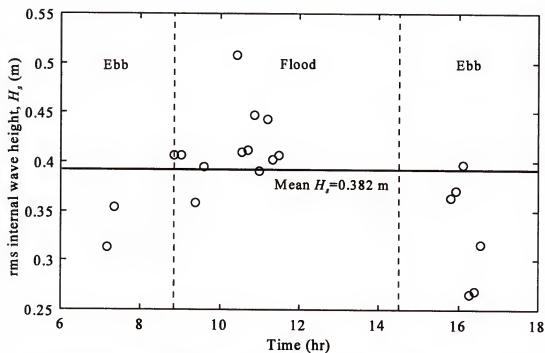


Figure 4.25. rsm of low-frequency internal wave height during ebb and flood.

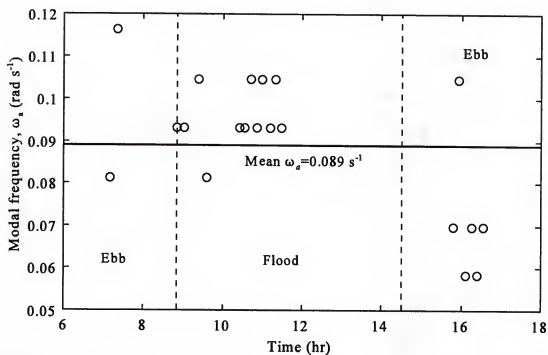


Figure 4.26. Modal frequency of low-frequency internal waves during ebb and flood.

Table 4.2. rsm height and angular frequency of internal waves as functions of global Richardson number and tidal range.

Type of internal wave	Parameter	Relationships	
		H_s (m)	ω_a (rad s ⁻¹)
High frequency	Ri_0	$H_s = 0.25 - 0.04 \log(Ri_0)$	$\omega_a = 1.4 - 0.1 \log(Ri_0)$
	Tidal range	Flood: 9 out of 10 points are above the mean value of $H_s = 0.205$ m Ebb: 5 out of 6 points are below the mean value of $H_s = 0.205$ m	Flood: 6 out of 9 points are above the mean value of $\omega_a = 1.326$ rad s ⁻¹ Ebb: 5 out of 6 points are below the mean value of $\omega_a = 1.326$ rad s ⁻¹
Low frequency	Ri_0	$H_s = 0.4375 - 0.0525 \log(Ri_0)$	$\omega_a = 0.1025 - 0.0125 \log(Ri_0)$
	Tidal range	Flood: 11 out of 12 points are above the mean value of $H_s = 0.382$ m Ebb: 7 out of 8 points are below the mean value of $H_s = 0.382$ m	Flood: 11 out of 12 points are above the mean value of $\omega_a = 0.089$ rad s ⁻¹ Ebb: 6 out of 8 points are below the mean value of $\omega_a = 0.089$ rad s ⁻¹

Similar to the global Richardson number formula (3.26), one can approximate ω_v as

$$\omega_v = \sqrt{\frac{g C_m (C_2 - C_1)}{\rho_0 h_{mix}}} = \sqrt{\frac{g'}{h_{mix}}} \quad (4.7)$$

where g' is the reduced gravity. To estimate ω_v using Eq. (4.7), the SSC profiles (Figure 4.9) observed at the same time as the ASSM data were employed. The results indicate that ω_v has a range of 0.12-0.26 rad s⁻¹. As shown in Figures 4.24, 4.26 and Table 4.2, the low frequency waves had frequencies ranging from 0.06 to 0.12 rad s⁻¹ and a mean value of

about 0.09 rad s^{-1} . Thus, the low frequency waves had modal frequencies near the local Brunt-Väisälä frequency. This type of internal wave at haloclines or thermoclines has been extensively studied by previous researchers (e.g., Lamb, 1945; Neumann and Pierson, 1966; Phillips, 1977). Theoretically, in a stratified fluid a vertically-moved fluid particle due to any disturbance will be restored to its original level under buoyancy force and overshift inertially. Consequently, it will oscillate about the original level at the Brunt-Väisälä frequency. Thus, it is believed that the low frequency wave detected in the Jiaojiang exhibited a natural oscillation about the lutocline.

4.3.5 Floc Settling Velocity

In order to examine the characteristic dependence of the settling velocity as a function of SSC in this estuary, the SSC profile data shown in Figures 4.7-4.9 were used. One may conveniently select the SSC profiles during slack water for this purpose, since the quiescent water assumption is approximately satisfied then. From the sediment conservation Eq. (3.15), the simplified vertical equation for SSC transport is

$$\frac{\partial c}{\partial t} - \frac{1}{H} \frac{\partial \omega_s c}{\partial \sigma} = 0 \quad (4.8)$$

For solving Eq. (4.8) to obtain the SSC profile $c(\sigma, t)$, the initial and boundary conditions are specified as follows:

Initial condition:

$$c(\sigma, 0) = c_0(\sigma) \quad (4.9)$$

Zero settling flux boundary condition at the water surface ($\sigma=0$):

$$(\omega_s c) \Big|_{\sigma=0} = 0 \quad (4.10)$$

Zero settling flux boundary condition at the bottom ($\sigma=-1$):

$$(\omega_s c) \Big|_{\sigma=-1} = 0 \quad (4.11)$$

Based on the above boundary value formulation, one can approximately calculate the settling velocity, ω_s , as a function of SSC. This analysis has been programmed by Mehta and Li (1997). Accordingly, the constants a , b , α and β in the settling velocity formula (3.30) can be determined by best-fitting Eq. (3.30) against the data points (for settling velocity against SSC). To determine the coefficients in settling velocity formula (3.30), the effects of temperature and salinity on flocculation are neglected and the settling velocity formula is simplified as

$$\omega_s = \frac{ac^\alpha}{(c^2 + b^2)^\beta} \quad (4.12)$$

Through best-fitting of the calculated data points, the values of the coefficients in Eq. (4.12) are obtained as: $\alpha=0.045$, $b=6$, $\alpha=1.5$ and $\beta=1.51$ during neap tide (Figure 4.27), and $\alpha=0.23$, $b=10$, $\alpha=1.5$ and $\beta=1.8$ during spring tide (Figure 4.28). These values are consistent with c (=SSC) measured in kg m^{-3} and ω_s measured in m s^{-1} . It is observed that the maximum SSC for flocculation settling, c_2 (approximately equal to b), increases during spring tide compared with neap tide, with $c_2=6.0 \text{ kg m}^{-3}$ during neap and $c_2=8.4 \text{ kg m}^{-3}$ during spring. In contrast, the settling velocity during spring tide is less than during neap tide (Figures 4.27 and 4.28). Also shown in Figures 4.27 and 4.28 is the data point of Li, et al.

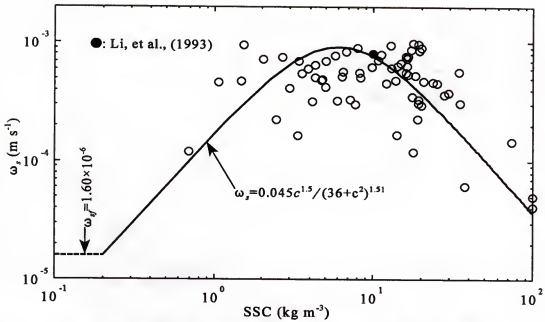


Figure 4.27. Settling velocity as a function of SSC during a neap tide from 0900 hr on 11/10/94 to 1000 hr on 11/11/94. Solid line is the best-fit of the calculated data points using Eq. (4.12).

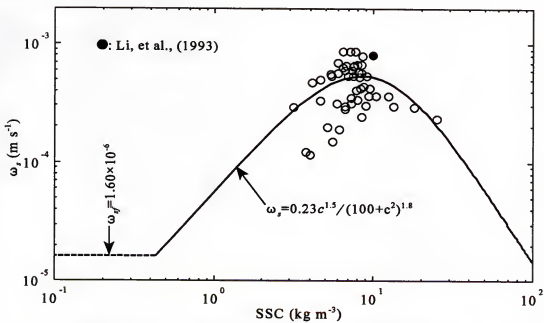


Figure 4.28. Settling velocity as a function of SSC during a spring tide from 1700 hr on 11/05/94 to 1800 hr on 11/06/94. Solid line is best-fit of the calculated data points using Eq. (4.12).

(1993) determined using the Postma's 'pipette' method (McCave, 1979) during the 1991 campaign in the Jiaojiang (Table 4.1). Finally note that in both plots ω_{sf} is the free settling velocity.

As described by Burt (1984), the tidal range, or associated turbulence has two effects on flocculation and, consequently, the settling velocity. Increasing turbulence may enhance flocculation and at the same time limit the size of flocs that can be sustained. In other words, depending on its cumulative effects in enhancing flocculation and limiting floc size, increasing turbulence may either increase or decrease the settling velocity. In the Jiaojiang, limiting floc size apparently dominated during spring tide, while enhanced flocculation occurred during neap.

4.3.6 Erosion Rate Constant

The erosion rate constant, M_{max} , in Eq. (3.29) can be determined from the vertical profiles of current velocity and SSC shown in Figures 4.4-4.9. The vertical profiles chosen for this purpose are those corresponding to periods when the suspended sediment mass in the entire water column increased gradually, usually 3-4 hr during each period of measurement. Also, the following assumptions are made:

- (1) SSC is approximately uniform along the estuary, so that the longitudinal advection term in the sediment conservation equation (3.15) can be omitted, i.e., $u\partial c/\partial x \approx 0$.
- (2) Within a short erosion period of 3-4 hr, the bottom shear strength can be approximately taken as constant.

(3) The effect of temperature on erosion rate is negligible.

From the data two parameters are obtained, i.e., the terms in Eq. (3.29) including the excess bottom shear stress, $\exp(-\chi\tau_s^\lambda) (\tau_b - \tau_s)$, and the erosion rate, m_e . The bottom shear stress is calculated from the vertical mean velocity according to

$$\tau_b = \frac{\rho g n_f^2 U^2}{H^{1/3}} \quad (4.13)$$

where n_f is the Manning's bed resistance coefficient taken as 0.015 (Dong et al., 1997), and U is the vertical mean velocity. The bottom shear strength is taken as the bottom shear stress at the beginning of each selected time period. Also, according to Lee and Mehta (1994), the values of $\chi=8$ and $\lambda=0.5$ are applicable. Finally, the erosion rate is calculated from the SSC profiles according to

$$m_e = \frac{C^{n+1} H^{n+1} - C^n H^n}{\Delta t} \quad (4.14)$$

where C is the vertical mean SSC, superscript n denotes time and Δt is the time interval between two profiles.

Through best-fitting of the data points (Figure 4.29), the erosion rate constant, $M_{max} = 0.29 \text{ kg N}^{-1} \text{ s}^{-1}$ is obtained. Vinzon (1998) obtained erosion rate constants by analyzing prototype data collected by Kineke (1993) in the same way. Her data yielded the range of M_{max} to be 0.25-0.34 $\text{kg N}^{-1} \text{ s}^{-1}$.

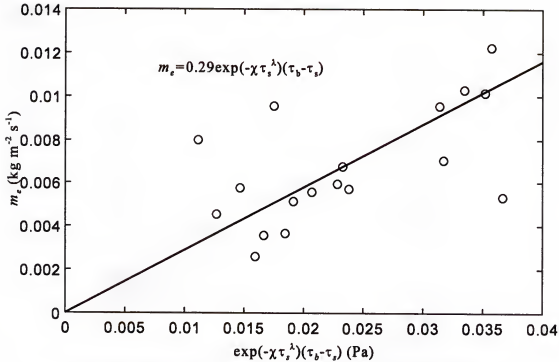


Figure 4.29. Erosion rate as a function of excess bottom shear stress.

4.4 Properties of Internal Waves

The results in Section 4.3.4 show that both the rms height, H_s , and the modal frequency, ω_a , of internal waves decrease with increasing Ri_0 . An attempt is made here to explain this behavior by referring to works of previous researchers. Also examined in this section are the celerity and length of internal waves.

4.4.1 Effect of Ri_0 on H_s

Since high Ri_0 implies high buoyancy-induced stabilization of the lutocline, increasing Ri_0 should correlate with decreasing wave height. As described in Section 1.2, this phenomenon has been observed by previous investigators in laboratory experiments on

lutoclines (e.g., Mehta and Srinivas, 1993) and on other pycnocline (e.g., Chou, 1975; Narimousa and Fernando 1987). By assuming that the interfacial undulations are due to the energy-containing, mixed-layer eddies impinging on the density interface, Narimousa and Fernando (1987) established an empirical relationship between the wave height, H_s , and Ri_0 as follows

$$\frac{H_s}{h_{mix}} \propto Ri_0^{-1/2} \quad (4.15)$$

In Eq. (4.15), h_{mix} is the mixed-layer thickness, i.e., the upper layer depth. According to this expression, H_s decreases with increasing Ri_0 with a slope of 0.5 on a log-log plot. As noted in Section 4.3.4, the observations in Jiaojiang do show that H_s decreases with increasing Ri_0 , although slopes much smaller than 0.5 were found (Figures 4.19 and 4.23, and Table 4.2). This difference in slopes between the Jiaojiang and the laboratory results of Narimousa and Fernando (1987) is believed to be mainly due to different physical scales and associated hydrodynamic effects including the degree of turbulence and eddy lengths.

4.4.2 Effect of Ri_0 on ω_a

In order to examine the influence of the Richardson number on the modal frequency of internal waves, the work of Lamb (1945) is introduced here. Lamb analytically examined internal waves at the interface of two inviscid fluids of densities ρ_1 and ρ_2 , one beneath the other, and moving parallel to the x -axis with velocities U_1 and U_2 , respectively (Figure

4.30). By assuming both fluids to be of unlimited depth and taking the wave profile as

$$H_a(x,t) = \frac{H_s}{2} e^{i(\omega_a t - kx)} \quad (4.16)$$

Lamb derived the following expression of the dispersion relationship for the waves:

$$\frac{\omega_a}{k} = \frac{\rho_1 U_1 + \rho_2 U_2}{\rho_1 + \rho_2} \pm \left\{ \left[\frac{g(\rho_2 - \rho_1)}{k(\rho_1 + \rho_2)} - \frac{\rho_1 \rho_2}{(\rho_1 + \rho_2)^2} (U_2 - U_1)^2 \right] \right\}^{\frac{1}{2}} \quad (4.17)$$

where k is the wave number. The first term on the right-hand side of Eq. (4.17) is referred to as the vertically-averaged velocity, U , of the two layers. It is seen that the values of ω_a given by (4.17) are imaginary if

$$\frac{g(\rho_2 - \rho_1)}{\rho_1 k (U_2 - U_1)^2} < \frac{\rho_2}{\rho_1 + \rho_2} \approx \frac{1}{2} \quad (4.18)$$

and it is also recognized that for two fluids of nearly equal densities, such as water and fluid mud, $\rho_2/(\rho_1 + \rho_2) \approx 0.5$.

It is evident that under the condition imposed by (4.18), two possible cases can arise with respect to the sign of the second term of Eq. (4.17). Considering Eqs. (4.16) and (4.17), it is seen that taking the plus sign the wave height will dissipate with time. This inherently implies that the interface will be stable. On the other hand, if the minus sign is taken, the wave height will grow with time. In other words, the interface will be unstable. For the present analysis, only the unstable mode is of interest, i.e., with the minus sign relative to the second term in Eq. (4.15). Thus, as soon as (4.18) is satisfied the interface will become

unstable. This is known as the Kelvin-Helmholtz instability (Delisi and Corcos, 1973). If now one considers the internal waves of all likely wavelengths in the estuarine setting such as in the Jiaojiang, it can be concluded that sufficiently short waves will be present to cause interfacial instability. Therefore, a two-layered estuarine shear flow characteristically unstable.

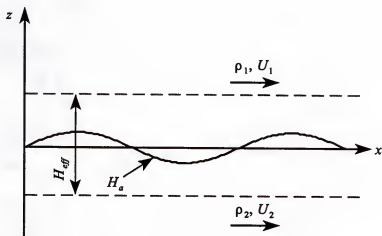


Figure 4.30. Definition sketch of two-layered flow system.

Based on the above, holding ρ_1 and ρ_2 constant, Eq. (4.17) can be restated as

$$\frac{\omega_a}{k} = U - \left[A_a - B_a H_{eff}^2 \left(\frac{U_2 - U_1}{H_{eff}} \right)^2 \right]^{\frac{1}{2}} \quad (4.19)$$

where $A_a = g(\rho_2 - \rho_1) / k(\rho_1 + \rho_2)$, $B_a = \rho_1 \rho_2 / (\rho_1 + \rho_2)^2$ and H_{eff} is the effective water depth defined as the thickness affected by internal waves. Further holding the wave number k and the mean velocity U constant, one may quantitatively evaluate the influence of the velocity

gradient, $|U_2 - U_1|/H_{eff}$, on ω_a . Thus, Eq. (4.19) can be expressed in terms of a stream Richardson number, Ri_s , as

$$\frac{\omega_a}{k} = U \left[A_a - \frac{B_a' H_{eff}}{Ri_s} \right]^{\frac{1}{2}} \quad (4.20)$$

where $B_a' = B_a g(\rho_2 - \rho_1)/\rho_1$ and Ri_s can be conveniently defined as

$$Ri_s = \frac{g(\rho_2 - \rho_1) H_{eff}}{\rho_1 (U_2 - U_1)^2} \quad (4.21)$$

Thus Ri_s is conceptually analogous to Ri_0 [Eq. (3.26)]. From Eq. (4.20), it is seen that ω_a decreases as Ri_s increases, an observation that is consistent with the data in Figures 4.20 and 4.24.

4.4.3 Celerity and Wave Length

In order to further understand the properties of internal waves at the lutocline in the Jiaojiang, the celerity and wave length are calculated here. For simplification, the flow is treated as two-layered system with fluid densities of ρ_1 and ρ_2 in upper and lower layers, respectively. Once the reduced gravity $g' [=g(\rho_2 - \rho_1)/\bar{\rho}]$ and the lutocline elevation above the bottom ζ_a are known, the celerity C_a and the wave length λ_a can be calculated according to (Lamb, 1945)

$$C_a = \sqrt{\frac{g'}{k} \tanh(k\zeta_a)}, \quad \lambda_a = \frac{2\pi g'}{\omega_a^2} \tanh(k\zeta_a) \quad (4.22)$$

where k is the wave number ($=2\pi/\lambda_a$). From the measured SSC profiles (Figure 4.9),

lutocline elevation (Figure 4.12) and the modal frequency of internal waves (Section 4.3.4), the calculated results for examples (a), (b) and (c) in Figure 4.12 are presented in Table 4.3. For these calculations, the mean lutocline elevation was taken for each ASSM segment, and an iteration method was used in solving Eq. (4.22).

From Eq. (4.18), one can calculate the critical wave length, λ_{ac} , below which the interface will become unstable, i.e., the Kelvin-Helmholtz (Delisi and Corcos, 1973) or Holmboe (Browand and Wang, 1972) instabilities due to interfacial shear. By equating the two sides of Eq. (4.18) one obtains

$$\lambda_{ac} = \frac{2\pi\rho_1\rho_2(U_2-U_1)^2}{g(\rho_2-\rho_1)} \approx \frac{\pi h_{mix}}{Ri_0} \quad (4.23)$$

Values of λ_{ac} calculated from Eq. (4.23) are given in Table 4.3. Also listed in Table 4.3 are the Brunt-Väisälä frequencies calculated from Eq. (4.7).

From Table 4.3 it is seen that the high frequency waves were characteristically in deep water, with the ratio ζ_a/λ_a on the order of 5 ($\gg 0.5$), whereas the low frequency waves were close to the shallow water regime, with ζ_a/λ_a on the order of 0.07 (≈ 0.05). It is also observed that the celerity and wave length increased with increasing Richardson number for both high and low frequency waves. Observe that λ_{ac} decreased with increasing Richardson number (ranging from 2.71 m to 0.06 m). Thus, the wave lengths for high frequency internal waves (ranging from 0.39 m to 0.65 m) are between the maximum and minimum critical wave lengths for stability. This suggests that the high frequency waves are generated by forcing due to interfacial shear.

Table 4.3. Celerity and length of internal waves

No.	ζ_a (m)	h_{mix} (m)	g' (m s ⁻²)	Ri_0	ω_v (rad s ⁻¹)	Low frequency wave			High frequency wave			λ_{ac} (m)
						ω_a (rad s ⁻¹)	C_a (m s ⁻¹)	λ_a (m)	ω_a (rad s ⁻¹)	C_a (m s ⁻¹)	λ_a (m)	
a	2.40	1.38	0.096	1.6	0.26	0.105	0.460	27.6	1.24	0.078	0.39	2.71
b	2.43	1.50	0.097	2.5	0.25	0.093	0.470	31.5	1.18	0.082	0.44	1.88
c	2.51	2.86	0.119	150	0.20	0.070	0.536	48.2	1.06	0.112	0.65	0.06

CHAPTER 5 TURBULENCE DAMPING IN FLUID MUD

5.1 Introduction

As stated in Chapters 1 and 2, the vertical mixing pattern of suspended sediment over the lutocline is highly dependent on the nature and intensity of turbulence in both layers. Laboratory experiment results (e.g., Wolanski, et al., 1989; Mehta and Srinivas 1993; Winterwerp and Kranenburg, 1997) and field investigations (e.g., Jiang and Wolanski, 1998) have revealed that upward mixing caused by the instability and breaking of internal waves at the lutocline occurs concurrently with turbulence damping within the fluid mud layer below.

Turbulence damping by suspended sediment was early examined by Einstein and Chien (1955). They argued that since part of the turbulent energy is used to maintain the sediment particles in suspension, turbulence is damped by the suspended sediment. Since then, turbulence damping in the fluid mud layer and consequent (vertically) asymmetric mixing over the lutocline have been commonly reported (e.g., Wolanski, et al., 1992; Scarlatos and Mehta, 1993; Kranenburg and Winterwerp, 1997; Jiang and Wolanski, 1998). However, there remains a lack of a theoretical basis as well as any direct evidence of this feature of mixing because of the difficulty in observing it in the field.

Here, turbulence damping in the fluid mud layer is examined on a phenomenological basis. Its effect on lutocline formation in the Jiaojiang is then explained.

5.2 Turbulence Damping and its Effect on Lutocline Formation

For a simplified treatment, we will consider a steady uniform flow, treat fluid mud as a Bingham plastic and omit advective effects.

The rate of production of turbulent energy associated with the Reynolds stress (per unit volume) can be expressed as $\tau_R \partial u / \partial z$ (Rossby and Montgomery, 1935). Based on the Prandtl mixing theory, Einstein and Chien (1955) proposed following formula for the Reynolds stress, τ_R , in a uniform flow

$$\tau_R = - \left[\frac{\rho_0 \overline{u'(\rho_s - c)w} - \overline{u'c(w - \omega_s)}}{\rho_s} \right] = \left(1 + \frac{\rho_s - \rho_0}{\rho_s \rho_0} c \right) \rho_0 l_m^2 \left(\frac{\partial u}{\partial z} \right)^2 \quad (5.1)$$

where u' is the turbulent fluctuation of the horizontal velocity in the x direction, l_m is the momentum mixing length, and the overbars denote time-averaging. Hence the rate of production of turbulent energy becomes

$$\tau_R \frac{\partial u}{\partial z} = \left(1 + \frac{\rho_s - \rho_0}{\rho_s \rho_0} c \right) \rho_0 l_m^2 \left(\frac{\partial u}{\partial z} \right)^3 \quad (5.2)$$

The rate of work done against buoyancy due to stratification is (Odd and Rodger, 1978)

$$gM_b = g l_c l_m \frac{\partial \rho}{\partial z} \left| \frac{\partial u}{\partial z} \right| = g \beta_m l_m^2 \frac{\partial \rho}{\partial z} \left| \frac{\partial u}{\partial z} \right| \quad (5.3)$$

where M_b is the vertical flux of buoyancy and β_m is the ratio of the mass mixing length, l_c , to the momentum mixing length, l_m , i.e., the turbulent Schmidt number.

The rate of work done against gravity is (Hunt, 1954)

$$gM_z = gC_m \overline{w'c'} \quad (5.4)$$

where M_z is the vertical mass flux and c' is the turbulent fluctuation of SSC. For a steady flow, from the sediment and water continuity considerations and the Prandtl mixing theory, Einstein and Chien (1955) obtained

$$\overline{w'c'} = \frac{\rho_s - c}{\rho_s} c\omega_s \quad (5.5)$$

Substituting Eqs. (3.27) and (5.5) into Eq. (5.4), rate of work done against gravity becomes

$$gM_z = \frac{g(\rho_s - \rho_0)(\rho_s - c)}{\rho_s^2} c\omega_s \quad (5.6)$$

The rate of work done against cohesion and interactions between the flocs in the fluid mud is

$$\tau_{\mu B} \frac{\partial u}{\partial z} = (\tau_{\mu} + \tau_B) \frac{\partial u}{\partial z} \quad (5.7)$$

where $\tau_{\mu B}$ is the total shear stress due to cohesion and interactions between the flocs and τ_{μ} is the shear stress due to the interactions between flocs. Bagnold (1954; 1956) examined the normal and tangential stresses in granular flows and suggested that they may be expressed

as functions of the shear rate, $\partial u/\partial z$, and a “linear sediment concentration”, c_λ , which characterizes the relative surface proximity between sediment particles (Figure 5.1). c_λ is related to the sediment concentration, c , by

$$c_\lambda = \frac{1}{(c_{max}/c)^{1/3} - 1} \quad (5.8)$$

where c_{max} is the maximum concentration corresponding to grain-grain contact.

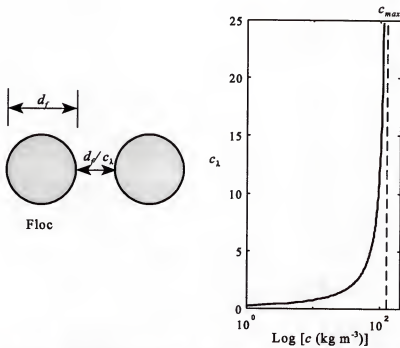


Figure 5.1. Definition of linear sediment concentration, c_λ , and its relationship with sediment concentration, c . d_f is the floc diameter.

Observe that c_λ increases drastically as c approaches c_{max} (Figure 5.1). For small, light grains in a very viscous fluid, Bagnold (1954; 1956) found that the behavior of the

mixture of fluid and cohesionless grains is dominated by viscosity due to interactions between particles, and termed it the macro-viscous regime. In this regime the shear stress has the form

$$\frac{\tau_{\mu}}{\tan\phi_d} = 1.3(1+c_{\lambda}) \left(1 + \frac{c_{\lambda}}{2} \right) \mu \frac{\partial u}{\partial z} \quad (5.9)$$

where ϕ_d is the dynamic angle of repose, which was found to be $\phi_d = 37^\circ$ (Bagnold, 1954; 1956), and μ is the dynamic viscosity of the fluid. To extend the applicability of this formula to fluid mud, it is reasonable to assume that the behavior of a mixture of fluid and cohesive sediment is phenomenologically analogous to the behavior of a mixture of fluid and cohesionless grains. Accordingly, Eq. (5.9) can be rendered applicable to the fluid mud merely by taking the dynamic viscosity μ to be that of the fluid mud, and treating flocs as basic particles.

Following the original arguments of Rossby and Montgomery (1935), under an assumed equilibrium condition the sum of the kinetic, potential and dissipated energy in a stratified and cohesive flow per unit mass can be considered to be the same as that in a homogeneous, non-cohesive flow at identical shear rates. Thus, combining Eqs. (5.2), (5.3), (5.5), (5.7) and (5.9) one obtains

$$\begin{aligned} \rho_0 I_m^2 \left(\frac{\partial u}{\partial z} \right)^3 &= \left(1 + \frac{\rho_s - \rho_0}{\rho_s \rho_0} c \right) \rho_0 I_m^2 \left(\frac{\partial u}{\partial z} \right)^3 + g \beta_m I_m^2 \frac{\partial \rho}{\partial z} \frac{\partial u}{\partial z} \\ &+ \frac{g(\rho_s - \rho_0)(\rho_s - c)}{\rho_s^2} c \omega_s + 1.3 \tan\phi_d (1 + c_{\lambda}) \left(1 + \frac{c_{\lambda}}{2} \right) \mu \left(\frac{\partial u}{\partial z} \right)^2 + \tau_B \frac{\partial u}{\partial z} \end{aligned} \quad (5.10)$$

Solving Eq. (5.10) for l_m leads to

$$\frac{l_m}{l_{m0}} = \sqrt{\frac{1 - Ri_\omega - Ri_\mu - Ri_B}{\alpha_m + \beta_m Ri}} \quad (5.11)$$

with

$$\begin{aligned} \alpha_m &= 1 + \frac{\rho_s - \rho_0}{\rho_s \rho_0} c \\ Ri_\omega &= \frac{(\rho_s - \rho_0)(\rho_s - c)c}{\rho_s^2 \rho_0} \frac{g \omega_s}{l_{m0}^2 (\partial u / \partial z)^3} \\ Ri_\mu &= 1.3 \tan \phi_d (1 + c_\lambda) \left(1 + \frac{c_\lambda}{2}\right) \frac{\mu}{\rho_0 l_{m0}^2 \partial u / \partial z} \\ Ri_B &= \frac{\tau_B}{\rho_0 l_{m0}^2 (\partial u / \partial z)^2} \end{aligned} \quad (5.12)$$

Here α_m is a dimensionless variable dependent on SSC, Ri_ω is the ratio of the potential energy of the sediment settling flux to the production of turbulent energy, $l_{m0}^2 (\partial u / \partial z)^3$, (denoted as F_s), Ri_μ is the ratio of the viscous force due to the interactions between flocs in the fluid mud to the Reynolds stress, and Ri_B is the ratio of Bingham yield stress to the Reynolds stress.

Equation (5.11) shows that at equilibrium the higher the potential settling flux of suspended sediment (as would occur in quiescent water), the smaller the turbulent mixing length. In other words, the turbulent kinetic energy is damped because part of it is used to maintain flocs in suspension. Due to hindered settling, the sediment settling flux will

decrease with increasing SSC (Ross and Mehta 1989). Thereafter, cohesion and the interactions between flocs can be expected to play an increasingly important role in turbulence damping. To demonstrate this behavior, one may introduce the following formulas and parameters:

(1) Settling Velocity: Here the floc settling velocity formula (3.30) is applied, with $a=0.085$, $b=10 \text{ kg m}^{-3}$, $\alpha=1.5$, $\beta=1.6$, and without considering the effects of salinity and temperature on flocculation.

(2) Bingham Yield Strength: The Bingham yield strength is expressed as a function of SSC as follows

$$\tau_B = \alpha_B c^{\beta_B} \quad (5.13)$$

Here α_B and β_B are sediment-dependent coefficients. Following Owen (1970) and Odd and Rodger (1986), $\alpha_B = 7.36 \times 10^{-6}$ and $\beta_B = 2.33$ are chosen.

(3) Momentum Mixing Length: In the near-bottom layer of a homogeneous, non-cohesive flow, the following Prandtl (1925) approximation for the momentum mixing length can be applied

$$l_{m0} = \kappa z_b \quad (5.14)$$

where z_b is the elevation above the bottom, and von Kármán constant κ is normally taken as 0.4.

(4) Velocity Profile: In the near-bottom layer, the velocity distribution will be considered to be a locally logarithmic, i.e.,

$$u(z_b) = \frac{u_{*0}}{\kappa} \ln \frac{z_b}{z_0} \quad (5.15)$$

Where u_{*0} is the bottom frictional velocity in homogenous flow.

(5) Viscosity of Fluid Mud: Following Odd and Rodger (1986), the viscosity of fluid mud, μ , with $SSC < 80 \text{ kg m}^{-3}$, which is the critical SSC for soil formation, will be taken as 0.01 Pa s .

(6) Water and Granular Densities: Values of water and granular densities taken here are $\rho_0 = 1,000 \text{ kg m}^{-3}$ and $\rho_s = 2,650 \text{ kg m}^{-3}$.

(7) Maximum Concentration: As mentioned above, for interactions between particles in fluid mud the flocs are treated as basic particle units. Hence the maximum concentration, c_{max} , should correspond to floc-floc contact. Flocs tend to be very loosely bound and are light in water, with a typical bulk density, ρ_f , of about $1,080\text{-}1,150 \text{ kg m}^{-3}$, which will contain nearly 95% by volume of water locked within the interstitial particulate fabric (Mehta and Li, 1997). Accordingly, the maximum concentration corresponding to the floc-floc contact can be expressed as

$$c_{max} = \frac{(\rho_0 - \rho_f) c_{vmax}}{C_m} \quad (5.16)$$

Where c_{vmax} is the maximum volumetric floc content corresponding to floc-floc contact. In analogy with the water-sand mixture (Bagnold, 1956), $c_{vmax} = 0.65$ will be chosen.

Substituting the above parameters and expressions into Eq. (5.11), the ratio of l_m/l_{m0} is calculated and plotted in Figure 5.2 as a function of SSC and the production of turbulent energy, F_s , below $SSC < 80 \text{ kg m}^{-3}$ without considering the effects of buoyancy. Also shown is the sediment settling flux as a function of SSC. It is observed that within the flocculation settling range, maximum turbulence damping is consistent with the maximum settling flux. Thus, a lutocline can be expected at the elevation of the maximum settling flux in the water column. As soon as the lutocline is formed, the buoyancy effect due to sediment-induced stratification will enhance turbulence damping as indicated in Eq. (5.11). This in turn will accentuate the lutocline. Figure 5.2 also shows that in the range of hindered settling, turbulence damping decreases due to decreasing sediment settling flux for $F_s < 0.0001 \text{ m}^2 \text{ s}^{-3}$. However, above $SSC > 40\text{-}50 \text{ kg m}^{-3}$ damping increases drastically as the effects of cohesion and interactions between flocs become significant. Turbulence collapse subsequently occurs. Thus, turbulence damping is governed by the potential settling flux in the flocculation settling range, and by cohesion and interactions between flocs in the hindered settling range with $SSC > 40\text{-}50 \text{ kg m}^{-3}$. Overall, flocculation settling, turbulence damping due to settling flux, cohesion and interactions between flocs in fluid mud as well as the buoyancy effect due to sediment-induced stratification contribute to the formation of a lutocline. This analysis thus replicates the conclusion arrived at by Ross and Mehta (1989) based solely on the concept of density stratification. However, the explanation provided here introduces new parameters, namely Ri_ω , Ri_μ and Ri_B .

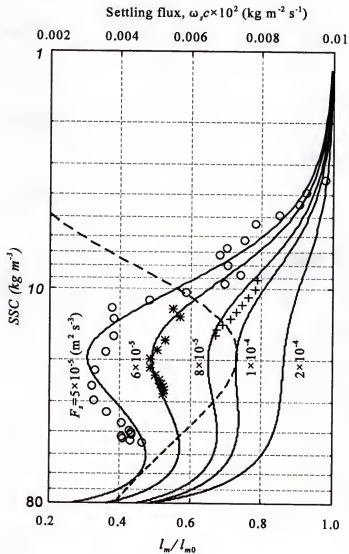


Figure 5.2. Relative momentum mixing length calculated from theoretical formula (solid lines) and field data (data points) and settling flux (dashed line) as functions of SSC.

Also observed in Figure 5.2 is that turbulence damping is dependent not only on SSC, but also on flow. Thus, beyond $F_s > \sim 0.0002 \text{ m}^2 \text{ s}^{-3}$, the ratio l_m/l_{m0} approaches unity, i.e.,

there is no significant damping and, as a result, mixing will occur in two ways, i.e., both upward and downward. The lutocline will be ruptured and become less distinct. This conclusion is supported by the observations of Jiang and Wolanski (1998) in the Jiaojiang, where it was found that a distinct lutocline only appears during slack water at neap tide when the production of turbulent energy, F_s , is usually less than $0.0002 \text{ m}^2 \text{ s}^{-3}$.

To examine the relationship between lutocline formation and the flow condition, an analysis of vertical profiles of SSC and velocity in the 1991 and 1994 field campaigns in the Jiaojiang (Table 4.1) is considered here. The result is shown in Figure 5.3 in terms of a lutocline strength index, L_s , as a function of the production of turbulent energy. Here, L_s is defined as

$$L_s = \frac{(\partial c / \partial z)_{\text{mean}}}{(\partial c / \partial z)_{\text{max}}} \quad (5.17)$$

where subscripts “max” and “mean” denote the maximum and the mean values of the SSC gradient, $\partial c / \partial z$, over the water column, respectively. $L_s = 1$ indicates that there is a uniform vertical distribution of the SSC and no lutocline. The vertical gradient of SSC is calculated from

$$\frac{\partial c}{\partial z} = \frac{c_{k+1} - c_k}{dz} \quad (5.18)$$

where subscript “ k ” denotes the measurement elevation and dz is the height between k and $k+1$. Figure 5.3 shows the results and the mean trend line. It is evident that the lutocline becomes less distinct as the turbulent energy production $F_s > \sim 0.0003 \text{ m}^2 \text{ s}^{-3}$. Relatively

high value of F_s , at which the lutocline became less distinct, are found because the buoyancy effect due to sediment-induced stratification was not considered in Figure 5.2.

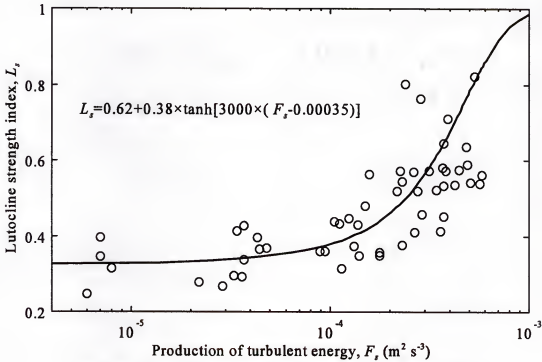


Figure 5.3. Lutocline strength index as a function of turbulence energy production based on measured profiles of SSC and velocity. The equation represents the best-fit line.

5.3 Mixing Length in the Jiaojiang

From the Jiaojiang ASSM field data (e.g., Figure 4.10), it is possible to examine the standard deviation of SSC, σ_d , which has the form

$$\sigma_d = \sqrt{\frac{\overline{c'^2}}{c^2}} = \sqrt{\frac{1}{T_d} \int_0^{T_d} \left(\frac{c}{c} - 1 \right)^2 dt} \quad (5.19)$$

where T_d is the period over which σ_d is calculated and the overbar expresses time averaging over a period of T_d . Here T_d will be taken as 2.5 min as a characteristic duration. c is calculated from Eq. (4.1) by using ASSM records. Considering that Eq. (5.19) is applied to a fixed elevation above bottom, i.e., $h' = \text{constant}$, Eq. (4.1) becomes

$$c = AF_a^2 \quad (5.20)$$

where A is a sediment and elevation dependent constant. By assuming that σ_d is proportional to the local Prandtl mixing length and the vertical gradient of SSC, one obtains

$$\overline{c'^2} = \beta_m^2 l_m^2 \left(\frac{\partial \bar{c}}{\partial z} \right)^2 \quad (5.21)$$

For a homogeneous flow, assuming that the shear stress near the bottom, τ_{zx} , is constant, the local Prandtl mixing length is obtained as

$$l_{m0} = \sqrt{\frac{\tau_{zx}/\rho}{(\partial u/\partial z)^2}} = \frac{u_*}{\partial u/\partial z} \quad (5.22)$$

Combining Eqs. (5.19), (5.20), (5.21) and (5.22), one obtains

$$\frac{l_m}{l_{m0}} = \frac{\frac{\partial u}{\partial z}}{\beta_m u_*} \frac{F_a^2}{\partial F_a^2/\partial z} \sqrt{\frac{1}{T_d} \int_0^{T_d} \left(\frac{F_a^2}{F_a^2} - 1 \right)^2 dt} \quad (5.23)$$

The values of l_m/l_{m0} were evaluated by Eq. (5.23) using ASSM records and measured velocity profiles (Figure 4.6). The results are plotted in Figure 5.2, where it is observed that the trends in mixing length follow Eq. (5.11).

5.4 Modified Vertical Momentum and Mass Diffusion Coefficients

The above results suggest that to calculate the turbulent diffusion coefficients in a cohesive sediment transport model, it is essential to consider the effects of potential settling flux, cohesion and interactions between flocs as well as sediment-induced stratification, as embodied in Eq. (5.11). Accordingly, the turbulent diffusion coefficient formulas (3.39) and (3.40) are modified following Munk and Anderson (1948) analog as:

Momentum diffusion coefficient:

$$A_v = A_{v0} \left(\frac{1 - d_1(Ri_\omega + Ri_\mu + Ri_B)}{\alpha_m + b_1 Ri} \right)^{\gamma_1} + A_{vb} \quad (5.24)$$

Mass diffusion coefficient:

$$K_v = K_{v0} \left(\frac{1 - d_2(Ri_\omega + Ri_\mu + Ri_B)}{\alpha_m + b_2 Ri} \right)^{\gamma_2} + K_{vb} \quad (5.25)$$

where $d_1 (\leq 1)$ and $d_2 (\leq 1)$ are the sediment-dependent coefficients relating the effect of suspended sediment on the mixing length.

CHAPTER 6 LUTOCLINE DYNAMICS IN THE JIAOJIANG

6.1 Introduction

COHYD-UF and COSED-UF are now applied to simulate lutocline and associated fluid mud dynamics in the Jiaojiang. The modeled results include tidal variations of velocity, SSC and the lutocline layer, lutocline layer thickness and hysteresis loops of SSC, and these are compared with the data obtained *in situ*. Relevant formulations of the flow and sedimentary processes modeled are summarized in Section 6.2. Applications of the numerical models are described in Section 6.3. Finally, simulations along with the data are presented in Section 6.4.

6.2 Parameters for Flow and Sedimentary Processes

Descriptions of the models and relevant flow and sedimentary formulations are given in Chapters 3, 4 and 5. Table 6.1 summarizes these formulations and relevant parameters in modeling sediment dynamics in the Jiaojiang. The most important parameters, including the settling velocity, erosion rate constant, momentum and mass diffusion coefficients, consolidation rate, and the effective roughness of the bed, were determined through analyses of field data and/or model calibration. Others were introduced from the works of previous researchers.

Table 6.1. Flow and sedimentary process formulations and parameters

Model	Formula	Parameter	Source
Vertical momentum diffusion coefficient	$A_v = A_{v0} \times \left(\frac{1 - d_1(Ri_w + Ri_\mu + Ri_{\beta})^{\gamma_1}}{\alpha_m + b_1 Ri} \right) + A_{vb}$ $A_{v0} = \alpha_u H(-\sigma)(1 + \sigma)$	<ol style="list-style-type: none"> ① $A_{vb} = 10^{-6} \text{ m}^2 \text{ s}^{-1}$ ② $\kappa = 0.4$ ③ $b_1 = 10, \gamma_1 = -0.5$ ④ $d_1 = 0.75$ 	<ol style="list-style-type: none"> ① Molecular diffusion ② von Kármán constant ③ Munk and Anderson (1948) ④ Model calibration
Vertical mass diffusion coefficient	$K_v = K_{v0} \times \left(\frac{1 - d_2(Ri_w + Ri_\mu + Ri_{\beta})^{\gamma_2}}{\alpha_m + b_2 Ri} \right) + K_{vb}$ $K_{v0} = \alpha_\lambda \alpha_u H(-\sigma)(1 + \sigma) + \beta_u H\left(\frac{-\sigma}{0.9}\right)^3 \text{ for } \sigma \geq -0.9$ $K_{v0} = \alpha_\lambda \alpha_u H(-\sigma)(1 + \sigma) + \beta_u H\left(\frac{1 + \sigma}{0.1}\right)^3 \text{ for } \sigma \leq -0.9$	<ol style="list-style-type: none"> ① $K_{vb} = 10^{-6} \text{ m}^2 \text{ s}^{-1}$ ② $b_2 = 3.33, \gamma_2 = -1.5$ ③ $d_2 = 0.75$ ④ $\alpha_\lambda = 1.00$ ④ $\alpha_\lambda = 0.038$ 	<ol style="list-style-type: none"> ① Molecular diffusion ② Munk and Anderson (1948) ③ Model calibration ④ Jobson and Sayre (1970)
Horizontal momentum and mass diffusion coefficients	Constant	$A_x = 5 \text{ m}^2 \text{ s}^{-1}$ $A_y = 3 \text{ m}^2 \text{ s}^{-1}$ $K_x = 5 \text{ m}^2 \text{ s}^{-1}$ $K_y = 3 \text{ m}^2 \text{ s}^{-1}$	Model calibration
Bottom shear stress	$\bar{\tau}_b = \rho C_D \bar{v} \left \bar{v} \right \sqrt{1}$ <p>with $C_D = \left\{ \kappa \left[\ln(z_v/z_0) + \Psi(z_v/L_\lambda) \right] \right\}^2$</p>	<ol style="list-style-type: none"> ① $z_0 = 0.7 \text{ mm}$ ② $z_v = 0.05H \text{ m}$ 	<ol style="list-style-type: none"> ① Model Calibration ② Lowest layer Modeled
Stratification function	$\psi = 1 + \alpha_\lambda \frac{z}{L_\lambda}$	$\alpha_\lambda = 4.7$	Businger, et al., (1971)
Lateral friction coeff.	Constant	$C_f = 0.003$	Empirical value

Table 6.1--continued

Monin-Obukhov length	$L_s = u_*^3 / \{k^2 g z [\rho_s - \rho] / \rho\} \partial c / \partial z\}$	—	Monin and Obukhov (1953)
Fluid density	$\rho = \rho_0 + C_m c$ with $C_m = (\rho_s - \rho_0) / P_s$	<ol style="list-style-type: none"> ① $\rho_0 = 1,012 \text{ kg m}^{-3}$ ② $\rho_s = 2,650 \text{ kg m}^{-3}$ 	<ol style="list-style-type: none"> ① Dong, et al., (1997) ② Commonly used value
Bottom erosion	$m_e = M_{max} \exp(-\chi \tau_s^3) \times [\Theta \exp(\Delta - \Delta(\Theta))] [\tau_b - \tau_s]$ $\tau_s = \tau_{s0} + \alpha_1 (\phi - \phi_c)^\beta$ for $\tau_b \geq \tau_s$	<ol style="list-style-type: none"> ① $M_{max} = 0.29 \text{ kg m}^{-2} \text{ s}^{-1} \text{ N}^{-1}$ ② $\chi = 8, \lambda = 0.5$ ③ $\tau_{s0} = 0.15 \text{ Pa}$ ④ $\alpha_1 = 6.5, \beta_1 = 1$ ⑤ $\phi_c = 0.03$ 	<ol style="list-style-type: none"> ① Analysis of field data ② Lee and Mehta (1994) ③ Nicholson and O'Connor (1986) ④ Mehta (1991b) ⑤ James, et al., (1988)
Deposition	$m_d = \omega_{s0} C_b (1 - \tau_b / \tau_d)$ for $\tau_b \leq \tau_d$	$\tau_d = 0.1 \text{ Pa}$	Krone (1962)
Interfacial entrainment	$m_{en} = A_E R_E^{-1} - D_E R_E$	$A_E = 5.2 \times 10^{-3}$ $D_E = 1.6 \times 10^{-5}$	Mehta and Srinivas (1993)
Settling velocity	$\omega_s = [ac^\alpha / (c^2 + b^2)^\beta] F(\theta)$ $[\rho_s / \rho(\theta_{s,c}) - 1] / 1.65 [10^{-6} / \nu(\theta_{s,c})]$ $F(\theta) = 1.776 - 0.0518\theta$ for $\theta = 0 - 30^\circ \text{C}$	<p>During spring tide: $a = 0.23, b = 10$ $\alpha = 1.5, \beta = 1.8$</p> <p>During neap tide: $a = 0.045, b = 6$ $\alpha = 1.5, \beta = 1.51$</p>	Analysis of field data

Table 6.1--continued

Consolidation rate	$\omega_{ac} = \omega_{ac1} \exp(-c/c_{s1}) F_t + \omega_{ac2} (1 - c/c_{s2})^m (1 - F_t)$ $F_t = \exp[-(c/c_t)^{n_t}]$	$\omega_{ac1} = 1 \times 10^{-4} \text{ m s}^{-1}$ $\omega_{ac2} = 6 \times 10^{-6} \text{ m s}^{-1}$ $c_{s1} = 31 \text{ kg m}^{-3}$ $c_{s2} = 350 \text{ kg m}^{-3}$ $c_t = 210 \text{ kg m}^{-3}$ $n_t = 4.5, n_r = 15$	Model calibration
Fully consolidated bed	$c = \bar{C} \alpha_2 \left(\frac{h_b - \Delta z}{h_b} \right)^{\beta_2}$	$\bar{C} = 350 \text{ kg m}^{-3}$ $h_b = 1 \text{ m}, \alpha_2 = 0.857$ $\beta_2 = -0.368$	Mehta, et al., (1982)
Bingham yield strength	$\tau_B = \alpha_B c^{\beta_B}$	$\alpha_B = 7.36 \times 10^{-6}$ $\beta_B = 2.33$	Owen (1970) Odd and Rodger (1986)
Water viscosity	Constant	$\nu = 10^{-6} \text{ m}^2 \text{ s}^{-1}$	Known value
Maximum volumetric flocc content corresponding to flocc-flocc contact	Constant	$c_{vmax} = 0.65$	Bagnold (1956)
Initial concentration of deposited sediment	Constant	$c_f = 80 \text{ kg m}^{-3}$	Odd and Rodger (1986)
Angle of repose	Constant	$\phi_d = 37^\circ$	Bagnold (1956)

6.3 Model Application

6.3.1 Modeled Domain, Initial and Boundary Conditions

The modeled region includes the area from the mouth to the upstream tributary (Figure 4.1), with a length of 13.4 km. The domain was discretized using spatial steps $\Delta x = \Delta y = 200$ m and $\Delta \sigma = 0.1$, with the total number of rectangular cells $M \times N \times L_f = 67 \times 13 \times 10 = 8,710$. Figure 6.1 shows the bathymetry and numerical mesh in the horizontal plane within the modeled domain. A time step $\Delta t = 30$ s was adopted based on stability constraints resulting from the numerical scheme involving the back-tracing approach mentioned in Section 3.5.4 [Eq. (3.50)]. The lowest layer near the bottom was $0.05H$ above the bed and the highest layer near the surface was $0.05H$ below the instantaneous water surface.

The initial conditions for COHYD-UF runs were as follows: (a) All velocities were set equal to zero, and (b) water elevation at each point was generated through linear interpolation of the prescribed values at the open boundaries based on measurements. For COSED-UF, the initial SSC was obtained by the same interpolation approach using the values at the open boundaries from measurements. Once a stable flow field resulted from COHYD-UF model, which took about 6 hr (one-half tidal cycle), COSED-UF run was initiated.

Stations T1 and T5 (Figure 4.1) were selected to prescribe the open boundary conditions for the water surface elevation. The following 11 tidal constituents were considered at these boundaries: Q_1 , O_1 , P_1 , K_1 , N_2 , M_2 , S_2 , K_2 , M_4 , $M_{3/6}$ and $M_{5/6}$. All

harmonic components were assumed to be constant in phase and amplitude over the cross-section of each open boundary.

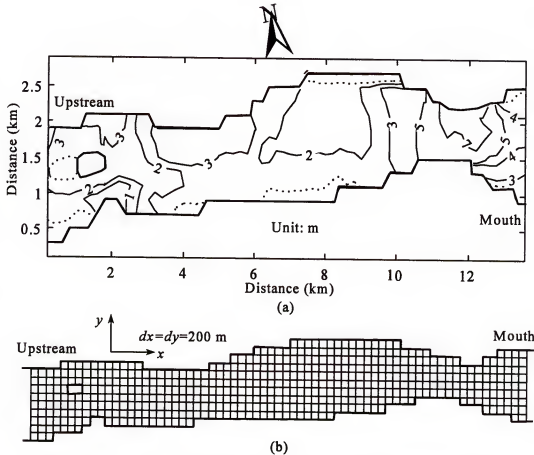


Figure 6.1. Bathymetry in the modeled domain of the Jiaojiang (a), where the datum is mean water level and the regions enclosed within dotted lines are mudflats, and the numerical plane mesh in the horizontal plane (b).

Measured SSC values at sites C1 and C3 (Figure 4.1) were inputted as the open boundary conditions for COSED-UF. Since there were only one measurement station over the cross-section of each open boundary (located in the middle as shown in Figure 4.1), it was assumed that the SSC was uniform over the entire cross-section of the open boundaries.

In reality there is always a certain amount of lateral variation of SSC, even in narrow channels. Consequently, this uniformity approximation can lead to a noticeable error in simulations results within the modeled domain. This aspect will be discussed further in Section 6.4. Because SSC observations were made at variable elevations using a turbidimeter lowered from the boat, the SSC values at fixed elevations had to be obtained through cubic spline interpolations.

Currents and SSC at sites C2 and C4 (Figure 4.1) were used to verify the simulations. Model tests were run over the same period as the field campaign, i.e., from November 4, 1994 (spring tide) to November 12, 1994 (neap tide). Simulated flow field and SSC profiles at the same time as observations at C2 and C4 were outputted for verification and analysis.

6.3.2 Sediment Deposition, Erosion, Consolidation and Entrainment

1. Deposition and Erosion: When $\tau_b \leq \tau_d$, sediment deposition occurs (Section 3.3.3 and Table 6.1). Within a time step, Δt , the rate of deposition, m_d , is assumed to be constant and calculated by the formula in Table 6.1. When $\tau_b \geq \tau_s$, where τ_s is a function of sediment concentration, bottom erosion occurs (Section 3.3.3 and Table 6.1). First eroded is the consolidating layer and then the fully consolidated bed. Within time step, Δt , erosion continues until $\tau_b \leq \tau_s$ is encountered. When $\tau_d \leq \tau_b \leq \tau_s$, it is assumed that deposition and erosion are in equilibrium, i.e., the sediment vertical flux at the bed-fluid interface, $m_e - m_d$, is zero. Deposition and erosion are incorporated in COSED-UF through the bottom boundary condition, i.e., Eq. (3.17).

2. Consolidation: The deposited material is combined with the consolidating sediment layer having an initial sediment concentration of c_f (Table 6.1), and goes through consolidation (Sections 3.3.3 and 3.5.3). When sediment concentration near the bottom of the consolidating layer is greater than the maximum compaction concentration, c_{s2} , this portion of the deposit is combined with the fully consolidated bed.

During deposition, bottom erosion and consolidation of freshly deposited sediment, although the heights of the consolidating and the fully consolidated layers vary with time, the bottom datum remains constant.

3. Entrainment: Interfacial entrainment discussed in Section 3.3.3 and turbulent diffusion in Section 3.4.2 and Chapter 5 are facets of interfacial mixing in a stratified flow, and are referred to as pure entrainment mixing and the pure turbulent-diffusion mixing. Grubert (1990) noted that pure entrainment mixing takes place when the interfacial transition layer (or lutocline layer) is in a subcritical state. In this condition, cusp motions generated by interfacial instabilities, transfer volumes of fluid in either direction to a greater or lesser extent, depending on turbulence in each layer.

Pure turbulent-diffusion mixing occurs when the transition layer is in a supercritical state. In this condition, violent vortex motions exchange equal volumes of fluid between layers. In reality, these two mixing processes are usually superimposed on each other, and the critical condition is dependent on local site-specific processes. By reexamining the experimental data of previous researchers including Ellison and Turner (1959), Lofquist (1960), Kato and Phillips (1969), Moore and Long (1971), Wu (1973), Chu and Vanvari

(1976), Kantha, et al., (1977), Bo Pedersen (1980), Kit, et al., (1980), Buch (1981), and Narimousa, et al., (1986), Christodoulou (1986) found that in the Richardson number range $0.01 \leq Ri_0 \leq 1$ the interface is turbulent and mixing is produced directly by eddies in the mixed layer. In the range $0.1 \leq Ri_0 \leq 10$, mixing is less turbulent and is produced by Kelvin-Helmholtz instabilities. In the range $1 \leq Ri_0 \leq 100$, where shear is weak, mixing is produced by intermittent, cusp-generated entrainment. Finally, when $Ri_0 \geq 100$, mixing is due to molecular diffusion. Mehta and Srinivas (1993) conducted experiments of fluid mud entrainment in a shear flow using a race-track flume. They observed that for $Ri_0 \leq 5$, interfacial entrainment appeared to be turbulence dominated. As Ri_0 increased above ~ 5 , the interface become convoluted with large, irregular undulations. Entrainment appeared to be dominated by interfacial wave breaking in which wisps of fluid were episodically ejected into the mixed layer.

Thus, considering the fact that at very low Richardson number, i.e., $Ri_0 \rightarrow 0$, mixing over the lutocline is dominated by turbulent diffusion, and in this situation the entrainment formula (Table 6.1) becomes inapplicable due to $m_{en} \rightarrow \infty$. The model only activates the entrainment formula when $Ri_0 \geq 1$.

6.4 Flow and Sediment Dynamics

6.4.1 Flow Field

Spring tide peak flows and slack water within the modeled domain are shown in Figures 6.2-6.5. The flow field shows the following noteworthy features:

(1) During peak flow the velocity decreases gradually from the mouth to upstream, while during slack water it decreases from upstream to the mouth.

(2) Maximum velocities occur along the channel center, in the channel segment near convex shorelines, i.e., shorelines protruding into the water area, and at other narrow sections.

(3) Near concave shorelines the velocities are lower. There mudflats are usually found [Figure 6.1(a)].

6.4.2 Tidal Variation of Velocity

Model simulated tidal velocities are shown in Figures 6.6(a)-6.9(a). The flood current was stronger than the ebb current. For example, at $0.4H$ elevation the flood peak at C2 during spring tide was around 1.70 m s^{-1} , and the ebb peak around 1.08 m s^{-1} [Figure 6.6(a)], with a ratio of 1.57. However, the peak ebb flow lasted considerably longer than the peak flood flow. From Figures 6.6(a)-6.9(a) it is found that the duration of peak ebb was around 5.34 hr, whereas that of the peak flood was around 2.05 hr, with a ratio of 2.60.

A noteworthy difference between simulations and observations is that the model under-predicted the ebb peak at C4 [Figures 6.8(a) and 6.9(a)]. To highlight this difference further, vertically-averaged maximum velocities at C2 and C4 are given in Table 6.2. It is evident that the greatest difference between simulations and observations occurred at C4 during peak ebb, with a difference of about 0.37 m s^{-1} . At C4 the measured peak ebb was greater than peak flood in contrast to other sites where flood was dominant. Table 6.2 also shows that the flood current at C2 was greater than at C4, whereas, ebb at C4 was greater

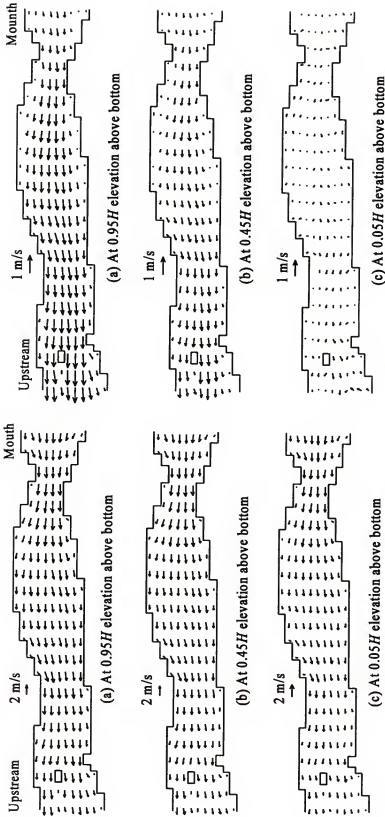


Figure 6.2. Simulated peak flood flow during a spring tide at 2000 hr, 11/05/94.

Figure 6.3. Simulated high water slack during a spring tide at 2245 hr, 11/05/94.

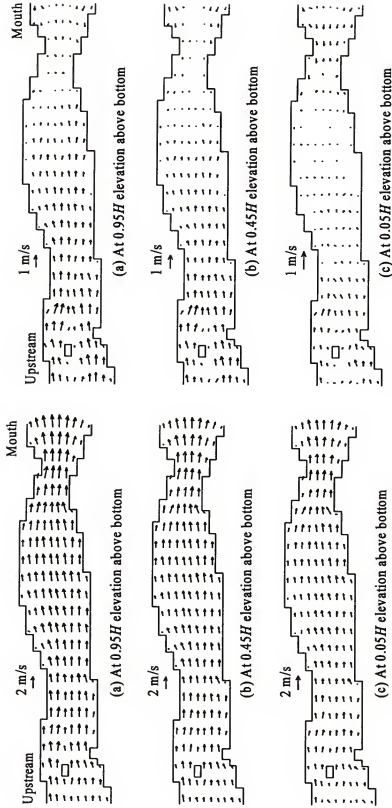


Figure 6.4. Simulated peak ebb flow during a spring tide at 0100 hr, 11/06/94.

Figure 6.5. Simulated low water slack during a spring tide at 0615 hr, 11/06/94.

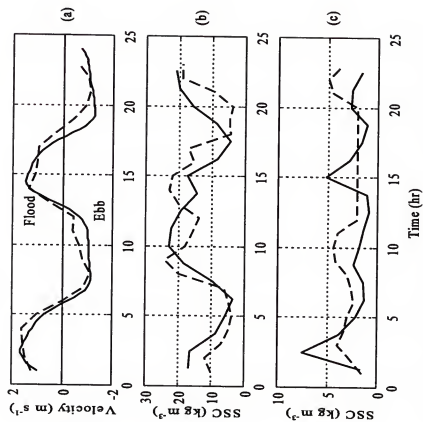


Figure 6.7. Tidal velocity at 0.4H (a), and SSC at 0.25H (b) and 0.75H (c) at C2 during a neap tide. Solid lines are simulations and dashed lines represent field data collected during 1000 hr, 11/10/94 to 0900 hr, 11/11/94.

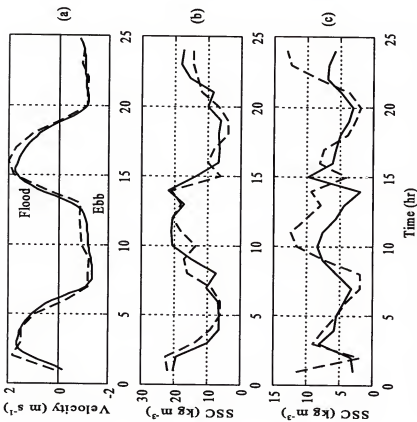


Figure 6.6. Tidal velocity at 0.4H (a), and SSC at 0.25H (b) and at 0.75H (c) at C2 during a spring tide. Solid lines are simulations and dashed lines represent field data collected during 1800 hr, 11/05/94 to 1700 hr, 11/06/94.

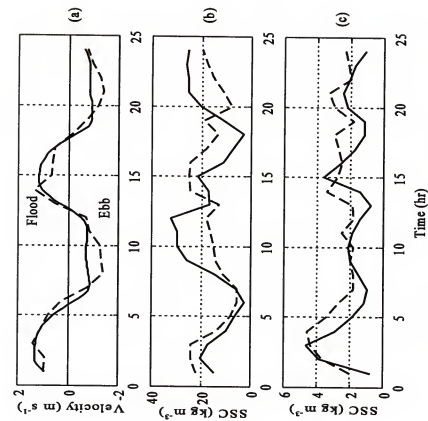


Figure 6.9. Tidal velocity at 0.4H (a), and SSC at 0.25H (b) and 0.75H (c) at C4 during a neap tide. Solid lines are simulations and dashed lines represent field data collected during 1000 hr, 11/10/94 to 0900 hr, 11/11/94.

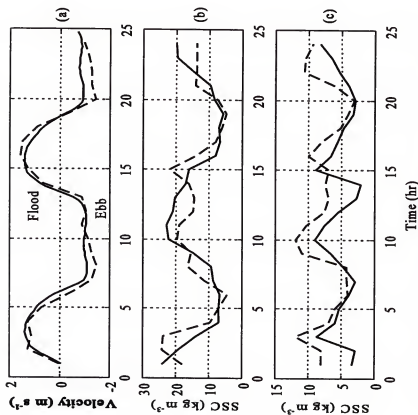


Figure 6.8. Tidal velocity at 0.4H (a), and SSC at 0.25H (b) and 0.75H (c) at C4 during a spring tide. Solid lines are simulations and dashed lines represent field data collected during 1800 hr, 11/05/94 to 1700 hr, 11/06/94.

than at C2. These observations collectively suggest that there was a horizontal circulation in the clockwise sense within the domain. This effect is discussed further in Section 6.4.4.

Table 6.2. Vertically-averaged maximum velocities at sites C2 and C4 (Unit: m s^{-1})

Site	Tide range	Observation		Simulation	
		Flood	Ebb	Flood	Ebb
C2	Spring tide	1.60	1.42	1.66	1.40
	Neap tide	1.33	0.99	1.56	1.16
C4	Spring tide	1.24	1.38	1.26	1.03
	Neap tide	1.16	1.21	1.36	0.82

6.4.3 Tidal Variation of SSC

The tidal variation of SSC near the bottom (specifically $0.25H$ above the bottom) and near the surface ($0.25H$ below the surface) are presented in Figures 6.6(b)-6.9(b) and 6.6(c)-6.9(c), respectively. The following noteworthy differences in the magnitude of SSC between simulations and observations occur:

(1) Near the bottom, the model mostly under-predicts SSC during flood and over-predicts it during ebb [Figures 6.6(b)-6.9(b)].

(2) Near the surface the model mostly under-predicts SSC over the entire tidal cycle [Figures 6.6(c)-6.9(c)].

Tidal variations of SSC show the following characteristics:

(1) Variations of SSC with Tidal Range: SSC exhibits quantitatively the same behavioral pattern during spring and neap tides. However, near the bottom, SSC during

spring tide is less than at neap [Figures 6.6(b)-6.9(b)], being usually $10\text{-}20\text{ kg m}^{-3}$ during spring and $10\text{-}25\text{ kg m}^{-3}$ during neap. In contrast, near the surface, SSC during spring is greater than during neap [Figures 6.6(c)-6.9(c)], being usually $5\text{-}10\text{ kg m}^{-3}$ during spring and $2\text{-}5\text{ kg m}^{-3}$ during neap.

(2) Vertical Variations of SSC: As might be expected, SSC near the bottom was always greater than near the surface. Near the bottom it was seldom less than 10 kg m^{-3} [Figures 6.6(b)-6.9(b)], whereas, near the surface it was seldom greater than 10 kg m^{-3} [Figures 6.6(c)-6.9(c)].

(3) Variations of SSC during Flood and Ebb: During high water slack, "low" SSC, which is defined here as the value at the "trough" of SSC tidal variation, occurred both near the bottom and the surface, with a lag of 0.5-1 hr near the surface. During low water slack peak SSC, which is defined in an analogous way as the value at the crest of SSC tidal variation, occurred near the bottom whereas low SSC occurred near the surface. During peak ebb, peak SSC occurred over the entire water column. During peak flood, peak SSC occurred near the surface whereas low SSC occurred near the bottom.

The behavior of SSC reflects cumulative effects on SSC due to flocculation, tidal current asymmetry (with a stronger flood peak and a weaker, longer duration of ebb peak), entrainment of the lutocline, turbulence damping in the fluid mud layer and the large ratio of tidal range to mean water depth.

During slack water, due to comparatively low vertical turbulent diffusion over the water column, higher turbulence damping in the fluid mud layer and decreasing mixing over the lutocline, sediment tends to settle and concentrate near the bottom where, as a result, high SSC occurs in the hindered settling range. As a further result, peak SSC occurs near the bottom and low SSC near the surface, along with a thick fluid mud layer and a stable lutocline (Odd and Rodger, 1986; Wolanski, et al., 1988). This was the situation during slack water in the Jiaojiang with the exception of the condition near the bottom during high water slack. It is believed that the large ratio of the tidal range to the water depth causes this latter phenomenon. As stated in Section 4.1, the mean tidal range in the studied domain was about 4 m and the mean water depth (below MSL) about 4-7 m with a ratio of about 0.8 between tidal range and water depth. Thus, during flood the water depth increased dramatically. This increase plus advection of lower SSC water from the region beyond the modeled domain caused the SSC near the bottom to be diluted. As shown in Figure 6.10, the vertically-averaged SSC at C1 during flood was always less than that at C2 and C4, with a difference of about $4-13 \text{ kg m}^{-3}$, which accounts for about 50%-85% of the vertically-averaged values of SSC at C2 and C4. It is this difference plus the large ratio of tidal range to water depth that causes dilution during flood. It also implies that sediment transport seems to be influenced strongly by advection.

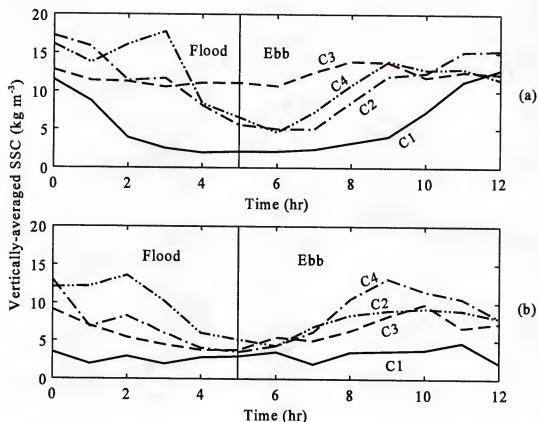


Figure 6.10. Time series of vertically-averaged SSC during a spring tide (a) and a neap tide (b). During spring tide, the data at sites C1 and C3 began at 1700 hr, 11/04/94 and at sites C2 and C4 at 1800 hr, 11/05/94. During neap tide, the data at sites C1 and C3 began at 1000 hr, 11/12/94 and at sites C2 and C4 at 2300 hr, 11/10/94.

During peak current, due to significant vertical turbulent diffusion and strong upward mixing over the lutocline (caused by internal wave breaking and high rate of erosion of freshly deposited sediment during the previous slack), SSC over the water column usually increases, the elevation of lutocline layer rises, and both fluid mud and lutocline layers become comparatively thicker (Odd and Rodger, 1986; Wolanski, et al., 1988). In the Jiaojiang, as noted, although the ebb peak is weaker than flood, it lasts longer than flood. As

a result, during peak ebb, diffusion, vertical mixing over the lutocline and bottom erosion are also comparatively high. Consequently, both during peak ebb and peak flood, SSC exhibits quantitatively the same behavior as noted, except near the bottom during peak flood due to the cumulative effects of dilution, stronger entrainment over the lutocline and mixing within the fluid mud layer.

6.4.4 Vertical Profiles of Velocity

Typical vertical profiles of velocity over a tidal cycle are shown in Figures 6.11-6.14. Many of the simulated velocity profiles are in reasonable agreement with the observations, although the simulations for spring tide show better agreement than at neap. It is also observed that at peak flood, the velocity over the entire water column was greater than that at peak ebb. Flood peak near the bottom ranges $0.8-1.0 \text{ m s}^{-1}$ at spring tide and $0.5-0.8 \text{ m s}^{-1}$ at neap. Ebb peak near the bottom ranges $0.6-0.8 \text{ m s}^{-1}$ at spring tide and $0.4-0.65 \text{ m s}^{-1}$ at neap.

Noteworthy differences between simulations and observations are as follows: during the flood at neap tide, the model over-predicted some profiles near the bottom, e.g., at 2 hr and 3 hr in Figures 6.12 and 6.14, respectively. During ebb, the model over-predicted some profiles near the surface at C2, e.g., at 8 hr and 9 hr in Figure 6.12 and under-predicted some profiles near the surface at C4, e.g., at 9 hr and 10 hr in Figure 6.14. These differences between simulations and observations are perhaps caused by following factors:

- (1) Use of Approximate Stratification Function: The stratification function [Eq. (3.10)] used in the model can be expected to affect the bottom drag coefficient, C_D [Eq. (3.9)

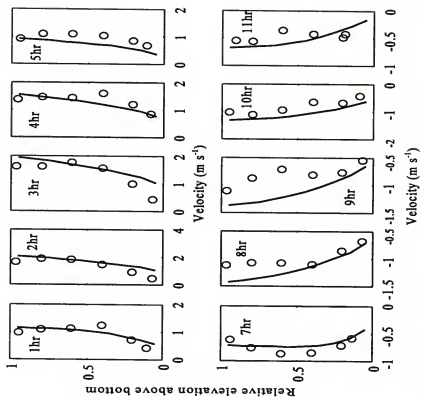


Figure 6.11. Velocity profiles at site C2 during a spring tide. Solid lines are simulations and open circles represent data obtained during 1900 hr, 11/05/94 to 0600 hr, 11/06/94. Positive values signify flood and negative denote ebb.

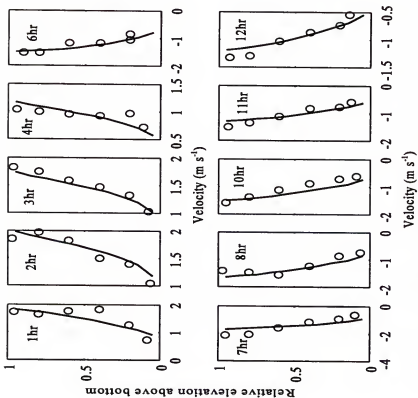


Figure 6.12. Velocity profiles at site C2 during a neap tide. Solid lines are simulations and open circles represent data obtained during 1100 hr to 2100 hr, 11/10/94. Positive values signify flood and negative denote ebb.

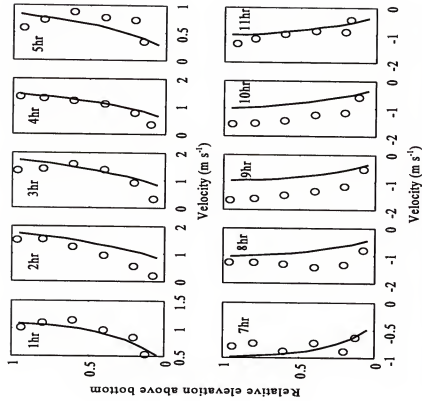


Figure 6.13. Velocity profiles at site C4 during a spring tide. Solid lines are simulations and open circles represent data obtained during 1900 hr, 11/05/94 to 0500 hr, 11/06/94. Positive values signify flood and negative denote ebb.

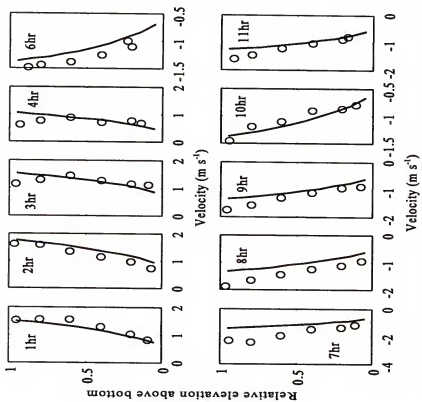


Figure 6.14. Velocity profiles at site C4 during a neap tide. Solid lines are simulations and open circles represent data obtained during 1100 hr to 2100 hr, 11/10/94. Positive values signify flood and negative denote ebb.

and Table 6.1], and consequently the near-bottom velocity near the bottom. As a result, an over-prediction of the stratification effect can imply reduced C_D and enhanced velocity near the bottom.

(2) Coriolis Effect: The model omitted the Coriolis effect due to the high Rossby number within the modeled domain, $R_o = U/f\bar{B} \approx 12.0 \gg 1$, where the Coriolis parameter $f = 2\Omega \sin\phi_l = 7.29 \times 10^{-5} \text{ s}^{-1}$, the angular velocity of the earth's rotation $\Omega = 7.29 \times 10^{-5} \text{ s}^{-1}$, the latitude $\phi_l = 30^\circ$, the characteristic mean velocity $U = 1.0 \text{ m s}^{-1}$ and the mean width of the estuary $\bar{B} = 1.2 \text{ km}$ (Section 4.1). Note that R_o signifies the effect of flow inertia relative to Coriolis acceleration. Thus, a high R_o implies comparatively low Coriolis effect. Note however, that Taizhou Bay outside the estuary (Figure 4.1) is a much wider water body with a mean width of about 6 km and R_o of about 2.0. Thus, one may expect that Coriolis acceleration would have a greater effect on the tidal current in the bay, which in turn perhaps has an effect on the tidal currents within the estuary. However, in that context the following analysis should be noted.

To examine the Coriolis effect further, the work of Proudman (1925) is introduced here. Proudman calculated the vertically-averaged transverse and longitudinal tidal currents, V and U , across a channel under the Coriolis effect for the special case of $f = \omega_n$, the angular frequency of the n^{th} tidal constituent, which corresponds to the diurnal tide, S_2 , at latitude 30° . A parabolic section is assumed for the channel as

$$h = h_0 \left(1 - \left(\frac{y}{\bar{B}} \right)^2 \right) \quad (6.1)$$

where h is the mean water depth below MSL, h_0 is the maximum water depth at the channel center and y is the transverse Cartesian coordinate originating from the channel center. The relevant formulas are as follows:

Non-dimensional transverse current:

$$\frac{\omega_n}{gh_0} hV = \frac{e^{k\bar{B}}}{2k^2\bar{B}^2} \left\{ \left[1 + \frac{2\omega_n^2\bar{B}^2}{gh_0} - k^2(\bar{B}^2 - y^2) - k(\bar{B} - y) \right] \sinh k(\bar{B} + y) + [k^2(\bar{B}^2 - y^2) - k(\bar{B} + y)] \cosh k(\bar{B} + y) \right\} \quad (6.2)$$

Non-dimensional longitudinal current:

$$\frac{\omega_n}{gh_0} hU = \frac{e^{k\bar{B}}}{2k^2\bar{B}^2} \left\{ \left[1 + \frac{2\omega_n^2\bar{B}^2}{gh_0} + k^2(\bar{B}^2 - y^2) - k(\bar{B} - y) \right] \sinh k(\bar{B} + y) - [k^2(\bar{B}^2 - y^2) + k(\bar{B} + y)] \cosh k(\bar{B} + y) \right\} \quad (6.3)$$

with the tidal wave number $k = \omega_n / \sqrt{g\bar{h}}$, where \bar{h} is the mean water depth of the parabolic flow cross-section, i.e., $\bar{h} = 2h_0/3$. Figure 6.15 shows the distributions of the transverse and longitudinal currents across channel in the Jiaojiang and also Taizhou Bay. $h_0 = 5$ m and $\omega_n = 7.27 \times 10^{-5}$ rad s⁻¹ (diurnal tide) were taken both for the estuary and the bay, and $\bar{B} = 1.2$ km and 6 km were taken in the estuary and the bay, respectively. It is observed that even in

the Taizhou Bay the Coriolis effect is almost negligible. The circulation in the bay due to this effect will rotate in the counterclockwise sense. This will lead to a clockwise circulation within the estuary due to the vorticity transfer by shear, consistent with the sense of rotation observed (Section 6.4.2).

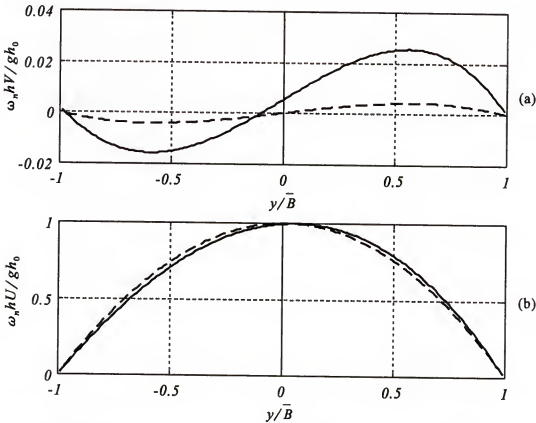


Figure 6.15. Distributions of transverse (a) and longitudinal (b) currents across the channel due to the Coriolis effect, viewed in the direction of tidal wave propagation. Solid lines are currents in Taizhou Bay and dashed lines in the Jiaojiang.

(3) Gravitational Circulation due to Salinity: Previous observations in the Jiaojiang have showed that salinity is typically well-mixed vertically during the entire tidal cycle (Zhou, 1986; Li, et al., 1993; Dong, et al., 1997). Hence, salinity-induced transport was not

considered in the present modeling effort. However, based on their simulations of salinity distribution in the Jiaojiang with and without sediment-induced buoyancy effects, Guan, et al. (1998) observed that suspended sediment could measurably modify the vertical distribution of salinity due to the fact that suspended sediment causes the currents to be strongly sheared along the vertical direction. They predicted that under sediment-induced buoyancy effects, salinity stratification locally increased during flood tide, thus in turn modifying the vertical profile of velocity.

Gravitational circulation due to salinity stratification can be approximately expressed in a formulation including river inflow and surface wind stress as follows (Hansen and Rattray, 1965):

$$\frac{u_g}{U_f} = \frac{3}{2}(1-\sigma^2) + \frac{T}{4}(1+4\sigma+3\sigma^2) + \frac{\alpha_g Ra}{48}(1-9\sigma^2-8\sigma^3) \quad (6.4)$$

where the first term on the right hand side is due to the effect of river inflow, the second term is due to the effect of wind, the third term is due to salinity-induced density gradient, u_g is the gravitational circulation and U_f is the vertical-mean inflow velocity. Further, T is the dimensionless wind stress, equal to $2\overline{BH}^2|\tau_w|/\rho A_v R_f$, R_f is the river inflow rate, Ra is the estuarine Rayleigh number, defined as the ratio of free convection to diffusion (Hansen and Rattray, 1965), i.e., equal to $gk_s S_0 H^3/\rho A_v A_x$, k_s is a proportionality coefficient between fluid density and salinity ($\approx 0.78 \times 10^{-3}$), S_0 is the salinity at the mouth of the estuary, and α_g is a constant in the relationship of salinity distribution introduced as follows

$$\frac{s(x, \sigma)}{S_0} = \alpha_g X + Z(\sigma) \quad (6.5)$$

Here X is the dimensionless horizontal coordinate, i.e., $X = R\gamma/\bar{B}HA_x$, and Z is the vertical distribution function of salinity.

Figure 6.16 shows profiles of u_g for different $\alpha_g Ra$ without considering the effect of surface wind stress. This type of gravitational circulation can cause ebb current to increase near the surface and decrease near the bottom, and vice versa during flood. The observations at C4 (Figure 6.13 and 14) were characteristically consistent with this trend. It should be noted that in light of the likely interaction between salinity and SSC in the Jiaojiang, Hansen and Rattray's analysis based on salinity effect alone must be interpreted more broadly for this estuary with regard to the likely combined effects of the salinity and SSC in inducing the gravitational circulation shown in Figure 6.16

(4) Geomorphologic Effects: Due to non-linear effects of bottom friction and of advection, tidal residual currents usually exist in the vicinity of topographies such as basins, headlands, sand ridges, etc. (Zimmerman, 1981). Noteworthy features in the Jiaojiang are the headlands located at the mouth of Taizhou Bay (Figure 4.1). It is likely that tidal residual currents induced by these headlands have effects on the residual currents within the estuary itself. As shown in Figure 6.17 (Zimmerman, 1981), along a coastal promontory tidal flow tends to accelerate as well as decelerate, with a maximum near the headland. Concurrently, a frictional boundary layer develops with diminishing current velocity towards the coast. Thus, vorticity is generated along the coast with orientation alternating between the flood and

ebb. As the vorticity is largest near the headland, during flood there is a net flux of counterclockwise vorticity into the left closed curve and out of the right one. During the ebb the situation does not reverse because of a net flux of clockwise vorticity out of the left quadrilateral and into the right quadrilateral, which is equivalent to the situation during the flood. Hence there is a net flux of counterclockwise vorticity into the left quadrilateral and of clockwise vorticity into the right quadrilateral, giving rise to a vortex pair of opposite signs at either sides of the headland. In other words, residual circulation exists at both sides of the headland.

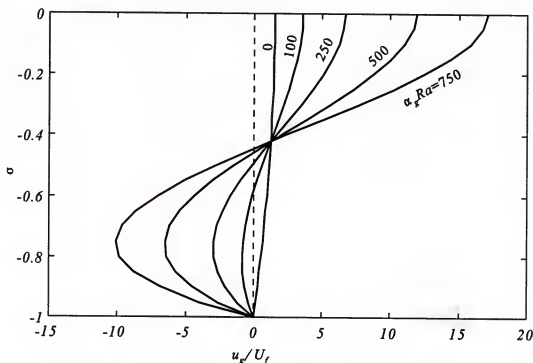


Figure 6.16. Profiles of gravitational circulation without wind stress, after Hansen and Rattray (1965).

Thus, a clockwise circulation can be expected in the north region of Taizhou Bay and a counterclockwise one in its southern region. These circulations possibly have extended effects on residual currents within the Jiaojiang. Unfortunately, Taizhou Bay is beyond the modeled domain, and there are no observations available to back-up this assertion.

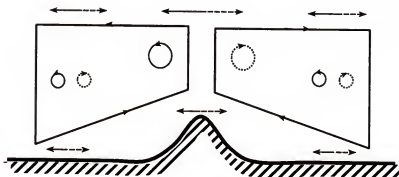


Figure 6.17. Tidal currents, vorticities and residual circulation in the neighborhood of a headland. Currents are signified by solid arrows for flood and dashed arrows for ebb. Currents are largest near the headland and decrease towards the shoreline. Vorticity therefore has a maximum near the headland. Vorticities generated by side-wall friction are shown by solid circles for flood and dashed circles for ebb. Vorticities have highest strength near the headland and diminish away from it (after Zimmerman, 1981).

6.4.5 Vertical Profiles of SSC

Figures 6.18-6.21 show vertical profiles of SSC simulated and observed at sites C2 and C4 over one tidal cycle during spring and neap tides, respectively. The following features of these SSC profiles are noteworthy:

(1) SSC changes in the following way: near the bottom during ebb, SSC continues to increase until flow deceleration occurs, then decreases. During flood it either continues to decrease, or increases somewhat during the accelerating phase of flow, then decreases.

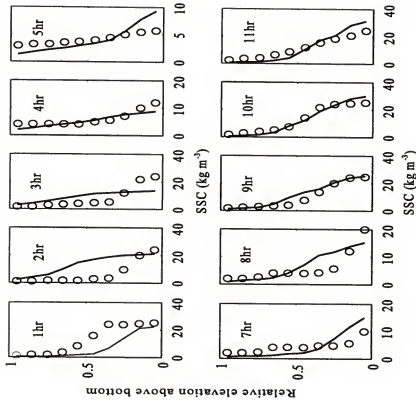


Figure 6.19. SSC profiles at site C2 during a neap tide. Solid lines are simulations and open circles represent field data obtained during 1100 hr to 2100 hr, 11/10/94.

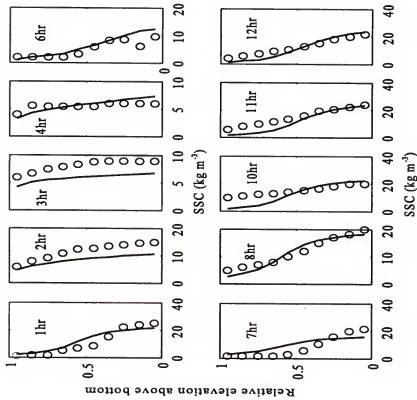


Figure 6.18. SSC profiles at site C2 during a spring tide. Solid lines are simulations and open circles represent field data obtained during 1900 hr, 11/05/94 to 0600 hr, 11/06/94.

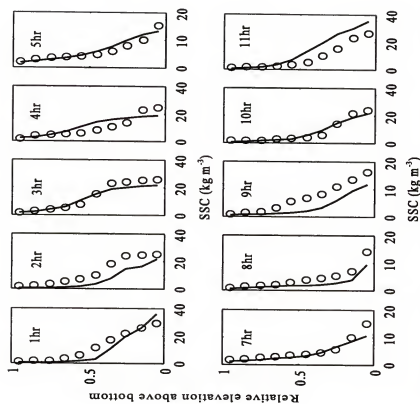


Figure 6.21. SSC profiles at site C4 during a neap tide. Solid lines are simulations and open circles represent field data obtained during 1100 hr to 2100 hr, 11/10/94.

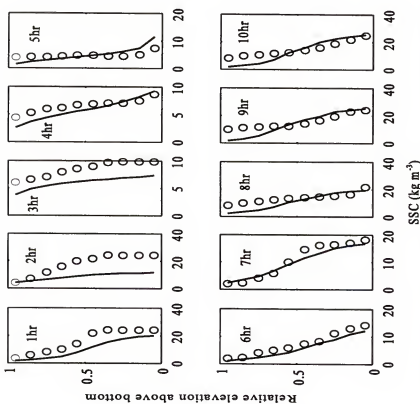


Figure 6.20. SSC profiles at site C4 during a spring tide. Solid lines are simulations and open circles represent field data obtained during 1900 hr, 11/05/94 to 0400 hr, 11/06/94.

Near the surface, it increases during accelerating flow and decreases during the decelerating flow both for flood and ebb.

(2) During peak currents, the lutocline layer (defined in Section 2.1) rises and becomes thicker, with gentler upper and lower gradients. During slack water it falls and becomes thinner, with steeper upper and lower gradients.

(3) The lutocline layer is lower and thinner during neap tide than during spring.

(4) Fluid mud and lutocline layers occur over the entire tidal cycle except during the period around high water slack.

This behavior of SSC reflects the cumulative effects of flocc settling, tidal asymmetry, lutocline entrainment, turbulence damping in fluid mud layer and the large ratio of tidal range to water depth (see also Section 6.4.3).

Differences between the simulations and observations of SSC are as follows: during ebb tide, the model over-predicts SSC for some profiles near the bottom, e.g., 5 hr, 7 hr and 11 hr in Figure 6.19, and under-predicts near the surface, e.g., 10 hr and 11 hr in Figure 6.18 and 8 hr, 9 hr and 10 hr in Figure 6.20. During flood tide, the model under-predicts SSC in some profiles over the entire water column, e.g., 2 hr and 3 hr in Figures 6.18 and 6.20, respectively. These differences likely arise due to following modeling approximations as well as observation errors:

(1) Approximate Open Boundary Conditions for SSC: SSC at the open boundaries were measured 30 hr before and after those at sites C2 and C4 during spring and neap tides, respectively, and were taken as uniform over the cross-sections of the open boundaries (see also in Section 6.3.3).

In order to demonstrate the lateral non-uniformity of SSC in the Jiaojiang, model simulations and observations of vertically-averaged SSC at the flow section including sites C2 and C4 are plotted in Figure 6.22. From this figure together with the tidal variation of velocity [Figures 6.6.6(a)-6.9(a)], it is found that during flood, SSC at C4 was greater than at C2, and during ebb it gradually increased at C2 and ultimately became greater than at C4. A difference (in the vertically-averaged SSC) of about 0.7 kg m^{-3} occurred between C2 and C4, which accounts for about 0%-70% of the vertically-averaged values of SSC at these sites. Because uniform SSC over the cross-sections of the open boundaries were employed in modeling, the model generated a more uniform SSC across the estuary within the modeled domain than observations (Figure 6.22). Table 6.3 includes typical values from Figure 6.22 at 4 hr, where two exhibit significant SSC non-uniformity and the other two do not. It is evident that better comparisons of vertically-averaged SSC between simulations and observations resulted at times of comparatively minor non-uniformity than when significant lateral non-uniformity occurred.

Table 6.3. Vertically-averaged SSC during minor and significant non-uniformity of SSC across the flow cross-section (Unit: kg m^{-3})

Method	Site	Minor non-uniformity				Significant non-uniformity			
		Spring tide		Neap tide		Spring tide		Neap tide	
		5 hr	10 hr	5 hr	8 hr	2 hr	15 hr	2 hr	10 hr
Observation	C2	5.50	12.50	4.00	6.00	11.50	6.75	6.75	13.20
	C4	6.50	12.90	6.00	7.00	16.25	14.00	12.10	9.00
Simulation	C2	5.70	13.25	4.00	7.00	11.50	10.75	13.50	12.50
	C4	5.70	15.00	3.60	7.50	9.50	11.75	14.00	15.50

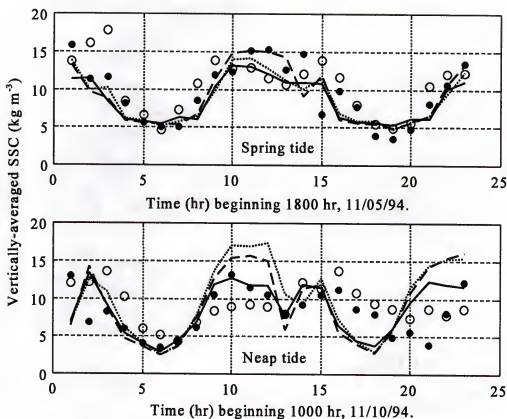


Figure 6.22. Time series of vertically-averaged SSC. Dark circles are from site C2, open circles represent site C4, solid lines signify simulations at C2, dashed lines are simulations at the center of the flow section containing C2 and C4 and dotted lines denote simulations at C4.

In order to demonstrate the significance of SSC non-uniformity, a model test using non-uniform boundary conditions for SSC was carried out for a spring tide. The simulated results are shown in Figure 6.23. Also shown in this figure are results using uniform SSC boundary conditions (Figure 6.22). Non-uniform SSC at the boundaries was generated using a linear relationship as follows: (1) the mean value of SSC over each open boundary was taken as the observation at site C1 or C3; (2) the slope of the lateral variation of SSC was taken as the ratio of vertically-averaged SSC observed between sites C2 and C4 (Figure

6.22). From Figure 6.23, it is observed that considerable differences in the simulated SSC were generated during peak ebb. This suggests, at least qualitatively, that non-uniformity of SSC at the open boundaries may have had a noteworthy effect on simulations within the estuary.

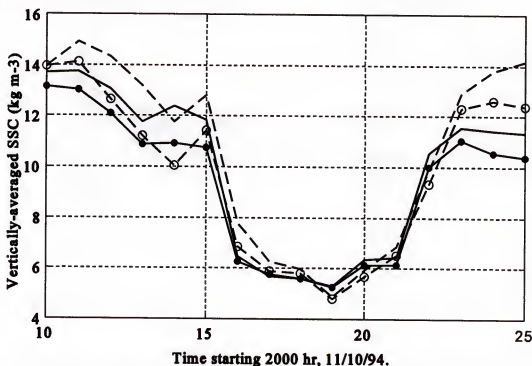


Figure 6.23. Comparison of simulated vertically-averaged SSC using uniform and nonuniform boundary conditions of SSC during a spring tide. Solid lines signify simulations at site C2, dashed lines are that at site C4 and dark and open circles represent that using uniform boundary conditions of SSC.

(2) Approximate Parameters: The selection of modeling parameters given in Table 6.1 was a difficult task. Although most parameters were determined optimally from previous works, data analysis and model calibration, parametric selection can in general cause

measurable differences between simulations and observations due to the approximate nature of the parameters. Noted in the following are those parameters that are sediment-dependent and highly influential in controlling the sensitivity of the simulations of SSC:

Parameters Determined by Model Calibrations: Model calibrations were carried out based on comparisons of SSC between simulations and observations. Because all parameters affected each other on an inter-dependent way in the calibration tests, it was at times difficult to identify the desired value of a certain parameter. In this regard, the most noteworthy ones are: the efficiency coefficient of turbulence damping, d_2 , in the vertical mass diffusion equation (3.20) (see also in Table 6.1), ω_{sc1} , ω_{sc2} , c_{s1} , c_{s2} , c_p , m_i and n_i in the consolidation rate formula (2.23) (see also in Table 6.1) and \bar{C} , α_2 , β_2 and h_b in the vertical distribution formula (2.24) of dry sediment concentration for a fully-consolidated bed (Table 6.1). There were no direct experimental data available for determining these parameters for the Jiaojiang.

Bottom Erosion Rate Constant: The bottom erosion rate constant, M_{max} , was obtained from analysis of field data (Section 4.3.6 and Table 6.1). Data analysis was carried out based on three basic assumptions (Section 4.3.6). It is known that the second and third assumptions seem reasonable but the first may not be so. As stated in Section 6.4.3, advection is a major factor affecting sediment transport in the Jiaojiang, and consequently has a significant effect on SSC. Thus it can not be ignored. In fact, the scatter of data points in Figure 4.29 demonstrates the effect of advection. Thus, the correct erosion rate constant can only be determined through erosion experiments in laboratory using the same mud as in the Jiaojiang.

(3) Observation Errors: As noted in Chapter 4, a ship-borne turbidimeter was used for measuring the SSC. The ship was anchored by a mooring chain with a length $\approx 10H \approx 50$ m. Thus, the ship could turn along with tidal currents and change its orientation within the circle defined by the chain. Given the laterally non-uniform distribution of SSC in the Jiaojiang as described above and in Section 6.4.3, changing ship position could have led to a degree of error in the observed SSC.

6.4.6 Lutocline Layer

The lutocline layer was identified by its definition in Section 2.1, i.e., the near-bottom layer between the upper elevation and lower elevation of the maximum vertical gradient of SSC (Figure 2.1). Figure 6.24 shows typical vertical distributions of the vertical gradient of SSC. The lutocline layer is identified by the zone over which the SSC gradient is comparatively high.

Time variations of this layer, both simulated and observed at sites C2 and C4 during spring and neap tides, are shown in Figures 6.24-6.27. It is seen that both the measured pattern and elevation of the lutocline layer are reproduced approximately by the model. Except for periods of about 1-2 hr around high water slack, a lutocline layer with a thickness of about 1-3 m (Figure 6.29) and an upper elevation of 1-4 m (Figure 6.30) consistently occurred, irrespective of whether the tide was spring or neap.

From Figures 6.25-6.28 and Table 6.4, combined with Figures 6.6(a)-6.9(a), the following characteristics of the lutocline layer can be gleaned:

(1) The lutocline layer was at higher elevation during peak flows than during slack water, with the highest elevations during peak floods.

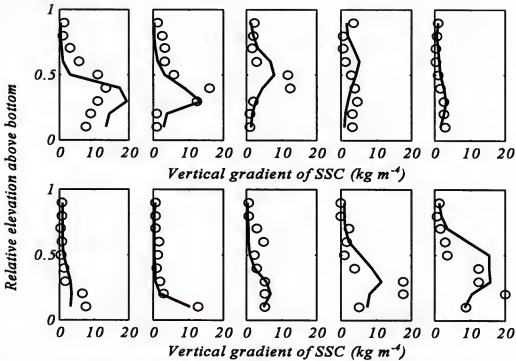


Figure 6.24. Vertical gradient of SSC as a function of elevation during a neap tide. Solid lines are simulations and open circles represent field data obtained during 1100 hr to 2100 hr, 11/10/94.

(2) The lutocline layer was thinner during slack water than during peak flow, and also thinner during neap tide than during spring.

(3) The lutocline layer rose during period of flow acceleration and fell during flow decelerating periods.

From comparisons of the thickness of the lutocline layer between simulations and measurements (Figure 6.29), it is observed that the predicted thickness of the lutocline layer is in better agreement with measurement at neap tide than at spring (Figure 6.29). Also, there is a degree of over-prediction of its upper limit at neap tide and under-prediction at spring (Figure 6.30).

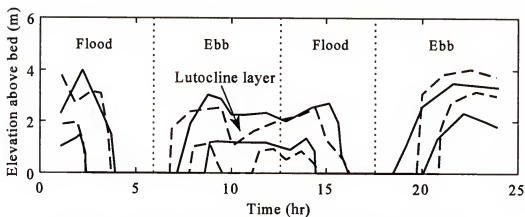


Figure 6.24. Simulated (solid lines) and measured (dashed lines) tidal variation of the lutocline layer at site C2 during a spring tide from 1800 hr, 11/05/94 to 1700 hr, 11/06/94.

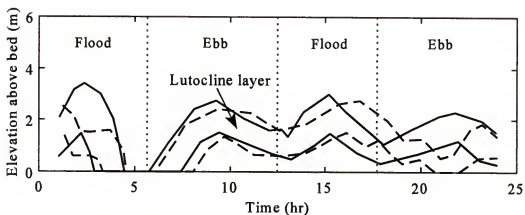


Figure 6.25. Simulated (solid lines) and measured (dashed lines) tidal variation of the lutocline layer at site C2 during a neap tide from 1000 hr, 11/10/94 to 0900 hr, 11/11/94.

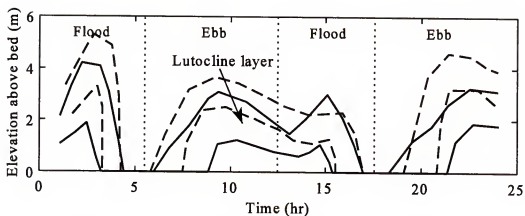


Figure 6.26. Simulated (solid lines) and measured (dashed lines) tidal variation of the lutocline layer at site C4 during a spring tide from 1800 hr, 11/05/94 to 1700 hr, 11/06/94.

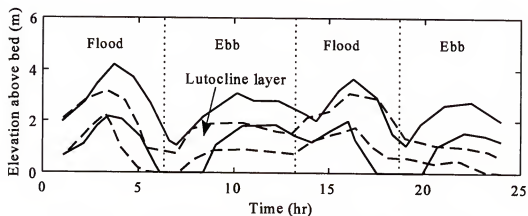


Figure 6.27. Simulated (solid lines) and measured (dashed lines) tidal variation of the lutocline layer at site C4 during a neap tide from 1000 hr, 11/10/94 to 0900 hr, 11/11/94.

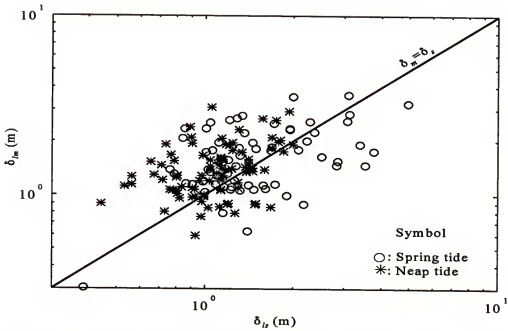


Figure 6.28. Lutocline layer thickness: simulation (δ_{ls}) and measurement (δ_{lm}).

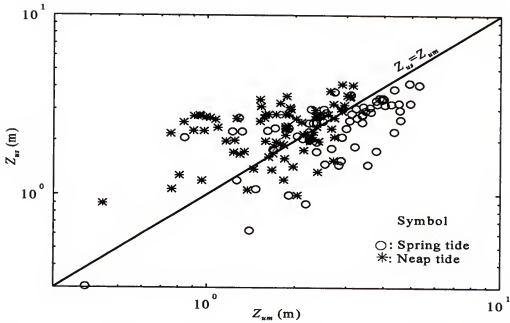


Figure 6.29. Lutocline layer upper elevation: simulation (Z_{um}) and measurement (Z_{us}).

Table 6.4. Average thickness and upper elevation of lutocline layer at different times (Unit: m)

Item	Tidal range	Observation				Simulation			
		Spring tide		Neap tide		Spring tide		Neap tide	
		C2	C4	C2	C4	C2	C4	C2	C4
Lutocline layer thickness	Peak flood	1.83	1.61	1.17	1.02	1.98	1.83	1.46	1.42
	Peak ebb	1.46	1.54	1.10	1.02	1.61	1.24	1.10	1.17
	High slack	0.00	0.00	0.58	0.88	0.00	0.00	0.44	1.02
	Low slack	1.32	1.17	1.02	0.80	1.17	1.02	1.02	0.88
	Tidal mean	1.27	1.30	0.97	0.97	1.29	1.43	0.99	1.33
Upper elevation of lutocline layer	Peak flood	3.07	3.80	2.63	3.07	3.29	3.59	3.15	3.50
	Peak ebb	3.15	3.80	1.98	1.54	3.15	3.07	2.34	2.56
	High slack	0.00	0.00	1.10	1.17	0.00	0.00	0.59	1.17
	Low slack	1.90	2.20	1.61	1.61	2.05	1.76	1.61	2.05
	Tidal mean	2.41	3.31	1.64	1.80	2.44	2.41	2.09	2.51

6.4.7 Flow-SSC Hysteresis

Due to time-lag effects associated with settling, diffusion, bed erosion, entrainment and consolidation, SSC in estuaries is usually higher during decreasing currents than when currents are increasing (Postma, 1967; Dyer and Evans, 1989). As a result, when the SSC at a certain elevation is plotted against the bottom shear stress, this hysteresis becomes visually evident (Costa and Mehta, 1990).

Simulated and measured hysteresis loops of SSC for sites C2 and C4 are shown in Figures 6.31-6.38. These are at 1 m above the bottom and 1 m below the instantaneous surface during spring and neap tides.

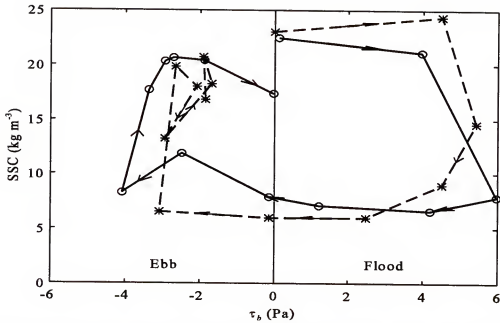


Figure 6.30. Simulated (solid line) and measured (dashed line) hysteresis loops at 1 m above bottom at C2 during a spring tide from 1800 hr, 11/05/94 to 0500 hr, 11/06/94.

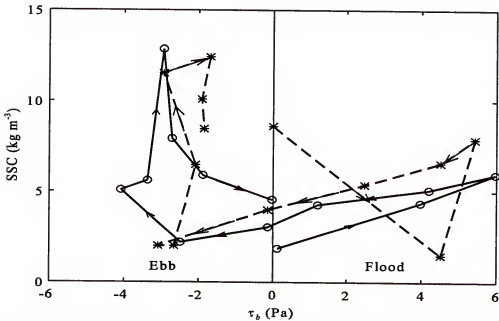


Figure 6.31. Simulated (solid line) and measured (dashed line) hysteresis loops at 1 m below surface at C2 during a spring tide from 1800 hr, 11/05/94 to 0500 hr, 11/06/94.

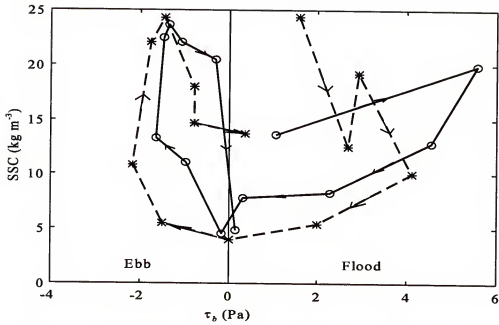


Figure 6.32. Simulated (solid line) and measured (dashed line) hysteresis loops at 1 m above bottom at C2 during a neap tide from 1000 hr to 2100 hr, 11/10/94.

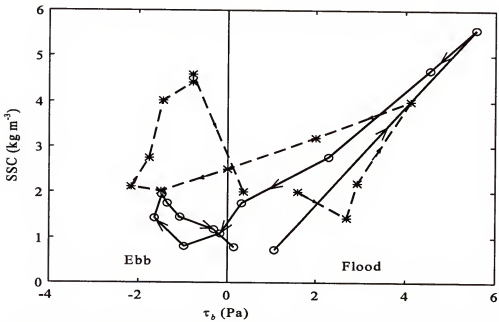


Figure 6.33. Simulated (solid line) and measured (dashed line) hysteresis loops at 1 m below surface at C2 during a neap tide from 1000 hr to 2100 hr, 11/10/94.

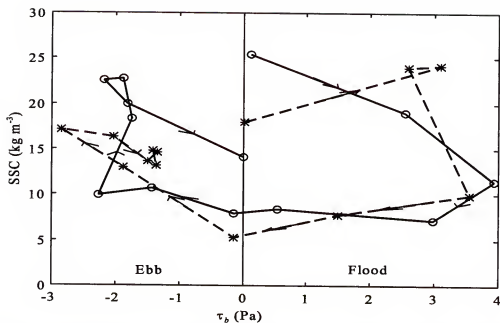


Figure 6.34. Simulated (solid line) and measured (dashed line) hysteresis loops at 1 m above bottom at C4 during a spring tide from 1800 hr, 11/05/94 to 0500 hr, 11/06/94.

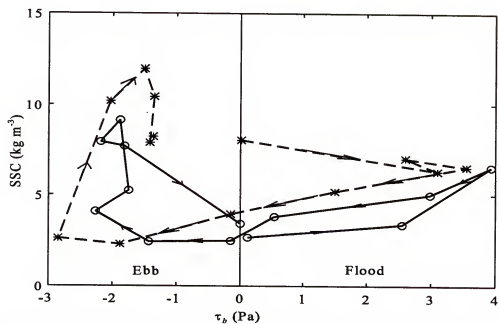


Figure 6.35. Simulated (solid line) and measured (dashed line) hysteresis loops at 1 m below surface at C4 during a spring tide from 1800 hr, 11/05/94 to 0500 hr, 11/06/94.

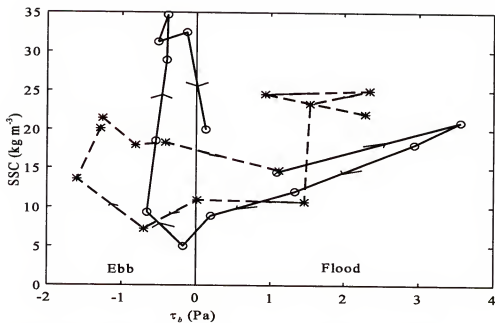


Figure 6.36. Simulated (solid line) and measured (dashed line) hysteresis loops at 1 m above bottom at C4 during a neap tide from 1000 hr to 2100 hr, 11/10/94.

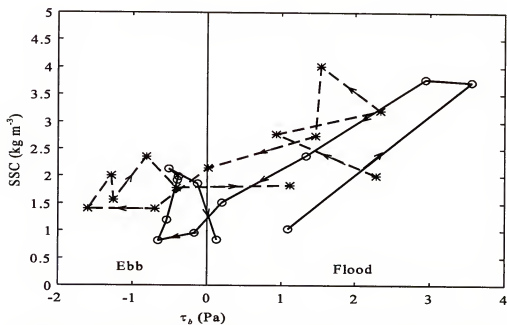


Figure 6.37. Simulated (solid line) and measured (dashed line) hysteresis loops at 1 m below surface at C4 during a neap tide from 1000 hr to 2100 hr, 11/10/94.

During ebb (Figures 6.31-6.38), the simulated and measured loops near the bottom and near the surface follow the same trend. During accelerating flow SSC increases gradually (by resuspension). As the flow begins to decelerate, at first SSC increases dramatically until it reaches a maximum, then starts to decrease (due to deposition). This behavior results in the loops rotation in the clockwise sense.

During flood, the loops near the bottom and near the surface follow different patterns. Near the bottom (Figures 6.31, 6.33, 6.35 and 6.37), SSC either decreases over all stages, or increases somewhat during accelerating flow, then decreases. This causes the loops to rotate clockwise. Near the surface (Figures 6.32, 6.34, 6.36 and 6.38), SSC increases during accelerating flows due to vertical diffusion and mixing and reaches a maximum at the end of the period of acceleration. Subsequently, during decelerating flows, SSC begins to decrease due to settling and dilution. This causes the loops rotating in the counterclockwise sense.

Thus, during flood, loop-reversals appeared near the bottom in the Jiaojiang. Costa and Mehta (1990) observed such loop-reversals in Hangzhou Bay, China, during the transition from accelerating to decelerating flow. They showed that reversal was induced by the presence of the lutocline at that level. During accelerating flow the lutocline forms, and entrainment over it occurs concurrently. Due to the entrainment lag, SSC near the bottom increases and reaches a maximum during accelerating flow, then decreases. This leads to a loop-reversal.

In the Jiaojiang, more significant loop-reversals occurred near the bottom during the entire flood tide period (Figures 6.31, 6.33, 6.35 and 6.37) with the SSC either decreasing

over this period, or increasing somewhat during accelerating flow, then decreasing. As noted in section 6.4.3, this behavior is believed to be caused by the effects of dilution, vertical diffusion as well as the presence of the lutocline.

6.4.8 Effect of Turbulence Damping on SSC and Lutocline Formation

With reference to Section 6.4.3, in order to further examine the effect of turbulence damping on SSC and the lutocline formation, the following numerical tests were carried out:

- (1) Test 1: Considering turbulence damping and taking $d_2=0.75$;
- (2) Test 2: Neglecting turbulence damping, i.e., taking $d_2=0$;
- (3) Test 3: Neglecting the effects of cohesion and interactions between flocs, i.e., taking $Ri_B=Ri_\mu=0$ and $d_2=0.75$.

In the above tests, all other parameters were taken to be the same as in previous simulations. Figure 6.39 shows the results of these tests along with the observations at C4 during a neap tide. It is seen that without considering turbulence damping (Test 2), the model resulted in relatively uniform profiles of SSC and consequently less distinct lutoclines (2-5 hrs and 9-11 hrs in Figure 6.39). If compared with the observations, it is seen that Test 2 had the worst results, Test 1 had the best with Test 3 in-between. However, there were smaller differences among these tests during low slack water (1 hr in Figure 6.39) and high slack water (7 and 8 hrs in Figure 6.39). This implies that during high and low slack waters, the lutocline is mainly governed by floc settling. It is also seen that considerable effect of turbulence damping appeared near the bottom (2-5 hrs and 9-11 hrs in Figure 6.39), because of damping induced by the relatively high SSC there. Near the surface, the effect of damping

during flood (2-5 hrs in Figure 6.39) is greater than during ebb (9-11 hrs in Figure 6.39), due to the relatively higher SSC near the surface during flood. Without considering cohesion and interactions between flocs (Test 3), the simulated results are very close to Test 1 and the differences are mainly near the bottom. This supports the conclusion in Chapter 5 that cohesion and interactions between flocs govern turbulence damping only at high SSC ($>40-50 \text{ kg m}^{-3}$), in the hindered settling range.

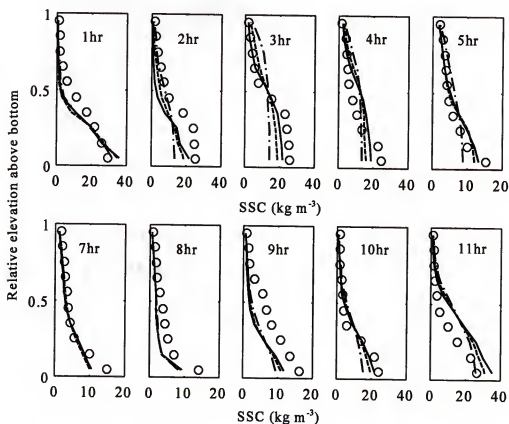


Figure 6.39. Modeling SSC profiles at site C4 during a neap tide. Open circles represent field data from 1100 hr to 2100 hr, 11/10/94, solid lines are simulations with $d_2=0.75$, dashed lines signify simulations with $d_2=0.75$ and $Ri_B=0$, and dotted lines represent simulations with $d_2=0$.

CHAPTER 7 SUMMARY AND CONCLUSIONS

7.1 Summary

Lutoclines are common features in estuaries with high-load fine sediments. They are significantly associated with interfacial waves and turbulence damping in fluid mud, and tend to diminish vertical mixing under tidal forcing. In order to better understand these dynamical features, the following studies were carried out:

1. Turbulence Damping: Following Rossby and Montgomery (1935), assuming the sum of the kinetic, potential and dissipated energy in a stratified, cohesive flow to be equal to that in a homogeneous, non-cohesive flow at identical shear rates, turbulence damping in fluid mud was phenomenologically examined. Accordingly, sediment settling flux, cohesion, interactions between flocs and sediment-induced stratification were quantified by the respective Richardson numbers Ri_ω , Ri_B , Ri_μ and Ri . The resulting formulations for the turbulent mixing length were examined using observations in the Jiaojiang estuary. The corresponding expressions for the vertical momentum and mass diffusion coefficients were incorporated in the developed numerical model codes for flow and sediment transport.

2. Internal Waves: ASSM data from the Jiaojiang estuary were used to examine the height, angular frequency, celerity and length of internal waves at the lutocline. Their

variation with the global Richardson number was examined in the light of results of previous studies on the lutocline and other pycnoclines.

3. Lutocline Response to Tidal Forcing: Three-dimensional, finite-difference hydrodynamic and sediment transport codes, COHYD-UF and COSED-UF, were developed, incorporating the latest unit process models for fine sediment transport including erosion/entrainment, diffusion, settling, deposition and consolidation. Following model testing against analytical solutions, laboratory data and field observations, tidal lutocline dynamics was examined by applications of COHYD-UF and COSED-UF and comparisons with field observations on flow and sediment transport from the Jiaojiang.

7.2 Conclusions

Important conclusions drawn from this study are as follows:

1. It is shown that turbulence damping in the water column at high SSC is governed by the settling flux in the flocculation settling range, and by cohesion and interaction between flocs in the hindered settling range. Maximum turbulence damping is shown to occur at the lutocline, supporting a similar, but qualitative observation (e.g., Ross and Mehta, 1989). Data derived from the Jiaojiang estuary are shown to support this observation.

2. Numerical model tests using SSC data from the Jiaojiang showed that without considering turbulence damping, the simulated results of SSC become less tenable when compared with the field observations, resulting in comparatively more uniform profiles of SSC and less distinct lutoclines than observed.

3. Observations in the Jiaojiang showed that the lutocline strength was highly associated with turbulence energy. The lutocline became comparatively less distinct as the turbulent energy production $F_s > \sim 0.0003 \text{ m}^2 \text{ s}^{-3}$. This supports the qualitative conclusion from the derived expression of turbulence damping.

4. High and low frequency internal waves were detected at the lutocline in the Jiaojiang. The shallow water low frequency wave had a representative rms height of 0.38 m and a modal frequency of 0.09 rad s^{-1} , which was near the local Brunt-Väisälä frequency. The deep water high frequency wave was characterized by sharp crests and flat troughs, with a rms height of 0.21 m and a modal frequency of 1.33 rad s^{-1} . This wave was possibly induced by interfacial shear at the lutocline.

5. The height and the angular frequency of both high and low frequency waves decreased with increasing Richardson number. The height and angular frequency versus $\log Ri_0$ plots exhibited linear trends and, in turn, the celerity and wave length increased with increasing Richardson number.

6. Numerical modeling tests showed that the developed codes, COHYD-UF and COSED-UF, are able to adequately simulate transport processes including sediment propagation, advection, diffusion, entrainment and consolidation. The simulated results compare reasonably with laboratory and field observations, once the appropriate process-related parameters are adopted.

7. From the simulations and observations in the Jiaojiang estuary, the lutocline was found to behave as follows: (1) The lutocline elevation was higher during peak flows than

during slack water, with the highest elevations during peak floods; (2) the lutocline layer was thinner during slack water than during peak flows, and also thinner during neap tide than spring; (3) the lutocline layer rose during flow acceleration and fell during flow decelerating periods; and (4) the lutocline was observed to persist through most of the tidal cycle, except 1-2 hr around high water. The overall behavior of lutocline reflects the cumulative effects of tidal current asymmetry (with a stronger flood peak and a weaker, longer duration of ebb peak), sediment settling and entrainment, turbulence damping and also the large ratio of tidal range to mean water depth resulting in a dilution effect during flood.

7.3 Recommendations for Future Studies

The present study is based on the limited data from the Jiaojiang. There persists a lack of quantitative information on internal wave generation, propagation, interfacial instability and vertical mixing at the lutocline. The only observations used to verify the derived analytical model of mixing length in the sediment-stratified water column were the results obtained from the vertical excursion of SSC using ASSM signals.

In the sub-model for sediment erosion, it was assumed that the existence of fluid mud has no tangible effect on bottom erosion. However, in general fluid mud appears as a “protective” cover over the bottom and thereby bottom erosion.

Based on the conclusions of this study, the following recommendations are made for future research:

1. In order to fully understand the internal wave behavior, collecting long time series of continuous *in situ* records of the interface are essential.

2. Direct measurement of turbulent mixing in the fluid mud is necessary to verify the mixing length model.

3. Extensive experiments in flumes are required for understanding the way in which the fluid mud layer affects bottom erosion.

APPENDIX A
DERIVATIONS OF THE GOVERNING EQUATIONS

A.1 Vertical Velocities, w and ω , and Continuity Equation (3.1)

The σ -transform converts the time and Cartesian coordinate system (t, x, y, z) to the new time and coordinate system (t', x', y', σ) according to

$$\begin{cases} t' = t \\ x' = x \\ y' = y \\ \sigma = \frac{z - \zeta}{H} \end{cases} \quad (\text{A.1})$$

The vertical velocity in the σ -coordinate, ω , is defined as

$$\omega = \frac{D\sigma}{Dt} \quad (\text{A.2})$$

The vertical velocity in the z -coordinate, w , is

$$\begin{aligned} w &= \frac{Dz}{Dt} = H \frac{D\sigma}{Dt} + \sigma \frac{DH}{Dt} + \frac{D\zeta}{Dt} \\ &= H\omega + \left(\sigma \frac{\partial H}{\partial t'} + \frac{\partial \zeta}{\partial t'} \right) + u \left(\sigma \frac{\partial H}{\partial x'} + \frac{\partial \zeta}{\partial x'} \right) + v \left(\sigma \frac{\partial H}{\partial y'} + \frac{\partial \zeta}{\partial y'} \right) \end{aligned} \quad (\text{A.3})$$

The continuity equation is

$$\frac{\partial u}{\partial x} + \frac{\partial v}{\partial y} + \frac{\partial w}{\partial z} = 0 \quad (\text{A.4})$$

The transformation of each term in Eq. (A.4) is as follows

The first term:

$$\frac{\partial u}{\partial x} = \frac{\partial u}{\partial x'} \frac{\partial x'}{\partial x} + \frac{\partial u}{\partial \sigma} \frac{\partial \sigma}{\partial x} = \frac{\partial u}{\partial x'} - \frac{\partial u}{\partial \sigma} \left(\frac{\sigma}{H} \frac{\partial H}{\partial x'} + \frac{1}{H} \frac{\partial \zeta}{\partial x'} \right) \quad (\text{A.5})$$

The second term:

$$\frac{\partial v}{\partial y} = \frac{\partial v}{\partial y'} \frac{\partial y'}{\partial y} + \frac{\partial v}{\partial \sigma} \frac{\partial \sigma}{\partial y} = \frac{\partial v}{\partial y'} - \frac{\partial v}{\partial \sigma} \left(\frac{\sigma}{H} \frac{\partial H}{\partial y'} + \frac{1}{H} \frac{\partial \zeta}{\partial y'} \right) \quad (\text{A.6})$$

The third term:

$$\frac{\partial w}{\partial z} = \frac{\partial w}{\partial \sigma} \frac{\partial \sigma}{\partial z} = \frac{1}{H} \frac{\partial w}{\partial \sigma} \quad (\text{A.7})$$

Differentiating Eq. (A.3) with respect to σ , one obtains

$$\frac{\partial w}{\partial \sigma} = H \frac{\partial \omega}{\partial \sigma} + \frac{\partial u}{\partial \sigma} \left(\sigma \frac{\partial H}{\partial x'} + \frac{\partial \zeta}{\partial x'} \right) + u \frac{\partial H}{\partial x'} + \frac{\partial v}{\partial \sigma} \left(\sigma \frac{\partial H}{\partial y'} + \frac{\partial \zeta}{\partial y'} \right) + v \frac{\partial H}{\partial y'} + \frac{\partial H}{\partial t'} \quad (\text{A.8})$$

Substituting Eqs. (A.5)-(A.8) into Eq. (A.4), simplifying and eliminating the superscript (prime) for convenience, one obtains

$$\frac{\partial \zeta}{\partial t} + \frac{\partial u H}{\partial x} + \frac{\partial v H}{\partial y} + H \frac{\partial \omega}{\partial \sigma} = 0 \quad (\text{A.9})$$

Integrating Eq. (A.9) with σ from -1 to 0 and considering the facts that $\omega|_{\sigma=0} = \omega|_{\sigma=-1} = 0$, the continuity equation (3.1) becomes

$$\frac{\partial \zeta}{\partial t} + \int_{-1}^0 \left(\frac{\partial H u}{\partial x} + \frac{\partial H v}{\partial y} \right) d\sigma = 0 \quad (\text{A.10})$$

A.2 Momentum Equations (3.2) and (3.3)

The derivation of the momentum Equation (3.2) in the x -direction is given here. The derivation of equation (3.3) in the y -direction is analogous. The momentum equation in the x -direction is

$$\frac{\partial u}{\partial t} + u \frac{\partial u}{\partial x} + v \frac{\partial u}{\partial y} + w \frac{\partial u}{\partial z} - fv = -\frac{1}{\rho} \frac{\partial p}{\partial x} + \left(A_x \frac{\partial^2 u}{\partial x^2} + A_y \frac{\partial^2 u}{\partial y^2} \right) + \frac{\partial}{\partial z} \left(A_v \frac{\partial u}{\partial z} \right) + \frac{1}{\rho} \frac{\partial \tau_B}{\partial z} \frac{u}{\sqrt{u^2 + v^2}} \quad (\text{A.11})$$

Here the rheological effect (the last term on the right hand side) of fluid mud is simply considered by assuming that its rheological behavior satisfies the Bingham model (Odd and Cooper, 1989).

The σ -transform of terms on the left hand side of Eq. (A.11) is

The first term:

$$\frac{\partial u}{\partial t} = \frac{\partial u}{\partial t'} + \frac{\partial u}{\partial \sigma} \frac{\partial \sigma}{\partial t} = \frac{\partial u}{\partial t'} - \frac{\partial u}{\partial \sigma} \left(\frac{\sigma}{H} \frac{\partial H}{\partial t'} + \frac{1}{H} \frac{\partial \zeta}{\partial t'} \right) \quad (\text{A.12})$$

The third term:

$$\frac{\partial u}{\partial y} = \frac{\partial u}{\partial y'} + \frac{\partial u}{\partial \sigma} \frac{\partial \sigma}{\partial y} = \frac{\partial u}{\partial y'} - \frac{\partial u}{\partial \sigma} \left(\frac{\sigma}{H} \frac{\partial H}{\partial y'} + \frac{1}{H} \frac{\partial \zeta}{\partial y'} \right) \quad (\text{A.13})$$

The fourth term:

$$\frac{\partial u}{\partial z} = \frac{\partial u}{\partial \sigma} \frac{\partial \sigma}{\partial z} = \frac{1}{H} \frac{\partial u}{\partial \sigma} \quad (\text{A.14})$$

Assuming pressure to be hydrostatic, the pressure term in right side of Eq. (A.11) becomes

$$-\frac{1}{\rho} \frac{\partial p}{\partial x} = -\frac{1}{\rho} \frac{\partial}{\partial x} \left(g \int_z^{\zeta} \rho dz \right) = -g \frac{\rho_{\zeta}}{\rho} \frac{\partial \zeta}{\partial x} - \frac{g}{\rho} \int_z^{\zeta} \frac{\partial \rho}{\partial x} dz \quad (\text{A.15})$$

where ρ_ζ is the fluid density at the water surface. Thus the σ -transform of the pressure term

is

$$\begin{aligned}
 -\frac{1}{\rho} \frac{\partial p}{\partial x} &= -\frac{g\rho_\zeta}{\rho} \left(\frac{\partial \zeta}{\partial x'} \frac{\partial x'}{\partial x} + \frac{\partial \zeta}{\partial \sigma} \frac{\partial \sigma}{\partial x'} \right) - g \int_{\sigma}^0 \left[\frac{\partial \rho}{\partial x'} - \frac{\partial \rho}{\partial \sigma} \left(\frac{\sigma}{H} \frac{\partial H}{\partial x'} + \frac{1}{H} \frac{\partial \zeta}{\partial x'} \right) \right] H d\sigma \\
 &= -\frac{g\rho_\zeta}{\rho} \frac{\partial \zeta}{\partial x'} - \frac{gH}{\rho} \int_{\sigma}^0 \frac{\partial \rho}{\partial x'} d\sigma + \frac{g}{\rho} \frac{\partial \zeta}{\partial x'} \int_{\sigma}^0 \frac{\partial \rho}{\partial \sigma} d\sigma + \frac{g}{\rho} \frac{\partial H}{\partial x'} \int_{\sigma}^0 \sigma \frac{\partial \rho}{\partial \sigma} d\sigma \\
 &= -g \frac{\partial \zeta}{\partial x'} - \frac{gH}{\rho} \int_{\sigma}^0 \frac{\partial \rho}{\partial x'} d\sigma - \frac{g}{\rho} \frac{\partial H}{\partial x'} \left(\sigma \rho + \int_{\sigma}^0 \rho d\sigma \right)
 \end{aligned} \tag{A.16}$$

The transformation of the turbulent diffusion term in the x -direction is

$$\begin{aligned}
 \frac{\partial^2 u}{\partial x^2} &= \frac{\partial}{\partial x} \left[\frac{\partial u}{\partial x'} - \frac{\partial u}{\partial \sigma} \left(\frac{\sigma}{H} \frac{\partial H}{\partial x'} + \frac{1}{H} \frac{\partial \zeta}{\partial x'} \right) \right] \\
 &= \frac{\partial^2 u}{\partial x'^2} + \text{Higher Order Terms} \approx \frac{\partial^2 u}{\partial x'^2}
 \end{aligned} \tag{A.17}$$

Similar to Eq. (A.17), the turbulent diffusion term in the y -direction is

$$\frac{\partial^2 u}{\partial y^2} = \frac{\partial^2 u}{\partial y'^2} + \text{Higher Order Terms} \approx \frac{\partial^2 u}{\partial y'^2} \tag{A.18}$$

The turbulent diffusion term in the vertical direction has the form

$$\frac{\partial}{\partial z} \left(A_v \frac{\partial u}{\partial z} \right) = \frac{1}{H} \frac{\partial}{\partial \sigma} \left(\frac{A_v}{H} \frac{\partial u}{\partial \sigma} \right) \tag{A.19}$$

Substituting Eqs. (A.3), (A.5) and (A.12)-(A.19) into Eq. (A.11), simplifying and eliminating the superscript (prime) for convenience, the momentum equation (3.2) in the x -

direction is obtained as

$$\begin{aligned} \frac{\partial u}{\partial t} + u \frac{\partial u}{\partial x} + v \frac{\partial u}{\partial y} + \omega \frac{\partial u}{\partial \sigma} - f v = -g \frac{\partial \zeta}{\partial x} - \frac{gH}{\rho} \int_{\sigma}^0 \frac{\partial \rho}{\partial x} d\sigma \\ - \frac{g}{\rho} \frac{\partial H}{\partial x} \left(\sigma \rho + \int_{\sigma}^0 \rho d\sigma \right) + \left(A_x \frac{\partial^2 u}{\partial x^2} + A_y \frac{\partial^2 u}{\partial y^2} \right) + \frac{1}{H} \frac{\partial}{\partial \sigma} \left(\frac{A_v}{H} \frac{\partial u}{\partial \sigma} \right) + \frac{1}{\rho H} \frac{\partial \tau_B}{\partial \sigma} \frac{u}{\sqrt{u^2 + v^2}} \end{aligned} \quad (\text{A.20})$$

A.3 Sediment Conservation Equation (3.15)

The sediment conservation equation is

$$\frac{\partial c}{\partial t} + u \frac{\partial c}{\partial x} + v \frac{\partial c}{\partial y} + w \frac{\partial c}{\partial z} - \frac{\partial \omega_z c}{\partial z} = \left(K_x \frac{\partial^2 c}{\partial x^2} + K_y \frac{\partial^2 c}{\partial y^2} \right) + \frac{\partial}{\partial z} \left(K_v \frac{\partial c}{\partial z} \right) \quad (\text{A.21})$$

Similar to Eq. (A.20), the following forms are obtained:

The first term on the left hand side (LHS):

$$\frac{\partial c}{\partial t} = \frac{\partial c}{\partial t'} \frac{\partial t'}{\partial t} + \frac{\partial c}{\partial \sigma} \frac{\partial \sigma}{\partial t} = \frac{\partial c}{\partial t'} - \frac{\partial c}{\partial \sigma} \left(\frac{\sigma}{H} \frac{\partial H}{\partial t'} + \frac{1}{H} \frac{\partial \zeta}{\partial t'} \right) \quad (\text{A.22})$$

The second term on the LHS:

$$\frac{\partial c}{\partial x} = \frac{\partial c}{\partial x'} \frac{\partial x'}{\partial x} + \frac{\partial c}{\partial \sigma} \frac{\partial \sigma}{\partial x} = \frac{\partial c}{\partial x'} - \frac{\partial c}{\partial \sigma} \left(\frac{\sigma}{H} \frac{\partial H}{\partial x'} + \frac{1}{H} \frac{\partial \zeta}{\partial x'} \right) \quad (\text{A.23})$$

The third term on the LHS:

$$\frac{\partial c}{\partial y} = \frac{\partial c}{\partial y'} \frac{\partial y'}{\partial y} + \frac{\partial c}{\partial \sigma} \frac{\partial \sigma}{\partial y} = \frac{\partial c}{\partial y'} - \frac{\partial c}{\partial \sigma} \left(\frac{\sigma}{H} \frac{\partial H}{\partial y'} + \frac{1}{H} \frac{\partial \zeta}{\partial y'} \right) \quad (\text{A.24})$$

The fourth term on the LHS

$$\frac{\partial c}{\partial z} = \frac{\partial c}{\partial \sigma} \frac{\partial \sigma}{\partial z} = \frac{1}{H} \frac{\partial c}{\partial \sigma} \quad (\text{A.25})$$

The fifth term on the LHS:

$$\frac{\partial \omega_z c}{\partial z} = \frac{1}{H} \frac{\partial \omega_z c}{\partial \sigma} \quad (\text{A.26})$$

The first term on right hand side (RHS):

$$\frac{\partial^2 c}{\partial x^2} = \frac{\partial^2 c}{\partial x'^2} + \text{Higher Order Terms} = \frac{\partial^2 c}{\partial x'^2} \quad (\text{A.27})$$

The second term on the RHS:

$$\frac{\partial^2 c}{\partial y^2} = \frac{\partial^2 c}{\partial y'^2} + \text{Higher Order Terms} = \frac{\partial^2 c}{\partial y'^2} \quad (\text{A.28})$$

The third term on the RHS:

$$\frac{\partial}{\partial z} \left(K_v \frac{\partial c}{\partial z} \right) = \frac{1}{H} \frac{\partial}{\partial \sigma} \left(\frac{K_v}{H} \frac{\partial c}{\partial \sigma} \right) \quad (\text{A.29})$$

Substituting Eqs. (A.22)-(A.29) into Eq. (A.21), simplifying and eliminating the superscript (prime) for convenience, the sediment conservation equation (3.15) becomes

$$\frac{\partial c}{\partial t} + u \frac{\partial c}{\partial x} + v \frac{\partial c}{\partial y} + \omega \frac{\partial c}{\partial \sigma} - \frac{1}{H} \frac{\partial \omega_z c}{\partial \sigma} = \left(K_x \frac{\partial^2 c}{\partial x^2} + K_y \frac{\partial^2 c}{\partial y^2} \right) + \frac{1}{H} \frac{\partial}{\partial \sigma} \left(\frac{K_v}{H} \frac{\partial c}{\partial \sigma} \right) \quad (\text{A.30})$$

APPENDIX B
NUMERICAL TECHNIQUES

B.1 Back-Tracing Approach

In the Eulerian-Lagrangian differential scheme, the physical properties of water particles at time step n are obtained by the back-tracing approach (Casulli and Cheng, 1992). The back-tracing time interval $\Delta t'' = \Delta t / N_p$. At each back-tracing step m , the water particle will lag by small distances

$$dx^m = -u_b^n \frac{\Delta t''}{\Delta x}, \quad dy^m = -v_b^n \frac{\Delta t''}{\Delta y}, \quad d\sigma^m = -\omega_b^n \frac{\Delta t''}{\Delta \sigma} \quad (\text{B.1})$$

where dx^m , dy^m and $d\sigma^m$ are the backward distances at time step m in the x , y and σ directions, respectively, and u_b^n , v_b^n and ω_b^n are the local velocities of the water particle in the x , y and σ directions, respectively, that are approximated by bilinear interpolation over the eight surrounding mesh points. Finally, the water particle is traced back to the position p , using back-tracing distances dx , dy and $d\sigma$ given by (Figure B.1)

$$dx = \sum_{m=1}^{N_p} dx^m, \quad dy = \sum_{m=1}^{N_p} dy^m, \quad d\sigma = \sum_{m=1}^{N_p} d\sigma^m \quad (\text{B.2})$$

Then, the physical property at point p is obtained by bilinear interpolation as follows

$$G_p^n = (1-d\sigma) \left[(1-dx)(1-dy)G_1^n + (1-dx)dyG_2^n + dx(1-dy)G_3^n + dx dy G_4^n \right] \\ + d\sigma \left[(1-dx)(1-dy)G_5^n + (1-dx)dyG_6^n + dx(1-dy)G_7^n + dx dy G_8^n \right] \quad (\text{B.3})$$

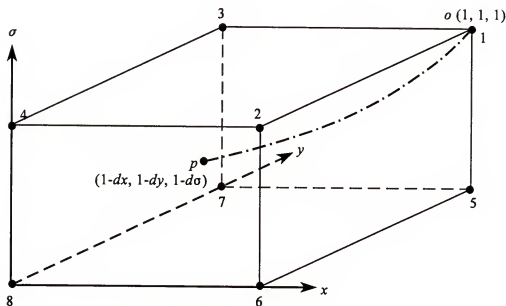


Figure B.1. Schematic diagram of back-tracing approach, where dotted line is the pathline of water particle, o is the position of water particle at current time step $n+1$ and p is the position of water particle at the previous time step n .

B.2 Pre-conditioned Conjugate Gradient Method

The linear five-diagonal system of equations for the water surface elevation, ζ , can be written in the following general form

$$\zeta_{i,j} - a_{i+1/2,j} \zeta_{i+1,j} - a_{i-1/2,j} \zeta_{i-1,j} - a_{i,j+1/2} \zeta_{i,j+1} - a_{i,j-1/2} \zeta_{i,j-1} = b_{i,j} \quad (\text{B.4})$$

where $a_{i\pm 1/2,j}$, $a_{i,j\pm 1/2}$ and $b_{i,j}$ are coefficients that are dependent on the time step. Note that for notational simplicity, superscript $(n+1)$ of water surface elevation, ζ , has been omitted. Note also that the coefficients $a_{i\pm 1/2,j}$ and $a_{i,j\pm 1/2}$ are non-negative and their sum is strictly less than unity. Thus the system formed by these equations is normalized, symmetric and positive-definite (Casulli and Cheng, 1992).

The pre-conditioned conjugate gradient algorithm to solve the system of equations (B.4) takes the following steps (Bertolazzi, 1990):

$$(B.2.1) \text{ Guess } \zeta_{i,j}^{(0)}.$$

$$(B.2.2) \text{ Set } p_{i,j}^{(0)} = r_{i,j}^{(0)} = \zeta_{i,j}^{(0)} - a_{i+1/2,j} \zeta_{i+1,j}^{(0)} - a_{i-1/2,j} \zeta_{i-1,j}^{(0)} - a_{i,j+1/2} \zeta_{i,j+1}^{(0)} - a_{i,j-1/2} \zeta_{i,j-1}^{(0)} - b_{i,j}.$$

(B.2.3) Carry out following calculations for $k=0, 1, 2, \dots$ and until $(\vec{r}^{(k)}, \vec{r}^{(k)}) < \epsilon$

$$\left\{ \begin{array}{l} \zeta_{i,j}^{(k+1)} = \zeta_{i,j}^{(k)} - \alpha^{(k)} p_{i,j}^{(k)} \\ r_{i,j}^{(k+1)} = r_{i,j}^{(k)} - \alpha^{(k)} (M p_{i,j}^{(k)}) \\ p_{i,j}^{(k+1)} = r_{i,j}^{(k+1)} + \beta^{(k)} p_{i,j}^{(k)} \\ \alpha^{(k)} = \frac{(\vec{r}^{(k)}, \vec{r}^{(k)})}{(\vec{p}^{(k)}, M \vec{p}^{(k)})} \\ \beta^{(k)} = \frac{(\vec{r}^{(k+1)}, \vec{r}^{(k+1)})}{(\vec{r}^{(k)}, \vec{r}^{(k)})} \\ M p_{i,j}^{(k)} = p_{i,j}^{(k)} - a_{i+1/2,j} p_{i+1,j}^{(k)} - a_{i-1/2,j} p_{i-1,j}^{(k)} - a_{i,j+1/2} p_{i,j+1}^{(k)} - a_{i,j-1/2} p_{i,j-1}^{(k)} - b_{i,j} \end{array} \right. \quad (B.5)$$

where ϵ is the allowed error. At each iteration the essential calculations consist of a matrix-vector multiplication $\vec{M}\vec{p}^{(k)}$ as specified in Eq. (B.5), two scalar products between vectors, namely $(\vec{r}^{(k)}, \vec{r}^{(k)})$ and $(\vec{p}^{(k)}, \vec{M}\vec{p}^{(k)})$ and three sums between vectors, namely $\vec{\zeta}^{(k)} - \alpha\vec{p}^{(k)}$, $\vec{r}^{(k)} - \alpha\vec{M}\vec{p}^{(k)}$ and $\vec{r}^{(k)} + \beta\vec{p}^{(k)}$.

APPENDIX C
EFFECT OF TEMPERATURE ON SETTLING VELOCITY

The experimental results of Lau (1994) related to temperature effect on the deposition of cohesive sediments in an annular flume indicated that temperature affects the settling velocity not only through changes in the viscosity and density of water, but also through floc aggregation. The flocs become stronger and denser with decrease of temperature, and consequently their settling velocity increases. To examine this effect, Lau's data are reprocessed here. His experiments were carried out at different temperatures and under the same flow condition with bottom shear stress $\tau_b=0.2$ Pa and initial vertical mean SSC, $C_0=9$ kg m⁻³. The available data are the concentration-time curves for runs at various temperatures. Commercial kaolinite was used in the experiments. Figure C.1 shows the frequency distribution, ϕ_j , of the settling velocity based on the standard size distribution of a similar kaolinite (Yeh, 1979), where the settling velocity is calculated from the Stokes law

$$\omega_{0n} = \frac{g d_n^2}{18\nu} \left(\frac{\rho_s}{\rho_0} - 1 \right) \quad (C.1)$$

In Eq. (C.1), d_n and ω_{0n} , respectively, are the grain size and settling velocity of the n^{th} kaolinite class, and $\rho_s=2,650$ kg m³, $\rho_0=1,000$ kg m³ and $\nu=10^{-6}$ m² s⁻¹.

In accordance with the method of Mehta and Lott (1987), sorting by size characteristically occurs for non-uniform fine sediment. Given $C(t)$ as the instantaneous depth-averaged concentration, under a given depositional flow condition C will decrease with time and ultimately reach a steady state value, C_f . If τ_{d1} and τ_{dM} are respectively defined as the minimum and maximum critical shear stress for deposition of the M_k kaolinite classes, then when $\tau_b > \tau_{dM}$, no sediment can deposit, whereas when $\tau_b < \tau_{d1}$, all sediment eventually deposits. When $\tau_{d1} < \tau_b < \tau_{dM}$, a certain fraction of the initial sediment, represented by C_f , will ultimately remain in suspension, and the remainder, represented by $C_0 - C_f$ will settle out. The occurrence of C_f less than C_0 but greater than zero is an indication of sediment sorting. A deposition law for a non-uniform cohesive sediment was developed by Mehta and Lott (1987) based on the consideration that the instantaneous concentration, C , is obtained by summation of the corresponding concentrations, C_n , obtained from the deposition relationship of Krone (1962) for each class. This leads to

$$\frac{C(t)}{C_0} = \frac{1}{C_0} \sum_{n=1}^{M_s} C_n(t) = \sum_{n=1}^{M_s} \phi_j(\omega_{sn}) \exp \left\{ - \left[1 - \frac{\tau_b}{\tau_{d1}} \left(\frac{\omega_{s1}}{\omega_{sn}} \right) \left[\frac{\ln(\tau_{dM}/\tau_{d1})}{\ln(\omega_{sM}/\omega_{s1})} \right] \right] \frac{\omega_{sn}}{H} \right\} \quad (C.2)$$

where ω_{sn} is the settling velocity of the n^{th} kaolinite class, which is simplified as

$$\omega_{sn} = F_c \omega_{0n} \quad (C.3)$$

where ω_{s1} and ω_{sM} are respectively the minimum and maximum settling velocities of the M_k

kaolinite classes and F_c is a flocculation factor.

Using Eqs. (C.2) and (C.3), one can attempt to best-fit the experimental data of Lau (1994) for different temperatures by changing the minimum settling velocity, ω_{s1} , and the flocculation factor, F_c . The results are shown in Figures (C.2)-(C.5), where $\ln(\tau_{dM}/\tau_{d1})/\ln(\omega_{sM}/\omega_{s1})=0.5$ was taken. The plot of cumulative weight finer against the settling velocity for different temperatures is shown in Figure (C.6). It is observed that the settling velocity increases with decreasing of temperature. In other words, the flocs become stronger and denser with decreasing of temperature.

To express the temperature effect mathematically, the (median) settling velocity at 50% of cumulative weight (finer) is taken. The results are shown in Figure (2.3), where the dimensionless median settling velocity is plotted against the temperature with ω_{s0} as the settling velocity at 15 °C. Finally, from Figure (2.3) the temperature function, F , i.e., Eq. (2.28), is obtained as

$$F = \frac{\omega_s}{\omega_{s0}} = 1.776 - 0.0518\theta, \quad \text{for } \theta = 0 - 30 \text{ } ^\circ\text{C} \quad (\text{C.4})$$

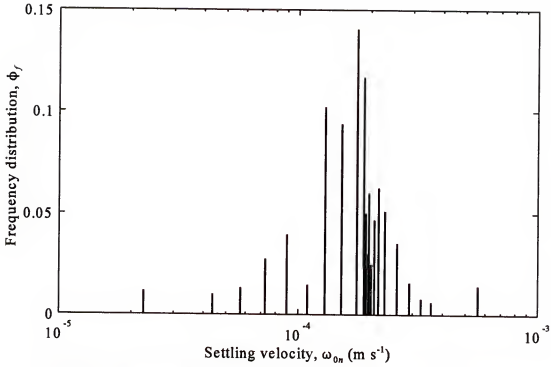


Figure C.1. Frequency distribution, ϕ_f , of the settling velocity of kaolinite.

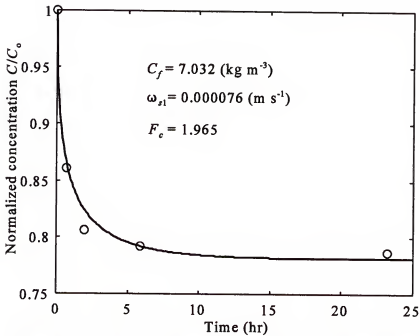


Figure C.2. Time-concentration relationship during deposition at 26°C . Open circles are the experimental data of Lau (1994).

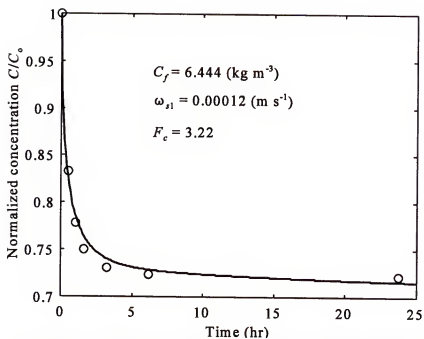


Figure C.3. Time-concentration relationship during deposition at 20 °C. Open circles are the experimental data of Lau (1994).

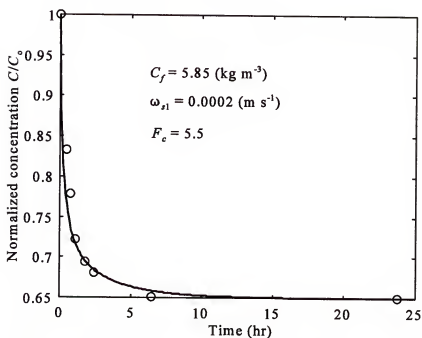


Figure C.4. Time-concentration relationship during deposition at 10 °C. Open circles are the experimental data of Lau (1994).

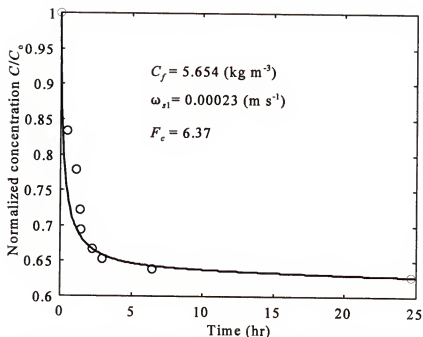


Figure C.5. Time-concentration relationship during deposition at 5 °C. Open circles are the experimental data of Lau (1994).

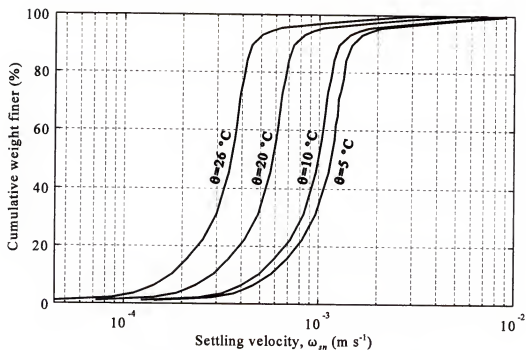


Figure C.6. Cumulative distribution of settling velocity of kaolinite at different temperatures, θ .

APPENDIX D
AN APPLICATION OF COHYD-UF: CONTRACTION SCOUR IN A RIVER

D.1 Scour Problem

An application of COHYD-UF is reported here for the simulation of a contraction scour problem at the Haldia Jetty, or Pier (Figure D.1), in the Hooghly River in India (Figure D.2). The pier, designed in the 1960s, served as an oil unloading terminal that enabled 40,000 DWT oil tankers to transfer oil to storage tanks at the Haldia Port. The Hooghly estuary transports high loads of fine-grained material. Since construction of the pier, a scour occurred in front of the pier. The presence of the hole near the tip of the pier was detrimental to the pier piles and hence the superstructure (Engineers India Limited, 1980; Rao, et al., 1980). The surficial shape of the scour hole was nearly elliptical, with the major axis and minor axis approximately perpendicular and parallel, respectively, to the longitudinal axis of the pier. The scour depth varied between 7 m and 13 m, and the hole migrated southward over a 40-month period up to May, 1980. The contours in Figure D.3 show the hole as it appeared in the May, 1980 survey. Note that the scour depths are taken as those below the original bottom elevation before the construction of the pier.

During the 40-month period the average rate of migration was 1.53 m/month along the direction of the main flow and 0.56 m/month perpendicular to the main flow and away from the pier. This mode and rate of migration suggested a slight dominance of the ebb

current over flood in the bottom region immediately adjacent to the pier. The strength of ebb current in this region was on the order of 2 m s^{-1} . The presence of such a strong current, coupled with the fact that a 40,000 DWT tanker was often docked at the pier, exacerbated the scour problem and necessitated action for filling up the hole in order to stabilize the pier (Engineers India Limited, 1980).

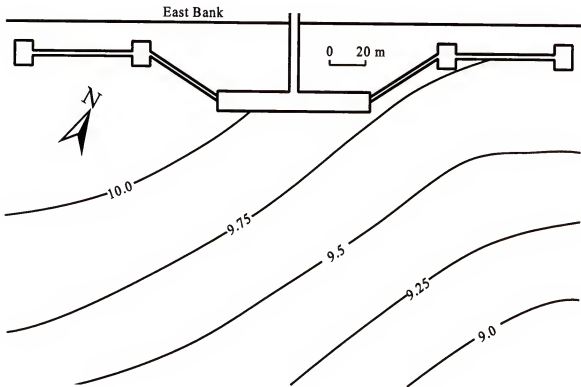


Figure D.1. Schematic diagram showing the Haldia oil pier and depth contours (m) in the vicinity. Water depth are below mean low water.

An evident conclusion that can be drawn is that the reduction of the flow area due to the pier resulted in an increase in the high ebb current and associated bed shear stress in front of the pier. Consequently, there was an increase in the erosive force in the effectively

contracted area in front of the pier, which is believed to be the main cause of the scour hole. Hence, it can be called contraction scour (HEC-18, 1995).

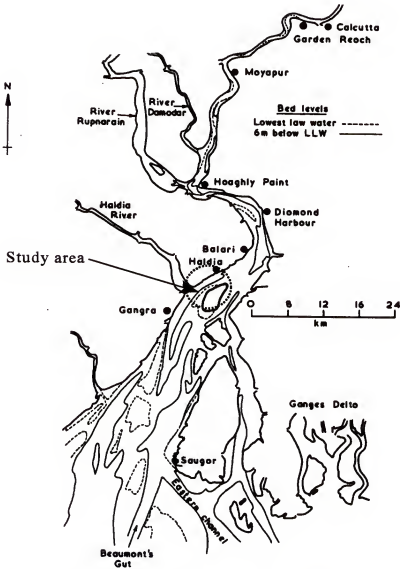


Figure D.2. Location map of Haldia oil pier, India.

D.2 Scour Simulation

As described above, the disturbance of the pier on the local flow and the dominance of ebb current were thought to be the main reasons for the development of the hole. Accordingly, the scour depth can be calculated through the modeled ebb flow, which will be assumed to be constant. Figure D.4 shows the bathymetry within the modeled segment of the river. The bed erosion rate is taken to be proportional to the bottom shear stress, τ_b , as follows

$$m_e = M_{max} \left(\frac{\tau_b}{\tau_s} - 1 \right) \quad (D.1)$$

By assuming the bottom to be in sedimentary equilibrium before the construction of the pier, one can take the critical shear stress for erosion, τ_s , to be the bottom shear stress before pier construction. The erosion rate constant, M_{max} , can be estimated using the maximum scour depth, ΔH_{max} , according to

$$M_{max} = \frac{\Delta H_{max}}{\rho_D \Delta T} \left(\frac{\tau_b'}{\tau_s'} - 1 \right)^{-1} \quad (D.2)$$

where τ_b' and τ_s' respectively are the bottom and critical shear stresses at the point where the maximum scour occurred, ΔT is the time period over which ΔH_{max} occurred, and ρ_D is the dry density of the bottom sediment. Accordingly, the scour depth at any position, ΔH , is obtained from

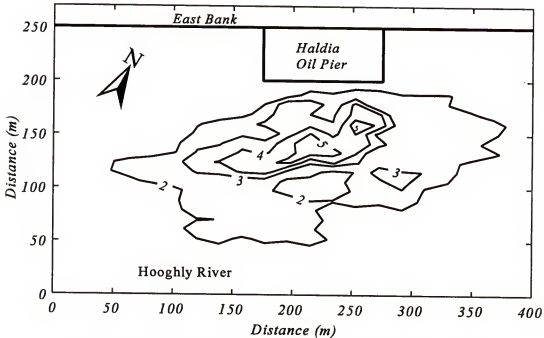


Figure D.3. Measured scour depths in front of the Haldia oil pier. The pier is shown as an idealized rectangular protrusion. Unit: m.

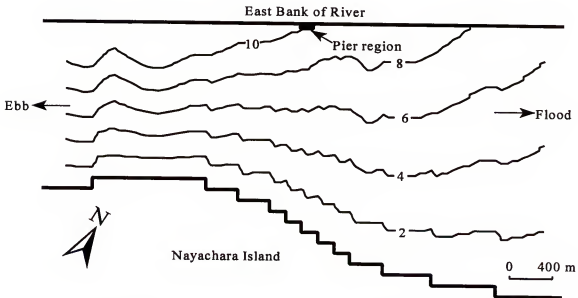


Figure D.4. Bottom topography of the modeled segment of the river in the vicinity of the Haldia pier. Water depths (unit: m) are below mean low water.

$$\Delta H = \frac{m_e \Delta T}{\rho_D} = \Delta H_{max} \left(\frac{\tau_b}{\tau_s} - 1 \right) \left(\frac{\tau_b'}{\tau_s'} - 1 \right)^{-1} \quad (D.3)$$

where the bottom shear stress, τ_b , was calculated from Eq. (2.9) without considering stratification effects. The values of $z_0=0.1$ mm [effective roughness of the bed in Eq. (2.9)] and $\Delta H_{max}=5$ m were taken in these calculations. From the modeling tests, it was found that the ratio of τ_b' to τ_s' was about 1.51.

The modeled region includes the area from 2.25 km upstream to 2.25 km downstream of the pier; thus with a length of 4.5 km (Figure D.4). The domain was discretised with spatial steps $\Delta x=50$ m, $\Delta y=25$ m and $\Delta \sigma=0.1$, with the total number of rectangular cells $M \times N \times L_f = 90 \times 104 \times 10 = 93,600$. A time step $\Delta t=5$ s was adopted due to stability constraints resulting from the numerical scheme involving in the back-tracing approach mentioned in Chapter 2 [Eq. (2.50)]. The lowest layer near the bottom was $0.05H$ above the bed, and the highest layer near the surface was $0.05H$ below the local water surface.

The upstream and downstream open boundary conditions were prescribed by constant water surface elevations at both ends. Elevations of 0.25 m above mean low water level at the upstream boundary and 0.00 m at downstream open boundary were taken. Model run was initiated at zero velocity and a constant water surface slope of 5.56×10^{-5} over the domain. COHYD-UF was run until a stable ebb flow field resulted. The model was run for two cases: before and after the construction of the pier, and both results were outputted for above

calculations. At each grid point, the bottom shear stress, τ_b in Eq. (D.3), was taken as the simulated value after the construction of the pier, and the bottom shear strength, τ_s in Eq. (D.3), was taken as the τ_b value before the construction of the pier.

D.3 Results

Figures D.5 and D.6 show simulated flow fields around the pier near the surface and the bottom, respectively. It is observed that the current in the front of the pier became stronger due to the disturbance of the pier on flow, with a maximum ratio between velocities after and before the construction of the pier of about 1.23.

The solid contours in Figure D.7 show the simulated scour depths in the front of the pier. In Figure D.8, the simulated areas, A_s , corresponding to 2-3 m, 3-4 m, 4-5 m and >5 m scour depths are plotted against the corresponding measured areas, A_m . This comparison shows that the model reasonably reproduced the area of the scour hole, and that the deeper the scour depth, the better the comparison of the simulated versus measured scour area.

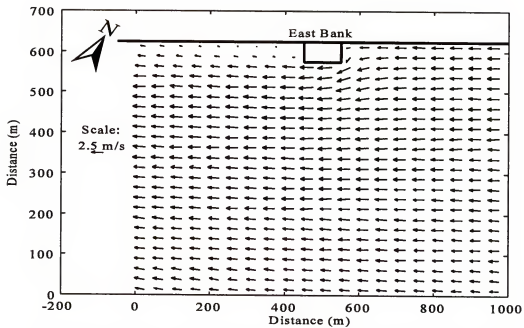


Figure D.5. Simulated flow field around pier at $0.05H$ below the surface.

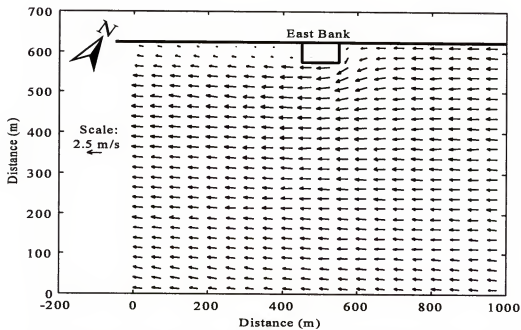


Figure D.6. Simulated flow field around pier at $0.05H$ above the bottom.

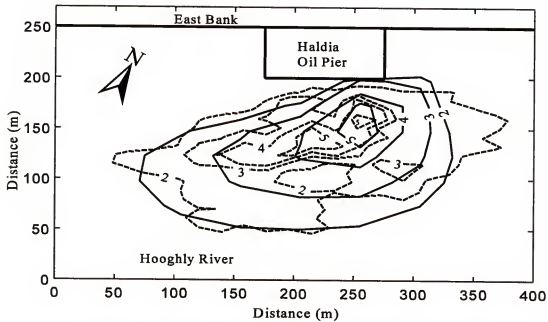


Figure D.7. Comparison of scour depths simulated (solid lines) and measured (dashed lines) in front of the Haldia oil pier. Unit: m.

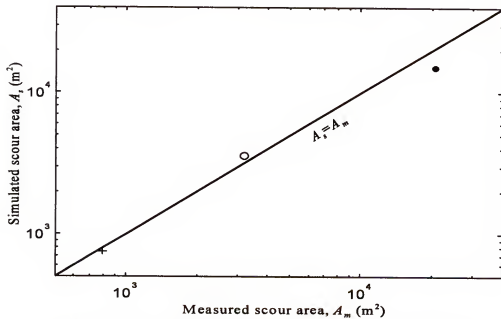


Figure D.8. Comparison between simulated and measured areas at 2-3 m (•), 3-4 m (*), 4-5 m (○) and >5 m (+) scour depths.

APPENDIX E SIMULATION OF SEDIMENT DEPOSITION IN A FLUME

E.1 Introduction

In order to test the ability of COSED-UF in predicting sedimentation, a simulation was conducted to compare modeled and observed shoaling patterns in the single flume test of Ariathurai (1974). In the simulation, the settling velocity in moving water was determined using experimental data of cohesive sediment deposition from Mehta (1973).

E.2. Flume Test

In the test of Ariathurai (1974), a 20 m long, 61 cm wide tilting recirculating flume was used. Approximately two-thirds of the way down the flume, a grating made of vertical steel rods, each of 6.35 mm diameter, was placed across one-half of the flume width so that it partially blocked the flow. The barrier allowed considerable flow through itself. Reconstituted seawater with a salinity of about 31‰ was added to the flume to give a flow depth of 10 cm. The flume pump was then set so as to generate an average velocity of about 17 cm s^{-1} . The slope of the flume bottom was adjusted simultaneously to produce a uniform flow depth along the length.

Before starting the experiment, the barrier was removed and the flow velocity increased. Sediment was then added to the flume gradually. San Francisco Bay sediment (bay mud) obtained from deposits in a yacht harbor in Mare Island was used for the test. Sea

shells, silt and other coarse materials present in the sample were removed by sedimentation and the remaining cohesive sediment with some silt in it was mixed in sea water and poured into running water in the flume slowly until an initial mean SSC of 0.2 kg m^{-3} was reached.

After all of the sediment had been added the barrier was placed and the velocity decreased to the same value as earlier (i.e., 17 cm s^{-1}). Afterwards, the suspended sediment settled gradually in the region in the lee of the barrier having relatively low velocities. The test was carried out for a period of about 3.5 days. Water was then drained out slowly and the deposition pattern around the barrier was recorded.

It was found that the SSC decreased with time according to (Ariathurai, 1974)

$$C = C_0 10^{-k_d t / 2.303} \quad (\text{E.1})$$

where C is the vertically-averaged SSC, C_0 is the initial SSC ($\approx 0.2 \text{ kg m}^{-3}$), and k_d is a deposition rate constant, which was found to be $1.0 \times 10^{-5} \text{ s}^{-1}$ by calibration (Krone, 1962; Ariathurai, 1974).

E.3 Settling Velocity in Moving Water

As stated in Section 4.3.5, the settling velocity in moving water is characteristically different from that in quiescent water, since increasing turbulence can enhance flocculation and at the same time limit the size of flocs that can be sustained. To determine the relevant settling velocity, experimental data on bay mud deposition reported in Mehta (1973) were used. These experiments were carried out in flumes under different bottom shear stress, τ_b ,

and initial SSC, C_0 . The data have been reported as the fraction of depositable concentration, $C^* [(C_0 - C)/(C_0 - C_f)]$, as a function of non-dimensional time, $t^* (=t/t_{50})$, where C_f is the final (steady state) SSC and t_{50} is the time corresponding to $C^* = 50\%$. Table E.1 gives the basic parameters in these experiments.

Table E.1. Basic parameters in deposition experiments using the bay mud

No.	C_0 (kg m^{-3})	H (m)	τ_b (Pa)	τ_d (Pa)	C_f (kg m^{-3})	t_{50} (hr)	Investigator
1	8.45	0.152	0.165	0.194	4.23	10	Mehta (1973)
2	0.50	0.305	0.067	0.070	0.05	63	Krone (1962)
3	0.92	0.305	0.049	0.065	0.00	23	Krone (1962)
4	1.92	0.305	0.037	0.065	0.00	7	Partheniades (1962)
5	21.00	0.152	0.031	0.065	0.00	5.9	Krone (1962)

Once $C^*(t^*)$, t_{50} , C_0 , C_f and water depth H are known, the settling velocity can be calculated from

$$\omega_s = \frac{2H(C^n - C^{n-1})}{C \Delta t p_d} \quad (\text{E.2})$$

where C^n and C^{n-1} are SSC at two consecutive measurements, Δt is the time interval between these two measurements, p_d is the probability of sediment deposition, which is

taken as $p_d=1-\tau_b/\tau_d$ (Krone, 1962), τ_d is the critical shear stress for deposition, and the instantaneous concentration $C=(C^n+C^{n+1})/2$. When applying Eq. (E.2), one should consider the non-uniformity of the sediment. In this case each class of the sediment has a different value of τ_d (Appendix C). By assuming that there is no interaction among different sediment classes, Mehta and Lott (1987) related the critical stress, τ_{dn} , to the settling velocity, ω_{sn} , for the n^{th} sediment class by

$$\tau_{dn} = \tau_{d1} \left(\frac{\omega_{sn}}{\omega_{s1}} \right)^{\beta_d} \quad (\text{E.3})$$

where $\beta_d [= \ln(\tau_{dM}/\tau_{d1}) / \ln(\omega_{sM}/\omega_{s1})]$ is a sediment-dependent constant, e.g., $\beta_d=0.5$ for kaolinite (Mehta and Lott, 1987). The other symbols are the same as in Appendix C. For the bay mud, $\tau_{d1}=0.065$ Pa, $\tau_{dM}=0.318$ Pa, and $\omega_{s1} = 2.3 \times 10^{-5}$ m s⁻¹ were chosen (Mehta, 1973). Considering that under a given flow only sediment classes having $\tau_{dn} \geq \tau_b$ are depositable, one can take τ_d in Eq. (E.2) as the minimum value of the critical stress of the depositable sediment classes, i.e., $\tau_d = \text{MIN}(\tau_{dn} | \tau_{dn} \geq \tau_b)$. Table E.1 gives τ_d for each test.

The calculated results using Eq. (E.2) are shown in Figure E.1, where the solid line is the best-fit of the calculated data points using the settling velocity - SSC relation given by Eq. (4.12). It is seen that for $\text{SSC} < \sim 0.2$ kg m⁻³ the particles become practically free settling, with a settling velocity ω_{sf} of about 4.0×10^{-5} m s⁻¹.

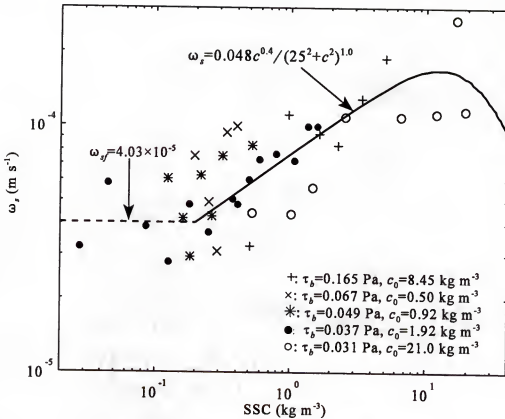


Figure E.1. Settling velocity as a function of SSC in moving water. Data are from Mehta (1973).

E.4 Deposition Simulation

In the simulation, the flume was discretized with spatial steps $\Delta x = 0.26$ m, $\Delta y = 0.02032$ m and $\Delta z = 0.1$, with the total number of rectangular cells $M \times N \times L_f = 77 \times 30 \times 10 = 23,100$. A time step $\Delta t = 0.02$ s was adopted due to the same reason as stated in Appendix D. The lowest layer near the bottom was $0.05H$ above the bed and the highest layer near the surface was $0.05H$ below the local water surface.

The upstream and downstream boundary conditions were prescribed by constant water surface elevations at both ends. Elevations of 2.5 cm below the horizontal datum at the downstream and 0.00 m at the upstream boundary were taken. This yielded a mean water surface slope of 1.25×10^{-3} . The flume bottom was tilted at the same slope as the water surface. The water depth was 10 cm. The following values of the hydrodynamic parameters were empirically selected: $A_x = 0.05 \text{ m}^2 \text{ s}^{-1}$, $A_y = 0.005 \text{ m}^2 \text{ s}^{-1}$ and $z_0 = 0.5 \text{ mm}$. Under these conditions, the model generated a cross-sectional mean velocity of 17 cm s^{-1} before the setting of the barrier.

In the model grid, the real barrier was approximated by alternatively placed solid lines at the same location as in the flume test. The model was initiated at zero velocity and a constant water surface slope of 1.25×10^{-3} . COHYD-UF was then run until a stable flow field resulted. The stable result was outputted for calculation of deposition. Figure E.2 shows the simulated flow field. It is observed that the velocity is relatively weak in the regions before and below the barrier, and also near the side walls, which are potential areas of deposition (Ariathurai, 1974).

As described earlier, during the deposition process the SSC in the flume was found to be a function of time, as defined by Eq. (E.1). Thus, the deposition depth at each grid point can be simply evaluated from

$$\Delta H = \sum \frac{C \omega_s \Delta t}{\rho_D} \left(1 - \frac{\tau_b}{\tau_d} \right) \quad (\text{E.4})$$

where ρ_D is the dry density of the newly deposited sediment (140 kg m^{-3}). The instantaneous concentration, C , was calculated by Eq. (E.1), and the bottom shear, τ_b , from Eq. (3.9).

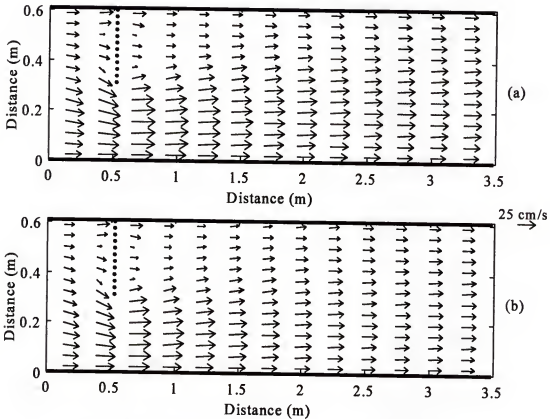


Figure E.2. Simulated flow field around the barrier in the flume, (a) near the surface and (b) near the bottom.

The calculated sediment deposition in the region downstream the barrier are shown in Figure E.3. Also shown in this figure are the measured thickness of the deposit. It is seen that the majority of deposition took place downstream the barrier due to a dramatic decreasing in the velocity there (Figure E.2).

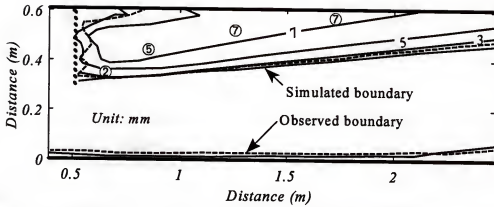


Figure E.3. Distribution of simulated (solid lines) and observed (numbers in circles) deposition (thickness) at the down side of the barrier. Data are from Ariathurai (1974).

BIBLIOGRAPHY

- Allen, G. P., Sauzay, G., Castaing, P. and Jouanneau, J. M. (1976). Transport and deposition of suspended sediment in the Gironde estuary, France. In: *Estuarine Processes*, Vol. II, M. Wiley ed., Academic Press, New York, 63-81.
- AmasSeds Research Group, (1990). A multidisciplinary Amazon shelf sediment study. *EOS. Transactions*, American Geophysical Union, 71(45), 1776-1777.
- Ariathurai, R. (1974). A finite element model for sediment transport in estuaries. *Ph. D. Thesis*, University of California, Davis, California, 192p.
- Ariathurai, R. and MacArthur, R. C. and Krone, R. B. (1977). Mathematical model of estuarial sediment transport. *Dredged Material Research Program, Technical Report D-77-12*. U. S. Army Engineering Waterways Station, Vicksburg, Mississippi, 77p.
- Bagnold, R. A. (1954). Experiments on a gravity-free dispersion of large solid spheres in a Newtonian fluid under shear. *Proceedings of the Royal Society of London*, A 225, 49-63.
- Bagnold, R. A. (1956). The flow of cohesionless grains in fluids. *Proceedings of the Royal Society of London, Philosophical Transactions*, B 249, 235-297.
- Bendat, J. S. and Piersol, A. G. (1971). *Random Data: Analysis and Measurement Procedures*, Wiley-Interscience, New York, 407p.
- Bertolazzi, E. (1990). Metodo PCG ed applicazione ad un modello di acque basse. *Thesis*, University of Trento, Trento, Italy, 135p.
- Bi, A. and Sun, Z. (1984). A preliminary study on the estuarine process in Jiaojiang River, China. *Journal of Sediment Research*, 3, 12-26 (in Chinese).
- Bosworth, R. C. L. (1956). The kinetics of collective sedimentation. *Journal of Colloidal Science*, 11, 496-500.

- Broward, F. K. and Wang, Y. H. (1972). An experiment on the growth of small disturbances at the interface between two streams of different densities and velocities. *Proceedings of the International Symposium on Stratified Flows*, Novosibirsk, USSR, 491-498.
- Buch, E. (1981). On entrainment and vertical mixing in stably stratified fjords. *Estuarine, Coastal and Shelf Science*, 12(4), 461-469.
- Burt, T. N. (1984). Field settling velocities of estuary muds. In *Lecture Notes on Coastal and Estuarine Studies 14: Estuarine Cohesive Sediment Dynamics*. A. J. Mehta ed., Springer-Verlag, Berlin, 126-150.
- Burt, T. N. and Parker, W. R. (1984). Settlement and density in beds of natural mud during successive sedimentation. *Report IT 262*, Hydraulics Research Limited, Wallingford, Oxfordshire, UK, 15p.
- Businger, J. A., Wyngaard, J. C., Izumi, Y. and Bradley, E. F. (1971). Flux-profile relationships in the atmospheric surface layer. *Journal of Atmospheric Science*, 28, 181-189.
- Carslaw, H. S. and Jaeger, J. C. (1959). *Condition of Heat in Solids*, Clarendon Press, Oxford, UK, 53p.
- Castaing, P. and Allen, G. P. (1981). Mechanisms controlling seawards escape of suspended sediment from the Gironde: a macrotidal estuary in France. *Marine Geology*, 40, 101-118.
- Casulli, V. and Cheng, R. T. (1992). Semi-implicit finite-difference method for three-dimensional shallow water flow. *International Journal for Numerical Methods in Fluids*, 15, 629-648.
- Chou, I. B. (1975). An experimental investigation of interfacial waves generated by low frequency internal waves. *M. S. Thesis*, University of Florida, Gainesville, Florida, 103p.
- Christodoulou, G. C. (1986). Interfacial mixing in stratified flows. *Journal of Hydraulic Research*, 24(2), 77-92.
- Chu, V. H. and Vanvari, M. R. (1976). Experimental study of turbulent stratified shearing flow. *Journal of the Hydraulics Division, ASCE*, 102(6), 691-706.
- Costa, R. G. (1989). Flow-fine sediment hysteresis in sediment-stratified coastal waters, *M. S. Thesis*, University of Florida, Gainesville, Florida, 155p.

- Costa, R. G. and Mehta, A. J. (1990). Flow-fine sediment hysteresis in sediment-stratified coastal waters. *Proceedings of the 20th Coastal Engineering Conference*, Vol. 2, ASCE, New York, 2047-2060.
- Delisi, D. and Corcos, G. M. (1973). A study of internal waves in a wind tunnel. *Boundary Layer Meteorology*, 5, 121-137.
- Dong, L. X., Wolanski, E. and Li, Y. (1997). Field and modeling studies of fine sediment dynamics in extremely turbid Jiaojiang River estuary, China. *Journal of Coastal Research*, 13(4), 995-1003.
- Dyer, K. R. (1986). *Coastal and Estuarine Sediment Dynamics*, Wiley, New York, 342p.
- Dyer, K. R. and Evans, E. M. (1989). Dynamics of turbidity maximum in a homogeneous tidal channel. *Journal of Coastal Research*, SI 5, 23-30.
- Einstein, H. A. and Chien N. (1955). Effects of heavy sediment concentration near the bed on velocity and sediment distribution. *Missouri River Division Series, No. 8*, University of California, Berkeley, California, 76p.
- Eisma, D., van der Gaast, S. J., Martin, J. M. and Thomas, A. J. (1978). Suspended matter and bottom deposition of the Orinoco delta: turbidity, mineralogy and elementary composition. *Netherlands Journal of Sea Research*, 12(2), 224-251.
- Ellison, T. H. and Turner, J. S. (1959). Turbulent entrainment in stratified flows. *Journal of Fluid Mechanics*, 6, 423-448.
- Engineers India Limited, (1980). Technical feasibility report - second oil unloading terminal for Haldia, Vol. II, Submitted to the Ministry of Shipping and Transport, Government of India, New Delhi, 53p.
- Fu, N. and Bi, A. (1989). Discussion on the problems in sediment transport of Jiaojiang river. *Journal of Sedimentary Research*, 3, 52-57 (in Chinese).
- Gibson, R. E., Englund, G. L. and Hussey, M. J. L. (1967). The theory of one-dimensional consolidation of saturated clays - I. *Géotechnique*, 17, 261-273.
- Goldberg, E. and Bruland, K. (1974). Radioactive chronologies. In: *The Sea*, Vol. 5, E. D. Goldberg ed., John Wiley & Sons, New York, 93-103.
- Greenspan, D. and Casulli, V. (1988). Numerical Analysis for Applied Mathematics. *Science and Engineering*, Addison-Wesley, Reading, MA, 139p.

- Grubert, J. P. (1990). Interfacial mixing in estuaries and fjords. *Journal of Hydraulic Engineering*, 116(2), 176-195.
- Guan, W. B., Wolanski, E. and Dong, L. X. (1998). Cohesive sediment transport in the Jiaojiang River estuary, China. *Estuarine, Coastal and Shelf Science*, 46(6), 861-871.
- Hansen, D. V. and Rattray, M. Jr. (1965). Gravitational circulation in straits and estuaries. *Journal of Marine Research*, 23(2), 104-122.
- Hayter, E. J. (1983). Prediction of cohesive sediment movement in estuarial waters, *Ph. D. Thesis*, University of Florida, Gainesville, Florida, 348p.
- Hopfinger, E. J. and Linden, P. F. (1982). Formation of thermoclines in zero-mean-shear turbulence subjected to a stabilizing buoyancy flux. *Journal of Fluid mechanics*, 114, 157-173.
- Hunt, J. N. (1954). The turbulent transport of suspended sediment in open channel. *Proceedings of the Royal Society of London*, A 224, 322-335.
- Hydraulic Engineering Circular No. 18 (HEC-18), (1995). Evaluating Scour at Bridges (Third Edition). U.S. Department of Transportation, Federal Highway Administration, Washington DC, 225p.
- Hwang, K. N. (1989). Erodibility of fine sediment in wave-dominated environments. *M. S. Thesis*, University of Florida, Gainesville, Florida, 158p.
- Inglis, C. C. and Allen, F. H. (1957). The regimen of the Thames estuary as affected currents, salinities and river flow. *Proceedings of the Institution of Civil Engineers*, 7, 827-868.
- Ippen, A. T. and Harleman, D. R. F. (1966). Tidal dynamics in estuaries. In: *Estuary and Coastline Hydrodynamics*, A. T. Ippen ed., McGraw-Hill, New York, 493-545.
- James, A. E., Williams, D. J. A. and Williams, P. R. (1988). Small strain, low shear rheometry of cohesive sediments. In: *Physical Processes in Estuaries*, J. Dronkers and W. van Leussen eds., Springer-Verlag, Berlin, 488-500.
- Jiang, J. H. and Wolanski, E. (1998). Vertical mixing by internal wave breaking at the lutocline, Jiaojiang River estuary, China. *Journal of Coastal Research*, 14(4), 1426-1431.
- Jobson, H. E. and Sayre, W. W. (1970). Vertical transfer in open channel flow. *Journal of the Hydraulics Division*, ASCE, 96(3), 7148-7152.

- Kantha, L., Phillips, O. and Azad, R. (1977). On turbulent entrainment at a stable density interface. *Journal of Fluid Mechanics*, 79, 753-768.
- Kato, H. and Phillips, O. M. (1969). On the penetration of a turbulent layer into stratified fluid. *Journal of Fluid Mechanics*, 37, 643-655.
- Kent, R. E. and Pritchard, D. W. (1959). A test of mixing length theories in a coastal plain estuary. *Journal of Marine Research*, 1, 62-72.
- Kineke, G. C. (1993). Fluid muds on the amazon continental shelf. *Ph. D. Thesis*, University of Washington, Seattle, Washington, 259p.
- Kirby, R. (1986). Suspended fine cohesive sediment in Severn estuary and Inner Bristol channel, U.K. *Report ETSU-STP-4042*, United Kingdom Atomic Energy Authority, Harwell, UK, 243p.
- Kirby, R. and Parker, W. R. (1977). The physical characteristics and environmental significance of fine-sediment suspension in estuaries. In: *Estuaries, Geophysics and the Environment*, National Academy of Science, Washington DC, 110-120.
- Kirby, R. and Parker, W. R. (1982). A suspended sediment in the Severn estuary. *Nature*, 295:5848, 396-399.
- Kit, E., Berent, E. and Vajda, A. (1980). Vertical mixing induced by wind and a rotating screen in a stratified fluid in a channel. *Journal of Hydraulic Research*, 18(1), 35-58.
- Kranenburg, C. and Winterwerp, J. C. (1997). Erosion of fluid mud layers. I: entrainment model. *Journal of Hydraulic Engineering*, 123(6), 504-511.
- Krone, R. B. (1962). Flume studies of the transport of sediment in estuarial shoaling processes. *Final Report*, Hydraulic Engineering Laboratory and Sanitary Engineering Research Laboratory, University of California, Berkeley, California, 110p.
- Kynch, G. J. (1952). A theory of sedimentation. *Transaction of the Faraday Society*, 48, 166-176.
- Lamb, H. (1932). *Hydrodynamics*. Sixth edition, Dover Publications, New York, 738p.
- Lau, Y. L. (1994). Temperature effect on settling velocity and deposition of cohesive sediments. *Journal of Hydraulic Research*, 32(1), 41-51.
- Lauder, B. E. and Spalding, D. B. (1972). *Lecture in Mathematical Models of Turbulence*, London, New York, Academic Press, 169p.

- Lee, S. C. and Mehta, A. J. (1994). Cohesive Sediment Erosion. *Dredging Research Program, Contract Report DRP-94-6*, U. S. Army Engineering Waterways Station, Vicksburg, Mississippi, 41p.
- Lesieur, M. (1997). *Turbulence in Fluids*. Third Revised and Enlarged Edition, Kluwer Academic Publishers, Dordrecht, The Netherlands, 515p.
- Li, B. G., Xie, Q. C., Xia, X. M., Li, Y. and Eisma, D. (1999). Size distribution of suspended sediment in maximum turbidity zone and its response to tidal dynamics in Jiaojiang River estuary, China. *Journal of Sediment Research*, 1, 18-26 (in Chinese).
- Li, Y., Pan, S., Shi, X. and Li, B. (1992). Recent sedimentation rates for the zone of the turbidity maximum in the Jiaojiang estuary. *Journal of Nanjing University*, Natural Science Edition, 28(4), 623-632 (in Chinese).
- Li, Y., Wolanski, E. and Xie, Q. C. (1993). Coagulation and settling of suspended sediment in the Jiaojiang River estuary, China. *Journal of Coastal Research*, 9(2), 390-402.
- Liu, Y. M. (1988). A two-dimensional finite-difference model for moving boundary hydrodynamic problems, *M.S. Thesis*, University of Florida, Gainesville, Florida, 134p.
- Lofquist, L. (1960). Flow and stress near an interface between stratified liquids. *The Physics of Fluids*, 3(2), 158-175.
- Maa, P. Y. and Mehta, A. J. (1987). Mud erosion by waves: a laboratory study, *Continental Shelf Research*, 7(11/12), 1269-1284.
- McCave, I. N. (1979). Suspended sediment. In: *Estuarine Hydrography and Sedimentation, A Handbook*, K. R. Dyer ed., Cambridge University Press, Cambridge, UK, 131-183.
- McLaughlin, R. T. (1959). The settling properties of suspension. *Journal of the Hydraulics Division, ASCE*, 85(12), 9-14.
- Mehta, A. J. (1973). Depositional behavior of cohesive sediments. *Ph. D. Thesis*, University of Florida, Gainesville, Florida, 275p.
- Mehta A. J. (1989). Fine sediment stratification in coastal water. *Proceedings of Third National Conference on Dock & Harbour Engineering, K.R.E.C., Surathkal, India*, 487-492.
- Mehta, A. J. (1991a). Understanding fluid mud in a dynamic environment. *Geo-Marine Letters*, 11, 113-118.

- Mehta, A. J. (1991b). Characterization of Cohesive Soil Bed Surface Erosion, With Special Reference to the Relationship between Erosion Shear strength and Bed Density. *Report No. UFL/COE-MP-91/4*, University of Florida, Gainesville, Florida, 83p.
- Mehta, A. J. and Li, Y. G. (1997). A PC-based short course on fine-grained sediment transport engineering. Coastal and Oceanographic Engineering Department, University of Florida, Gainesville, Florida, 91p.
- Mehta, A. J. and Lott, J. W. (1987). Sorting of fine sediment during deposition. *Proceedings of Coastal Sediment '87*, ASCE, New York, 348-362.
- Mehta A. J. and Parchure, T. M. (1999). Surface erosion of fine-grained sediment revisited. In: *Muddy Coasts: Processes and Products*, B. W. Flemming, M. T. Delafontaine and G. Liebezeit eds., Elsevier, Amsterdam (in press).
- Mehta, A. J., Parchure, T. M., Dixit, J. G. and Ariathurai, R. (1982). Resuspension potential of deposited cohesive sediment beds. In: *Estuarine Comparisons*. V. S. Kennedy ed., Academic Press, New York, 591-609.
- Mehta, A. J. and Srinivas, R. (1993). Observations on the entrainment of fluid mud in shear flow. In: *Nearshore Estuarine Cohesive Sediment Transport*, A. J. Mehta ed., American Geophysical Union, Washington, DC, 224-246.
- Monin, A. S. and Obukhov, A. M. (1953). Dimensionless characteristics of turbulence in atmospheric surface layer. *Doklady Akad Nauk SSSR*, 98, 223-226 (in Russian).
- Moore, M. J. and Long, R. R. (1971). An experimental investigation of turbulent stratified shearing flow. *Journal of Fluid Mechanics*, 49, 635-655.
- Munk, W. H. and Anderson, E. A. (1948). Notes on a theory of the thermocline. *Journal of Marine Research*, 7, 276-295.
- Narimousa, S. and Fernando, H. J. S. (1987). On the sheared interface of an entraining stratified fluid. *Journal of Fluid Mechanics*, 174, 1-22.
- Narimousa, S., Long, R. R. and Kitaigorodskii, S. A. (1986). Entrainment due to turbulent shear flow at interface of a stably stratified fluid. *Tellus*, 38A(1), 76-87.
- Neumann, G. and Pierson, W. J. (1966). *Principles of Physical Oceanography*. Prentice-Hall, Englewood Cliffs, New Jersey, 545p.
- Nichols, M. M. (1984-1985). Fluid mud accumulation processes in an estuary. *Geo-Marine Letters*, 4, 171-176.

- Nicholson, J. and O'Connor, B. A. (1986). Cohesive sediment transport model. *Journal of Hydraulic Engineering*, 112, 621--640.
- Ochi, M. K. (1990). *Applied Probability & Stochastic Processes*, John Wiley & Sons, New York, 499p.
- Odd, N. V. M. and Cooper, A. J. (1989). A two-dimensional model of the movement of fluid mud in a high energy turbid estuary. *Journal of Coastal Research*, SI(5), 85-193.
- Odd, N. V. M. and Owen, M. W. (1972). A two-layer model of mud transport in the Thames estuary. *Proceedings of the Institution of Civil Engineers, Supplement IX, Paper 7517S*, 175-205.
- Odd, N. V. M. and Rodger J. G. (1978). Vertical mixing in stratified tidal flows. *Journal of the Hydraulics Division, ASCE*, 104(3), 337-351.
- Odd, N. V. M. and Rodger, J. G. (1986). An analysis of the behaviour of fluid mud in estuaries. *Report No. SR 84*, Hydraulics Research Limited, Wallingford, Oxfordshire, 25p.
- Ogata, A. and Banks, R. B. (1961). A solution of the differential equation of longitudinal dispersion in porous media. *Professional Paper 411-A*, U. S. Geological Survey, A1-A9.
- Owen, M. A. (1970). Properties of a consolidating mud. *Report No. INT 83*, Hydraulics Research Station, Wallingford, UK, 35p.
- Owen, M. A. and Odd, N. V. M. (1970). A mathematical model of the effect of a tidal barrier on siltation in an estuary. *Proceedings of an International Conference on the Utilization of Tidal Power*, Halifax, Nova Scotia, Canada, 457-484.
- Parchure, T. M. and Mehta, A. J. (1985). Erosion of soft cohesive sediment deposits. *Journal of Hydraulic Engineering*, 111(10), 1308-1326.
- Parker, W. R. and Kirby, R. (1979). Fine sediment studies relevant to dredging practice and control. *Proceedings of the Second International Symposium on Dredging Technology*, BHRA, Paper B2, Texas A & M University, College Station, Texas, 13-26.
- Parker, W. R. and Lee, K. (1979). The behaviour of fine sediment relevant to the dispersal of pollutants. *ICES Workshop on Sediment and Pollutant Interchange in Shallow Sea*, Tecel, UK, 28-34.

- Partheniades, E. (1962). A study of erosion and deposition of cohesive soil in salt water. *Ph. D. Thesis*, University of California, Berkeley, 192p.
- Pedersen, F. B. (1980). A monograph on turbulent entrainment and friction in two-layer stratified flow. *Series Paper No. 25*, Technical University of Denmark, Lyngby, Denmark, 397p.
- Phillips, O. M. (1977). *The Dynamics of the Upper Ocean*. 2nd ed., Cambridge University Press, London, 336p.
- Postma, H. (1967). Sediment transport and sedimentation in the estuarine environment. In: *Estuaries*, American Association for the Advancement of Science, Publication No. 83, Washington DC, 158-179.
- Prandtl, Z. A. (1925). Bericht über untersuchungen zur ausgebildeten turbulenz. *Zs Angew Math, Mech.*, 5, 136-169.
- Proudman, J. (1925). Tides in a channel. *Philosophical Magazine and Journal of Science*, 16, 465-475.
- Rao, P. V., Einerson, J. J., Einerson, J. A. and Mehta, A. J. (1980). A survey of small-craft recreational marinas in florida, *Technical Report, No. 151*, Department of Statistics, University of Florida, Gainesville, Florida, 41p.
- Rodi, W. (1980). Mathematical modeling of turbulence in estuaries. *Proceedings of the International Symposium on Mathematical Modeling of Estuarine Physics*, J. Sundermann and K. P. Holz ed., German Hydrographic Institute, Hamburg, 14-26.
- Ross, M. A. (1988). Vertical Structure of Estuarine Fine Sediment Suspensions. *Ph. D. Thesis*, University of Florida, Gainesville, Florida, 187p.
- Ross, M. A. and Mehta, A. J. (1989). On the mechanics of lutoclines and fluid mud. *Journal of Coastal Research*, SI 5, 51-61.
- Rosby, C. G. and Montgomery, R. B. (1935). The layer of functional influence in wind and ocean currents, *Papers of Physical Oceanography*, 3(3), 1-101.
- Scarlatos, P. D. and Mehta, A. J. (1993). Instability and entrainment mechanisms at the stratified fluid mud-water interface. In: *Nearshore and Estuarine Cohesive Sediment Transport*, A. J. Mehta ed., American Geophysical Union, Washington, DC, 205-223.
- Shi, Z. (1998). Acoustic observations of fluid mud and interfacial waves, Hangzhou Bay, China. *Journal of Coastal Research*, 14(4), 1348-1353.

- Shi, Z., Ren, L. F., Zhang, S. Y. and Chen, J. Y. (1997). Acoustic imaging of cohesive sediment resuspension and re-entrainment in the Changjiang Estuary, East China Sea. *Geo-Marine Letters*, 17, 162-168.
- Smith, T. J. and Kirby, R. (1989). Generation, stabilization and dissipation of layered fine sediment suspensions. *Journal of Coastal Research*, SI 5, 63-73.
- Sottolichio, A., Hir, P. L. and Castaing, P. (1999). Modeling mechanisms for the turbidity maximum stability in the Gironde estuary. In: *Coastal and Estuarine Fine Sediment Processes*, W. H. McAnally and A. J. Mehta, ed., Elsevier, Amsterdam (in Press).
- Srinivas, R. (1989). Response of fine sediment-water interface to shear flow. *M.S. Thesis*, University of Florida, Gainesville, Florida, 137p.
- Stansby, P. K. and Lloyd, P. M. (1995). A semi-implicit lagrangian scheme for 3D shallow water flow with a two-layer turbulence model. *International Journal of Numerical methods*, 20, 115--133.
- Su, J. L., Wang, K. S. and Li, Y. (1992). Fronts and transport of suspended matter in the Hangzhou Bay. *Acta Oceanologica Sinica*, 12(1), 1-15.
- Su, J. L. and Xu, W. Y. (1984). Modeling of the depositional patterns in Hangzhou Bay, *Coastal Engineering*, 8, 2181-2191.
- Toorman, E. A., and Berlamont, J. E. (1993). Mathematical modeling of cohesive sediment settling and consolidation. In: *Nearshore Estuarine Cohesive Sediment Transport*, A. J. Mehta ed., American Geophysical Union, Washington, DC, 148-184.
- Tsuruya, H., Murakami, K. and Irie, I. (1990a). Mathematical modeling of mud transport in ports with a multi-layered model: application to Kumamoto Port. *Report of the Port and Harbour Research Institute*, 29(1), 51p.
- Tsuruya, H., Murakami, K. and Irie, I. (1990b). Numerical simulations of mud transport by a multi-layered nested grid model. *Proceedings of the 22th Coastal Engineering Conference*, Vol. 3, ASCE, New York, 2098-3012.
- van den Bosch, L., Toorman, E. and Berlamont, J. (1988; 1989; 1990). Settling column experiments and *in situ* measurements, *Reports to IMDC*, Hydraulics Laboratory, Katholieke University Leuven, Belgium, variously paginated (in Dutch).
- van Leussen, W. and van Velzen, E. (1989). High concentration suspensions: their origin and importance in Dutch Estuaries and coastal waters. *Journal of Coastal Research*, SI(5), 1-22.

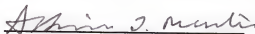
- Verreet, G. and Berlamont, J. (1989). Rheology and non-Newtonian behaviour of sea and estuarine mud. *Encyclopedia of Fluid Mechanics, Vol. VII: Rheology & Non-Newtonian Flow*, N. P. Cheremisinoff, Ed., Gulf Publishing Co., Houston, Texas, 135-149.
- Vinzon, S. B. (1998). A preliminary examination of amazon shelf sediment dynamics. *Engineer Degree Thesis*, University of Florida, Gainesville, Florida, 154p.
- Wiersma, J. (1984). Acoustisch onderzoek bodemslib in relatie tot sedimentatie in toegangseulen en zeehavens. *Report NZ-N-84.07*, Rijkswaterstaat, North Sea Directorate, 74p.
- Winterwerp, J. C. and Kranenburg, C. (1997). Erosion of fluid mud layers. II: experiment and model validation. *Journal of Hydraulic Engineering*, 123(6), 512-519.
- Wolanski, E., Asaeda, T. and Imberger, J. (1989). Mixing across a lutocline, *Limnology and Oceanography*, 34(5), 931-938.
- Wolanski, E., Chappell, J., Ridd, P. and Vertessy, R. (1988). Fluidization of mud in estuaries. *Journal of Geophysical Research*, 93(C3), 2351-2361.
- Wolanski, E., Gibbs, R. J., Mazda, Y., Mehta, A. and King, B. (1992). The role of turbulence in the settling of mud flocs. *Journal of Coastal Research*, 8, 35-46.
- Woodruff, D. P. (1973). *The Solid-Liquid Interface*. Cambridge University Press, Cambridge, UK, 182p.
- Wright, L. D., Wiseman, W. J., Bornhold, B. D., Prior, D. B., Suhayda, J. N., Keller, G. H., Yang, Z. S. and Fan, Y. B. (1988). Marine dispersal and deposition of Yellow River silts by gravity-driven underflows. *Nature*, 332 (14), No. 6164, 629-632.
- Wu, J. (1973). Wind-induced turbulent entrainment across a stable density interface. *Journal of Fluid Mechanics*, 61, 275-287.
- Yeh, H. Y. (1979). Resuspension of properties of flow deposited cohesive sediment beds. *M.S. Thesis*, University of Florida, Gainesville, Florida, 118p.
- Yu, G., Martin, J. M., Zhou, J., Windom, H. and Dawson, R. (1990). Biogeochemical study of the Changjiang estuary, China. Ocean Press, London, 898p.
- Zhou, Y. K. (1986). Some characteristics of stream-like macro-tidal estuary (Jiaojiang). *Geographical Study*, 5(1) (in Chinese).

Zimmerman, J. T. F. (1981). Dynamics, diffusion and Geomorphological significance of tidal residual eddies, *Nature*, 290(16), No. 5807, 549--555.

BIOGRAPHICAL SKETCH

Jianhua Jiang was born on March 15, 1961 in the village of Hezhai, Zhejiang, China. He received his Bachelor of Engineering degree in hydromechanics from the Hohai University, Nanjing, in 1983, and then worked as an Assistant Engineer in the East China Institute of Hydro-Electric Investigation and Design, Hangzhou, for three years. He obtained his Master of Science degree in physical oceanography in 1989 from the Second Institute of Oceanography, Hangzhou. Subsequently, he was hired as a coastal engineer by the same institute and was engaged in investigations of estuarine and coastal hydrodynamics and sediment transport for about six years. In 1996, he was accepted by the Coastal and Oceanographic Engineering Department of the University of Florida as a doctoral student and research assistant. After three years of study, he eventually earned the Doctor of Philosophy degree, and looks forward to contributing his newly acquired knowledge towards solving various coastal and estuarine engineering problems.

I certify that I have read this study and that in my opinion it conforms to acceptable standards of scholarly presentation and is fully adequate, in scope and quality, as a dissertation for the degree of Doctor of Philosophy.



Ashish J. Mehta, Chairman
Professor of Coastal and Oceanographic
Engineering

I certify that I have read this study and that in my opinion it conforms to acceptable standards of scholarly presentation and is fully adequate, in scope and quality, as a dissertation for the degree of Doctor of Philosophy.



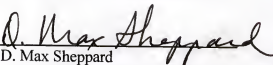
Robert G. Dean
Graduate Research Professor of Coastal
and Oceanographic Engineering

I certify that I have read this study and that in my opinion it conforms to acceptable standards of scholarly presentation and is fully adequate, in scope and quality, as a dissertation for the degree of Doctor of Philosophy.



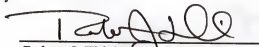
Kirk Hatfield
Associate Professor of Civil Engineering

I certify that I have read this study and that in my opinion it conforms to acceptable standards of scholarly presentation and is fully adequate, in scope and quality, as a dissertation for the degree of Doctor of Philosophy.



D. Max Sheppard
Professor of Coastal and Oceanographic
Engineering

I certify that I have read this study and that in my opinion it conforms to acceptable standards of scholarly presentation and is fully adequate, in scope and quality, as a dissertation for the degree of Doctor of Philosophy.



Robert J. Thieke
Assistant Professor of Coastal and
Oceanographic Engineering

This dissertation was submitted to the Graduate Faculty of the College of Engineering and the Graduate School and was accepted as partial fulfillment of the requirements for the degree of Doctor of Philosophy.

August, 1999



M. Jack Ohanian
Dean, College of Engineering

Winfred M. Phillips
Dean, Graduate School